UNIVERSITÀ DEGLI STUDI DI MILANO

Corso di Dottorato in Epidemiologia, ambiente e sanità pubblica

Development of an integrated *in silico* strategy for the risk assessment of chemicals and their mixtures on different toxicological outcomes.

TUTOR: Prof. Angelo Moretto
CO-TUTOR: Prof. Ivano Eberini

Luca Palazzolo
Matricola n° R11527

A mio padre.

A Giovanni Badino
che per mi insegnò le gioie della Ricerca.

Abstract

Ogni giorno siamo esposti a una miscela di più sostanze chimiche attraverso l'assunzione di cibo, l'inalazione e il contatto cutaneo. Il rischio per la salute che può derivare da ciò, dipende da come si combinano gli effetti delle diverse sostanze chimiche nella miscela e dalla presenza di sinergismo o antagonismo tra loro. Il numero di diverse combinazioni di sostanze chimiche nelle miscele è infinito e manca un'efficace strategia di prova per queste. Inoltre, vi è una pressione sociale per ridurre la sperimentazione sugli animali, che è la pratica corrente nei test di sicurezza delle sostanze chimiche. In questo contesto, la biochimica computazionale e, più in generale, la bioinformatica soddisfano tutti i requisiti e forniscono le basi per ulteriori studi *in vitro* o *in vivo*.
Scopo di questa tesi di dottorato è lo sviluppo di un flusso di lavoro *in silico* in grado di stabilire le priorità e discriminare le sostanze chimiche che agiscono come sostanze attive a livello endocrino (EAS), che interferiscono con il percorso dell'acido retinoico durante lo sviluppo dell'embrione e/o possono causare tossicità epatica. L'approccio basato sul ligando e quello basato sulla struttura sono stati integrati con la biologia del sistema al fine di descrivere il percorso degli esiti avversi partendo dall'osservazione dell'evento molecolare iniziale. In questo quadro, i risultati di (Q)SAR e di *docking* molecolare sono stati uniti in un punteggio di consenso maggioritario per classificare le sostanze chimiche e sono state utilizzate le simulazioni di dinamica molecolare a bassa frequenza per studiare la loro attività intrinseca, rispetto a uno specifico recettore nucleare. Inoltre, un approccio computazionale basato sia sulla teoria dello stato di transizione sia sulla teoria della densità funzionale è stato usato per discriminare un sottoinsieme di sostanze chimiche tra inibitori e substrati di particolari enzimi coinvolti nella via dell'acido retinoico, calcolando inoltre le loro energie libere di legame. Questa informazione è stata anche presa in considerazione sia nei modelli farmacocinetici (PD) che nei modelli farmacocinetici a base fisiologica (PBPK).
Questo flusso di lavoro condotto *in silico*, oltre ad essere più veloce, presenta vantaggi economici ed etici, riducendo sia i costi di ricerca che il numero di animali coinvolti, in accordo con le 3R della ricerca.

Abstract

Daily, we are exposed to a mixture of multiple chemicals via food intake, inhalation and dermal contact. The risk for health that may result from this depends on how the effects of different chemicals in the mixture combine, and whether there is any synergism or antagonism between them. The number of different combinations of chemicals in mixtures is infinite and an efficient test strategy for mixtures is lacking. Furthermore, there is social pressure to reduce animal testing, which is the current practice in safety testing of chemicals. In this context, computational biochemistry and, more in general, bioinformatics meets all the requirements, and provides the foundation for further in vitro or in vivo studies.

Aim of this PhD thesis is the development of an *in silico* workflow able to prioritize and discriminate chemicals that act as endocrine active substances (EAS), interfere with the retinoic acid pathway during embryo development and/or may cause liver toxicity. From the observation of the molecular initiating event to the description of the adverse outcome pathway, both ligand- and structure-based approaches were integrated with systems biology. Within this framework, (Q)SAR and molecular docking results were mixed into a majority consensus score to rank chemicals and low-mode molecular dynamic simulations were used to study their intrinsic activity, with respect to a specific nuclear receptor. Moreover, a computational approach based on both the transition state and the density functional theories was used to try discriminating a subset of chemicals as inhibitors or substrates of particular enzymes involved in the retinoic acid pathway, computing also their binding free energy values. This information was also included both in the pharmaco-dynamics (PD) and in the physiological based pharmaco-kinetics (PBPK) models.

This in silico pipeline, besides being faster, has economic and ethical advantages, reducing both the research costs and the number of involved animals, in agreement with the “3R” principles (Reduction, Refinement and Replacement).

Table of contents

Preface

Daily, we are exposed to a mixture of multiple chemicals *via* food intake, inhalation and dermal contact. The risk to health that may result from this depends on how the effects of different chemicals in the mixture combine, and whether there is any synergism or antagonism between them. The number of different combinations of chemicals in mixtures is infinite and an efficient test strategy for mixtures is lacking. Furthermore, there is a societal need to reduce animal testing, which is the current practice in safety testing of chemicals.
In this context, computational biochemistry and, more in general, bioinformatics meets all these needs, being the bases for further *in vitro* or *in vivo* studies. This approach has been largely applied in a multitude of research project, such as *EuroMix* and an Italian Multiple Sclerosis Foundation (FISM)-granted project, which I participated to, during my PhD. In particular, EuroMix, an H2020 project, delivered a mixture test strategy using novel techniques useful to refine the assessment of the future risk of the relevant mixtures for all the stakeholders such as the European Food Safety Authority (EFSA) or other EU regulatory authorities.
On the other hand, the FISM financed a project entitled "*Deciphering and modelling remyelinating mechanisms induced by clinically-used azole antifungals with exploitable repurposing properties"* that was purposely aimed at studying azole antifungals, already approved for clinical uses, to better understand the demyelinating component of MS and to counteract its pathological evolution. At the same time, the use of different cellular models of maturation, (re)myelination and tissue organization allowed us to quantitate the contribution of natural hormones and specific proteins to multiple sclerosis evolution and the molecular strategies exploitable for its treatment.
Again, in the field of risk assessment, bioinformatics approaches were applied to big data management and analysis, as for an EFSA procurement in which I worked as work-package leader, studying proteins with associated toxic effects. In this project, we integrated, through an *in silico* pipeline some bioinformatics tools to allow the risk assessment of the use of potentially toxic proteins in biotechnological products for food use.
Among the twelve papers published during my PhD as first or co-author, two of them are explicitly linked to my PhD project, explaining and applying the *in silico* pipeline discussed in the present PhD thesis.

The computational approach developed in this PhD thesis is aimed to prioritize and discriminate chemicals that act as endocrine active substances, interfere with the retinoic acid pathway both during embryo development and (re)myelinating processes and/or may cause liver toxicity, applying this pipeline directly in both the EuroMix and FISM projects. Both the computational approach and the results developed in my PhD are also reported in five different scientific report already submitted to the EU and FISM.

This *in silico* pipeline, in addition to being faster, has economic and ethical advantages, reducing both the research costs and the number of involved animals, in agreement to the 3R (Reduction, Refinement and Replacement).

Chapter 1 – Endocrine active substances

Endocrine active substances are defined as *exogenous substances or mixtures that alters function(s) of the endocrine system and consequently causes adverse health effects in an intact organism, or its progeny, or (sub)populations*.
The hormone action is related to the hormone capability to activate its nuclear receptor, that depends upon several factors, such as how much hormone is synthesized and released by the endocrine gland, how it is transported through the circulation, how much reaches the target organ, and how strongly the hormone binds its nuclear receptor and for how long it can activate its receptor.
The physico-chemical properties and 3D shape of each hormone are well-defined and unique, and each hormone has a corresponding receptor (or a set of receptors) that has (have) a complementary binding site to its hormone in a mechanism similar to lock-and-key system. The response of a given tissue or organ to a hormone is determined by the presence of receptors on target cells and receptor activation by hormone binding. Hormone shows an agonistic activity for its receptor, which implies an activation mediated by a closure of specific α-helix (α-helix 12), that is the starting point for biochemical pathways. These properties are fundamental to normal hormonal signalling, EASs can interfere with any of these steps.
In fact, EASs often interfere with endocrine systems by blocking the binding or mimicking the activity of the natural hormone on its receptor. In the first case, affinity and concentration values of EASs are in equilibrium and EASs act as *competitive ligands of hormone receptor* (or antagonist) because it does not allow the hormone::receptor complex formation and it does not activate the nuclear receptor and its related biochemical pathway. In the second case, an EAS can bind the receptor, inappropriately activating it and triggering processes normally activated only by the natural hormone.
The best-known example is the endocrine perturbation of hormones with estrogenic activity. In both males and females, ERs are present in many cells in the brain, in bone, in vascular tissues, and in reproductive tissues. While the estrogen role is better characterized in female reproduction, they also exert important activities for male reproduction, and are also involved in neurobiological functions, bone development and maintenance, cardiovascular functions, and many other functions. Natural estrogens exert these actions, after being released from the gonad (ovary-female or testis-male), by binding to ERs in the target tissues. Estrogen receptors are not the only receptors that are affected in this manner by EASs, although they are the best studied. EAS interfere with androgen (AR) and progesterone (PR) receptors, involving gender- and hormone-dependent clinical outcomes.
In addition, a single EAS may have the ability to affect multiple hormonal signalling pathways. Thus, it is quite likely that one type of EAS can disrupt two, three, or more endocrine functions, with widespread consequences on the biological processes that are controlled by those vulnerable endocrine glands. Some of the phenotypic endpoints that can be affected include abnormal anogenital distance, cryptorchidism, nipple retention and/or osteoporosis.
Chapter I will discuss the pipeline of the procedures for prioritization and validation of chemicals as putative ligands and their application to the EuroMix chemical inventory, extending the study field from ERα to all the four sexual hormone receptors (ERα, ERβ, AR, PR). In particular, this chapter will be divided in two part in which we developed the complete *in silico* pipeline to study EAS on Erα using a specific training set and carried out an *in silico* prioritization of the EuroMix chemical inventory of thousand chemicals *via* molecular docking approach, as reported in Figure 1.

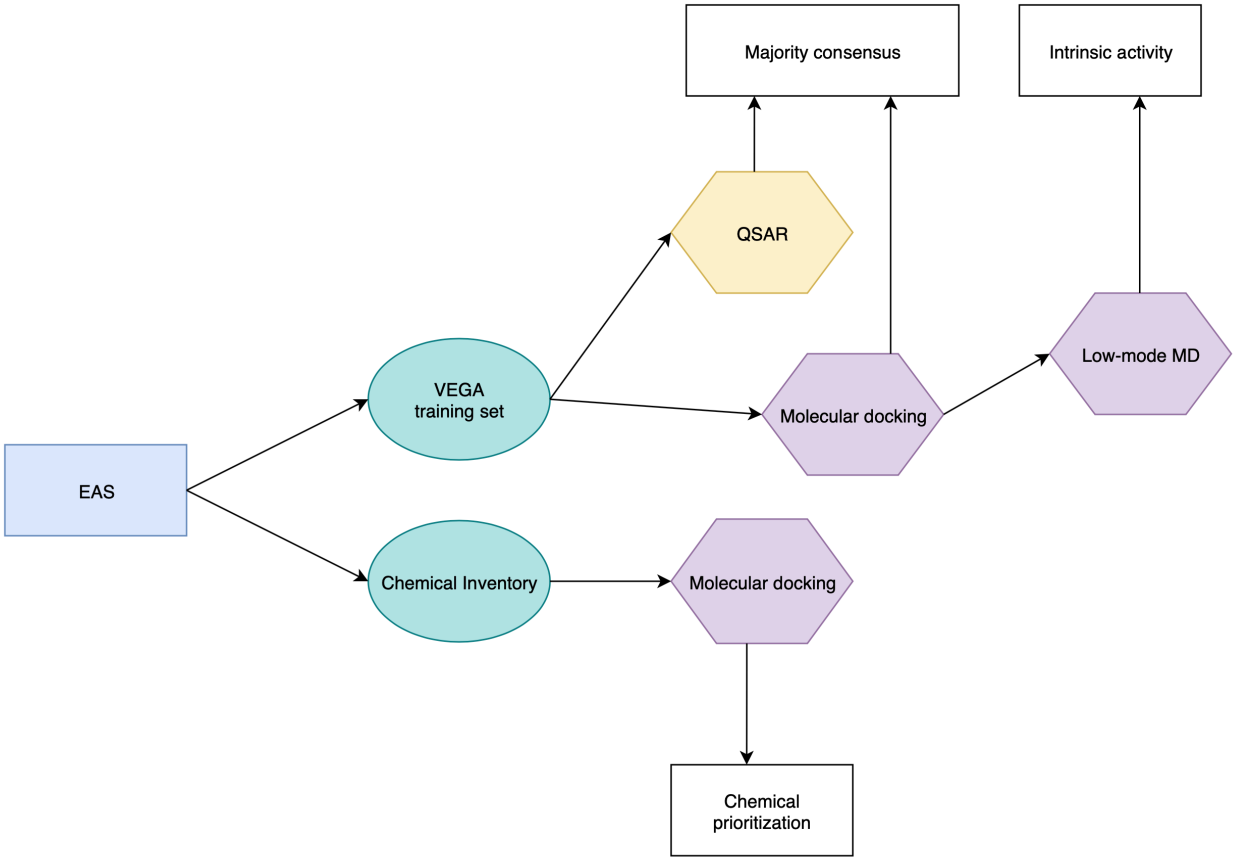

Figure 1: Endocrine active substances *in silico* pipeline. Yellow polygon represents ligand-based approach, while the violet polygons represent structure-based approaches. Endpoints are represented as white rectangle.

Part I – VEGA training set

These results have already been published in Cotterill, Palazzolo et al. (2018), that we published in the EuroMix framework.

Introduction

Exposure to endocrine disrupting chemicals (EDCs) has been linked to an increase in reproductive problems, hormone-dependent cancers, diabetes and obesity (Diamanti-Kandarakis *et al*., 2009; Piparo and Worth, 2010; Schug *et al*., 2011, Vuorinen *et al*., 2013). There are diverse and complex mechanisms of endocrine disruption, including direct activation or inactivation of key endocrine target receptors such as estrogen, androgen, progesterone and several corticosteroid receptors, as well as disruption of hormone synthesis and inhibition or activation of hormone metabolizing enzymes such as hydroxysteroid dehydrogenases.
The majority of research on EDCs has been based on interactions of compounds with nuclear hormone receptors (NR), especially estrogen receptors (ERα and ERβ) and the androgen receptor (AR). Potential EDCs are often identified by *in vitro* and *in vivo* screening tests (Borgert *et al*., 2011), however this approach can be time-consuming and expensive. *In silico* screening is far quicker and has lower cost implications and so can be a valuable tool for prioritising potential EDCs for further biological evaluation. Additionally, *in silico* screening can be applied to substances that are not synthesized (yet) or which would have physico-chemical properties that make *in vitro* testing difficult and/or unreliable.
There is a range of *in silico* methods available to predict potential EDCs including (Q)SAR ((Quantitative) Structure Activity Relationships), Read across, molecular docking, pharmacophore modelling and virtual screening (Diaza *et al*., 2012; Porta *et al*., 2016). Although most methods will classify compounds as either binders or non-binders of a particular receptor, methods such as molecular docking and some methods in the Endocrine Disruptor Knowledge Base (EDKB) (Ding *et al*., 2010) can provide a quantitative estimate of the binding strength (Galli *et al*., 2014; Trisciuzzi *et al*., 2017). On the other hand, molecular dynamics simulation allows to evaluate the intrinsic activity of a chemical bound to a nuclear receptor. There are pros and cons to the different approaches. (Q)SARs are quick and easy to run but individual models have a limited chemical space i.e. the types of compounds which fall within the applicability domain of the models. Molecular docking is applicable to almost all compounds and is quantitative, however the more accurate methods required for toxicology, rather than the preliminary low accuracy pharmacology approach for large numbers of compounds, are more computationally intensive and time consuming (Trisciuzzi *et al*., 2005).
Recently a lot of effort is being put into the estimation of EDCs, for example the estimation of ER activity in a large-scale modelling project called CERAPP (Collaborative Estrogen Receptor Activity Prediction Project) (Mansouri *et al*., 2016). In this extensive project 48 QSAR models to predict ER activity, developed using a common training set of 1,677 compounds, were combined and evaluated using a validation set of 7522 compounds. There is also a large literature on using docking against ERα applied to toxicology in order to reduce animal tests. For example, Trisciuzzi *et al*. (2005) present a study on estrogen receptors by deriving *ad hoc* docking-based classification models to discern potential estrogenic from non-estrogenic activity. On the other hand, many authors used molecular docking simulations to evaluate both affinity and molecular recognition mechanism of chemical::ERα complexes in order to develop drugs (Maruthanila *et al*., 2018), test xenobiotics effect (Conroy-Ben *et al*., 2018; Pang *et al*., 2018; Ye and Shaw, 2019) or study the molecular recognition mechanism of endogenous ligands at an atomistic level (Li *et al*., 2019).

Estrogen Receptor binding is one of the endpoints being considered in the EU-funded project EuroMix (https://www.euromixproject.eu/), in which *in silico* predictions are being used as input in

the risk calculation of combined exposure to multiple chemicals, when experimental data are not available. Exposure can occur to a diverse range of compounds that may be present in mixtures in food and feed. These compounds include plant protection products, biocides, environmental pollutants, mycotoxins, alkaloids, non-intentionally added substances (NIAS), food contact and food additives. In the component-based approach to mixture toxicity assessment proposed by the EuroMix project, QSAR predictions are used as (lower tier) information to determine which substances are likely to contribute to similar toxicological effects, and therefore should be assessed together in Cumulative Assessment Groups (CAG). This CAG approach to mixture toxicity assessment is explained in the draft guidance on mixture toxicity risk assessment from the European Food and Safety Authority (EFSA, 2019) and information on this approach can be found at the EFSA website (http://www.efsa.europa.eu/en/topics/topic/chemical-mixtures). Also required in the proposed project risk assessment process are the relative potency factors of the compounds in the cumulative assessment group. As no single (Q)SAR method is likely to be capable of providing reliable predictions for such a wide range of compounds, an approach using a weight of evidence of estimates from a suite of *in silico* models was proposed. We identified a broad selection of (Q)SAR models which were fundamentally different to each other, i.e. built using different chemicals, types of data and using different approaches and algorithms, in order to enable a diverse range of compounds to be estimated with more confidence.
In the initial phase of the EuroMix project a simple Majority Consensus approach for the interpretation of multiple QSAR results was used. To test the validity of this approach a test set of compounds with experimental Relative Binding Affinity (RBA) data was evaluated and the predictivity of both the individual models and the Majority Consensus prediction was assessed. Experimental values from reporter gene (RA) assays (i.e. agonist-specific activation assays) were also examined to investigate whether false negatives were likely to be antagonists. In addition to the application of the (Q)SAR models, molecular docking was carried out and the binding energies of the test set compounds to the ERα receptor were determined; we also investigated whether the Majority Consensus of QSAR models correctly predicted the strongest binding compounds. As well as using Molecular docking data to provide an assessment of the strength of binding, we investigated using different binding energies as a cut off to determine whether a compound is a binder or non-binder and also how QSAR model and molecular docking results can be best combined according to a particular requirement, for example to minimise false negatives, or to obtain the highest accuracy. A few test compounds were also evaluated using low-mode molecular dynamics simulations to determine their intrinsic activity and to investigate whether some of the negatives from the QSAR Majority Consensus were actually ERα antagonists.

Results – Ligand based approach

Predictivity of individual (Q)SAR models and the Majority Consensus

The predictivity of the individual (Q)SAR models was variable, as expected; some models had high sensitivity and others had high specificity. The Majority Consensus gave very good results with an accuracy of 0.8 and a reasonably balanced sensitivity and specificity and a high NPV value (Table 1). The VEGA-RBA model gave slightly better results (higher Accuracy, Specificity and MCC, the same Sensitivity and a similar NPV value) than the Majority Consensus model. Although it could be argued that the VEGA-RBA model alone could thus be used instead of the Majority Consensus model, the consensus of a number of different models is likely to be suitable for a wider range of compounds, i.e. will have a broader applicability domain, and if a compound is out of the domain of the VEGA-RBA model, it may be predicted by other models.

(Q)SAR Model	Sensitivity	Specificity	Accuracy	MCC	NPV
COSMOS Nuclear Receptor model	0.85	0.40	0.55	0.25	0.83
DEREK Nexus	0.33	0.98	0.75	0.44	0.73
OCHEM estrogen receptor α agonists [a]	0.88	0.51	0.66	0.40	0.86
OECD QSAR Toolbox DART scheme (ER binding)	0.29	0.83	0.64	0.14	0.68
OECD QSAR Toolbox ER binding OR rtER alert	0.75	0.64	0.68	0.37	0.82
VEGA – RBA	0.77	0.88	0.84	0.64	0.88
VEGA – CERAPP [a]	0.73	0.68	0.70	0.40	0.82
Majority Consensus	0.77	0.82	0.80	0.58	0.87

Table 1: Cooper statistics and NPV values for individual (Q)SAR models and Majority Consensus predicting experimental Relative Binding Affinity.

Of the 52 compounds in the VEGA test set (please, see Material and Methods chapter for VEGA test set details) with active experimental RBA values, there were 12 compounds that were predicted to be non-binders by the majority QSAR Consensus. These compounds covered a range of chemical classes, including phthalates, benzaldehydes, organophosphate, organochlorine, dicarboximide, organosulfur and polycyclic aromatic hydrocarbons. These compounds were investigated further and Reporter Gene assay (RA) results values were obtained (Roncaglioni *et al*., 2008), the transcriptional activity values of which are positive for agonists only. From the RA data it was found that 10 of these 12 compounds were not able to activate the ER, which indicates that they may be antagonists. The remaining two compounds, which were not structurally similar to each other (2-hydroxy fluorene and 2,2-bis(4-aminophenyl)hexafluoropropane), are not indicated to be antagonists and so are potential false negatives.

Majority Consensus (Q)SAR prediction of the strongest binding compounds

Experimental values and Majority Consensus (Q)SAR predictions for all compounds with binding energies below -6.5 kcal/mol (50 compounds in total) were examined. Results show that, out of these 50 strongest binding compounds, which also had positive relative binding activity (RBA) experimental values, only 5 compounds were predicted by the Majority Consensus QSAR to be negative. In addition to the RBA experimental values, the data for the same compounds for the relative activity (RA) test (agonist only) were also considered. The RA experimental results for these 5 compounds were all negative. As the RA test is agonist-specific and RBA is general (could be agonists or antagonists) this result indicates that these 5 compounds are in fact ER antagonists. This suggests that the majority consensus QSAR approach has not missed any of the highest binding ER agonists in the validation set.

Results – Structure based approach

Molecular docking

From molecular docking to ERα, both the molecular poses and the free binding energies of the VEGA validation set were obtained. These energies ranged from -8.9 to 9.6 kcal/mol, with the ten strongest binders shown in Table 3. Eight of these ten compounds were classified as active from the RBA experimental values. Moreover, a free binding energy of -8.1 kcal/mol was calculated for 17β-estradiol, the endogenous hormone for ERα. Based on this value, it was possible to classify within the database how many compounds have a lower value of binding free energy (ΔG). As a result, only

7 compounds have a ΔG lower than -8.1 kcal/mol, of which 5 are classified as active, while 2 are classified as inactive, on the basis of VEGA RBA data.

CAS number	Chemical name	Binding energy [kcal/mol]	RBA Experimental value
17606-31-4	Bensultap	-8.9	Active
1816-85-9	11-Hydroxytestosterone	-8.5	Inactive
566-76-7	16-Hydroxyestrone	-8.3	Active
2772-45-4	2,4-Bis(dimethylbenzyl)phenol	-8.3	Active
67747-09-5	Prochloraz	-8.2	Inactive
71030-11-0	beta-Zearalenol	-8.2	Active
571-20-0	5alpha-Androstane-3,17-diol	-8.2	Active
104-43-8	4-Dodecylphenol	-8.0	Active
1476-34-2	6-Keto estrone	-8.0	Active
5447-02-9	3,4-Bis(benzyloxy)benzaldehyde	-7.7	Active

Table 2: Binding Energies for ten strongest binding compounds and experimental values

Cut-off values of binding energies used to class as binders or non-binders.

In order to investigate the binding free energy value to be used as a cut-off, regardless of the endogenous substrate value, an R-script was written to compute the sensitivity, the specificity and the accuracy of the docking procedure by changing cut-off value. Table 3 shows the values of the Cooper statistics, calculated for four different cut-offs. Based on accuracy, the optimal cut-off value is -6.5 kcal/mol, which corresponds to a 10*E-06 M for dissociation constant (K_i). Using this cut-off value, although the accuracy of prediction was close to 0.7, the Cooper statistics were not as good as for the QSAR Majority Consensus. All these data were obtained relating the binding free energy results with the RBA.

Cut-off (kcal/mol)	Sensitivity	Specificity	Accuracy	MCC	NPV
-5.5	0.87	0.38	0.55	0.25	0.82
-6	0.75	0.58	0.64	0.32	0.81
-6.5	0.54	0.77	0.69	0.31	0.76
-7	0.31	0.83	0.65	0.16	0.69

Table 3: Cooper statistics and NPV value for Molecular docking binding energy cut-off values to assign whether compounds are binders or non-binders.

The NPV values ranged from 0.69 to 0.82 using the cut-off values of -7 to -5.5 kcal/mol (Table 3) and so a value of -5.5 kcal/mol would minimize the false negative prediction. Considering also this term for molecular docking, a good compromise between accuracy and NPV would be a cut-off value of -6 kcal/mol, for which there is also a good sensitivity (0.75). For these reasons, in section 3.4 we also consider the cut-off of -6 kcal/mol for the majority consensus between (Q)SAR and molecular docking.

Majority consensus between methodologies

In order to highlight the weight of each model and to provide different scenarios for interpreting the results, a majority consensus between methodologies was evaluated. As a first step, the same weight as a single (Q)SAR model was associated to molecular docking. Using -6 kcal/mol as docking cut-off, two different scenarios were obtained considering a chemical "positive" if it was classified as "positive" in three or half of the models, respectively (Table 5). In the first case, we obtained a high sensitivity value of 0.87, maximizing the true positive rate, although the accuracy was reduced

compared to the majority consensus of QSAR models. In the second case there were more balanced Cooper statistics.
Using the same approach but with a -6.5 kcal/mol as binding free energy cut-off value, again where three or models were positive, we obtained a high sensitivity value of 0.83, minimizing the number of false negatives. Again, there were more balanced Cooper parameters when we considered a chemical "positive" if at least half of the models were positive.
Changing perspective and using the logical operator "OR", we considered a chemical "positive" if it was positive in least half of the (Q)SAR models OR positive for molecular docking (binding free energy below the cut-off). Using -6 kcal/mol as docking cut-off, an extremely high sensitivity value of 0.94 was obtained, but with a low specificity. Slightly more balanced Cooper statistics were obtained using the -6.5 kcal/mol as docking cut-off with the sensitivity still high (0.87). With these analyses we have shown that, depending on the requirement e.g. highest accuracy, or highest sensitivity to decrease the chances of false negatives, it is possible to combine the (Q)SAR and molecular docking results, providing a rational combined strategy to maximize terms of toxicological interest.

Methods	Sensitivity	Specificity	Accuracy	MCC
Majority Consensus using 7 QSAR models	0.77	0.82	0.80	0.58
Molecular docking cut off -6	0.75	0.58	0.64	0.32
Molecular docking cut off -6.5	0.54	0.77	0.69	0.31
Consensus including docking (-6 cut off) as one of the models (positive if half or more models positive	0.77	0.79	0.78	0.55
Consensus including docking (-6 cut off) as one of the models (positive if 3 or more positive)	0.87	0.63	0.71	0.47
Consensus including docking (-6.5 cut off) as one of the models (positive if half or more models positive)	0.75	0.81	0.79	0.55
Consensus including docking (-6.5 cut off) as one of models (positive if 3 or more positive)	0.83	0.66	0.72	0.46
Consensus half or more QSAR models OR docking positive (-6 cut off)	0.94	0.49	0.65	0.44
Consensus half or more QSAR models OR docking positive (-6.5 cut off)	0.87	0.63	0.71	0.47

Table 4: Cooper statistics combining the (Q)SAR model and molecular docking results under different scenarios.

Low-Mode Molecular dynamics simulations to determine intrinsic activity of ERα binders
To evaluate the procedure of LM-MD for identifying the intrinsic activity of some strongly binding compounds, i.e. whether agonists or antagonists, ten compounds were selected. Five likely agonists selected from the test set were the strongest binding compounds with positive RBA and RA experimental data and five possible antagonists selected were the negative compounds from the Majority Consensus QSAR, which had positive RBA data but negative results in the RA assay. In addition to these compounds, a full-agonist (17-beta-estradiol), an antagonist (4-hydroxytamoxifen) and the *apo*-form of ERα were tested, in order to have a solid background to work on considerations related to intrinsic activity.
As a first step, the *ab initio* flexible alignment with MOE Conformational Search program was verified, on the basis of the molecular structures of reference compounds (17β-estradiol and 4-hydroxytamoxifen). Subsequently, three reference conformations were computed (Figure 2) and verified, starting from the lowest energetic conformation of 17β-estradiol, 4-hydroxytamoxifen and

apo- form, respectively. Closed conformation of full-agonist corresponds to starting 3UUD conformation, while both partially open and completely open conformations, respectively for *apo-* and antagonist, have similar shape with respect to AR open conformation reported in Galli *et al*., (2014).

Figure 2. Superimposition of lower energetic configuration for agonist (green), antagonist (orange) and *apo-* form of ERα (light violet).

Through an R script, the RMSD of the first 100 conformations was evaluated for each generated complex, using as reference the 3UUD crystallographic structure in closed conformation. For the five selected putative agonists (Figure 3, left), we found that 2 compounds (V2 and V3) have low RMSD values, so they can be classified as full agonists, another 2 compounds (V4 and V5) have low RMSD values for approximately 70% of the generated poses, so they can be classified as partial agonists, while the last one (v6) has a RMSD value similar as the reference antagonist, so it could be classified as an antagonist. On the other hand, for the five selected putative antagonists (Figure 3, right), 4 compounds (V9, V10, V11 and V12) have RMSD values very high or comparable with the antagonist reference value, while 1 compound (V8) showed for approx. 50% of generated conformations a low RMSD value, comparable with the agonist value. In this case, we can assess that 4 compounds are antagonists, while the fifth is a weak partial agonist.

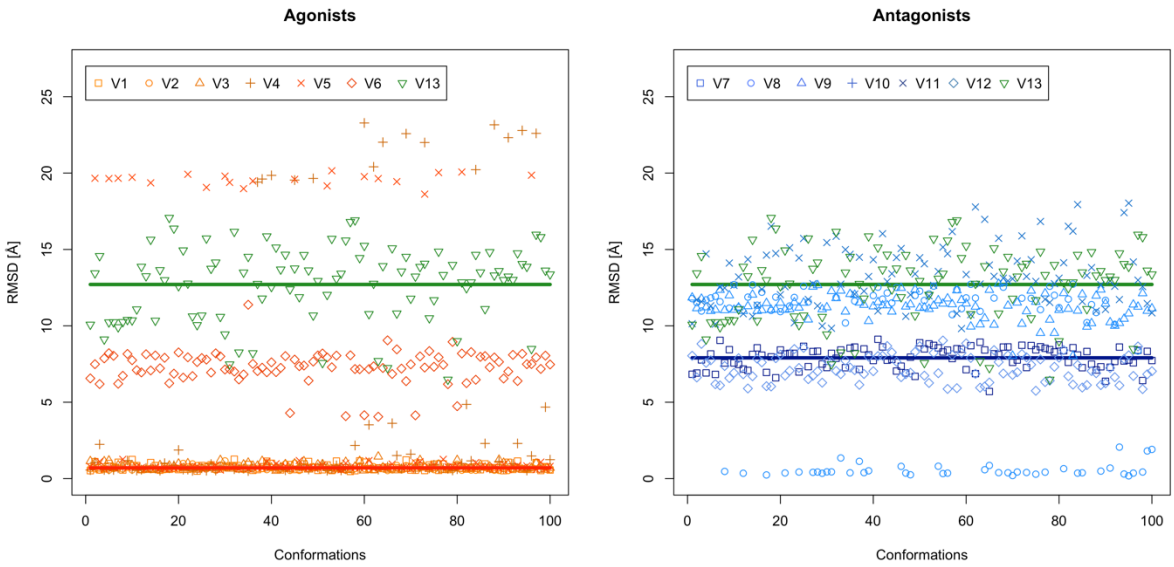

Figure 3. RMSD values for both putative ERα agonists (left) and putative ERα antagonists (right). Lines represent the reference conformations for agonists (red), antagonists (blue) and *apo*-ERα (dark green).

17-β Estradiol, the reference full agonist, has a median RMSD value of 0.67 Å, as does compound V2, whereas compounds V3-V5 have a median value of around 0.71 Å. Compound V6 has a median value of 7 Å, an order of magnitude higher than the reference agonist. On the other hand, 14-hydroxytamoxifen, the reference antagonist, has a median value of about 8 Å, while the compounds V8-V12 have a median value ranging from 7 Å to 18 Å. *Apo*-ERα has a median value of 13 Å. Compound V8, defined as very weak partial agonist, therefore presents a higher interquartile range, because of the dispersion of the generated configurations, which are in part those of an agonist, in part those of an antagonist. A box plot of the RMSD of the generated complexes is shown in Figure 4.

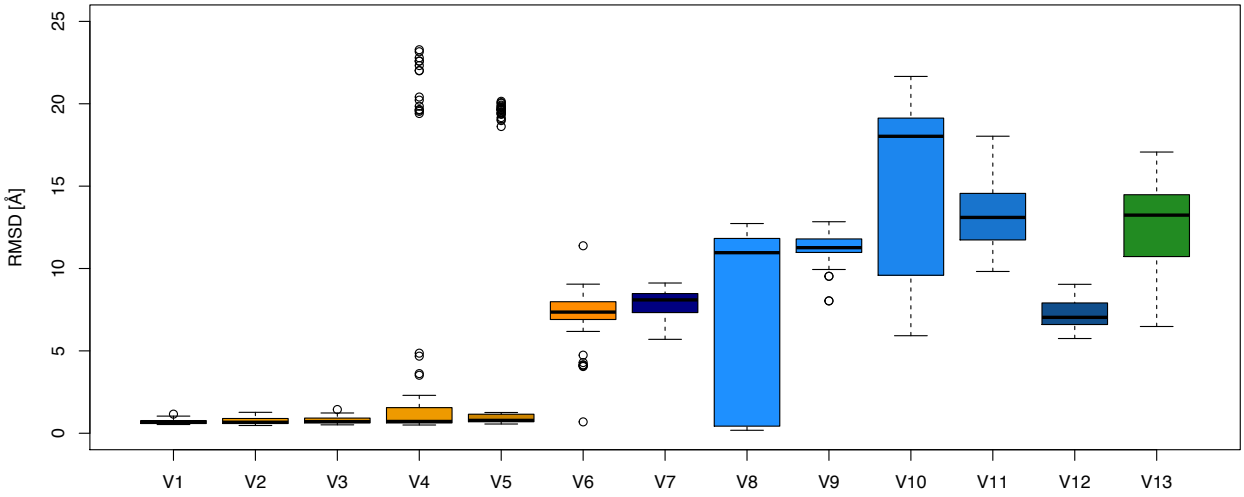

Figure 4. Box plot of the RMSD of the generated complexes. Reference agonist (V1) and putative agonists (V2-V6) are coloured in orange, while reference antagonist (V7) and putative antagonists (V8-V12) are coloured in blue. Apo-ERα (V13) is coloured in green.

Discussion/Conclusions

The approach of using the results from a suite of *in silico* models which account for different ER binding related endpoints, are built from different compounds and using different methodologies, has the advantage of increasing the chemical space covered and thus the probability that any active compounds from diverse classes of chemicals such as those considered in the EuroMix project will be correctly identified. Weight of evidence from different (Q)SAR models has been successfully used for a number of toxicological endpoints. For example, Price and Chaudhry (2014) showed that this approach using different *in silico* models can provide a rapid and reliable means of rapid screening for mutagenicity and carcinogenicity for compounds that may migrate from food packaging. Hewitt *et al*. (2010) and Marzo *et al*. (2016) integrated *in silico* models to enhance predictivity for developmental toxicity. Benfenati *et al*. (2015) integrated QSAR and Read-across results for the assessment of bioconcentration factors of chemicals. Again, Benfenati *et al* (2019) showed that there are several ways to integrate results of multiple in silico methods, recognising that integration of the

results from different (Q)SARs and other in silico tools can improve the overall confidence in the predicted estimates.

In attempting to identify substitute compounds for known phthalate, bisphenol and parabens EDCs, Porta *et al*. (2016) applied a battery of different models, along with EC priority lists and other rule sets derived from authority's opinions. Similar to Porta *et al*. (2016), we selected models which are fundamentally different from one another, i.e. they were developed using different chemicals, using experimental results from a range of different assays and thus different ER binding endpoints, and using different methodologies (e.g. QSAR models generated using molecular descriptors by a range of algorithms, SARs using molecular fragments etc.), in order to enable a diverse range of compounds to be estimated with more confidence. The (Q)SAR models used in the EuroMix project were however also selected on the basis of being readily available and implemented into software programs, easy to use and with the benefit of being able to run in batch mode and thus of being able to screen large numbers of compounds.

The results showed that individual (Q)SAR model predictivity varied, as expected, with accuracies ranging from 0.55 to 0.84. Some models such as the COSMOS Nuclear Receptor and OCHEM models showed high sensitivity, whilst others such as DEREK Nexus and the OECD Toolbox DART scheme alert showed very high specificity. The Majority Consensus prediction shows a high accuracy (0.8) as well as well-balanced sensitivity and specificity.

To further investigate the false negative predictions from the QSAR Majority Consensus, experimental values from reporter gene (RA) assays (an agonist-specific assay) were obtained for these compounds. The vast majority of these compounds had negative RA values, which indicates that these compounds may be ER receptor antagonists. As the (Q)SAR models covered a range of ER-compound interactions, including relative binding to, and activation of the ER, then although the Majority consensus used in the study predicts well ER interaction in general, it is perhaps not surprising that it appears to be less predictive for antagonists, as no specific ER-antagonist QSAR models were used in the study.

Molecular docking was also used to provide quantitative information on the strength of binding to the ERα receptor, thus allowing to derive first-tier estrogenic potencies in the EuroMix project. Using a range of cut-off values of binding energies to predict whether a compound is a binder or non-binder, Cooper statistics showed that a threshold of -6.5 kcal/mol produced the highest accuracy. Using the molecular docking energies with the threshold value for predicting ER binding vs. non binding had a lower accuracy than the QSAR Majority Consensus approach, but it provided invaluable (quantitative) information on the strength of receptor binding. Finally we demonstrated that using Molecular docking cut-off values to assign ER binding can be combined with (Q)SAR results either as an additional *in silico* model in an overall consensus, or to assign a compound as an ER-binder if either the (Q)SAR Majority consensus was positive OR the Molecular docking classified it as a binder, for example if it is desired to optimise the sensitivity of the model (at the cost of overall accuracy) to reduce the chances of false negative predictions.

Further investigations on the 50 highest binding affinity compounds showed that the QSAR Majority Consensus correctly predicted these compounds to be binders in 90% of the cases. Of all compounds with positive RBA experimental values, only 5 were predicted as non-binders by the QSARs. Furthermore, the experimental values from RA assays for these 5 compounds were all negative, indicating that the negatives from the consensus of QSARs may be ER antagonists. Low Mode Molecular dynamics simulation was used to determine intrinsic activity of these negative compounds, together with 5 likely agonists, and the results were mostly consistent with expectation. Four of the five proposed agonists were confirmed as such (16-Hydroxyestrone, Zearalenol, Androstane17-diol and 4-Dodecylphenol) and four of the five proposed antagonists were confirmed as such (3,4-Bis(benzyloxy)benzaldehyde, Chlorpyriphos, 2-(4-Chlorophenyl)-1,1-diphenylethanol and Captafol).

QSAR models are available which can provide quantitative estimation of ER binding (e.g. those developed in the CERAPP project (Mansouri *et al*., 2016)), which could also be used to provide strength of binding estimates, in addition to, or instead of, the Molecular docking results. Similarly, QSAR models have been developed to predict ER agonists or ER antagonists, rather than binding in general (e.g. Mansouri *et al*., 2016), which could be used in place of the Molecular Dynamics simulations to identify if a compound is an agonist or antagonist.

Overall the results show that the Majority Consensus of the (Q)SAR models is a good method to predict whether a compound is an ER-receptor binder or non-binder. It predicts ER binding well for the majority of the highest binding compounds and the majority of the relatively few false negatives may be antagonists. This method has the benefit of being quick to provide results, being simple to use and is based on readily available (Q)SAR models. Compounds predicted positive by QSARs could then be screened by molecular docking to assess whether they are weak or strong binders. We also showed different scenarios of combining (Q)SAR results with Molecular docking classification of ER binding based on cut-off values of binding energies, providing a rational combined strategy to maximize terms of toxicological interest, for example to minimise false negatives. As complementary approach, low-mode MD can be applied to distinguish between agonists and antagonists, improving both the (Q)SAR- and molecular docking-related information. A logical improvement over a simple Majority Consensus approach of interpreting multiple (Q)SAR predictions would be to consider the individual predictive performance (sensitivity, specificity) of the (Q)SAR models and apply Bayesian statistical theory. Examples of application of this approach are e.g. in Rorije *et al*. (2012) and Buist *et al*. (2012). In this case the predictive results from the Majority Consensus approach are such that not much improvement was expected and hence Bayesian statistics were not applied.

Results – Structure-based approach

The crystallographic structures of 4 endogenous hormone receptors are excellent 3D structures on which perform both molecular docking and low mode simulations. No outliers are found on the Ramachandran Plot analysis for the 4 structures, which are correctly superimposed with calculated RMSD values on the alpha carbons of the entire sequence, LBD included, ranging [0.97, 1.60] Å. Figure 5 shows the superimposed structures (left) of NR for sexual hormones and their respective RMSD values (right), from which it can be observed that the LBD of estrogen receptors (#5 and #7 on legend) are those with the lowest RMSD.

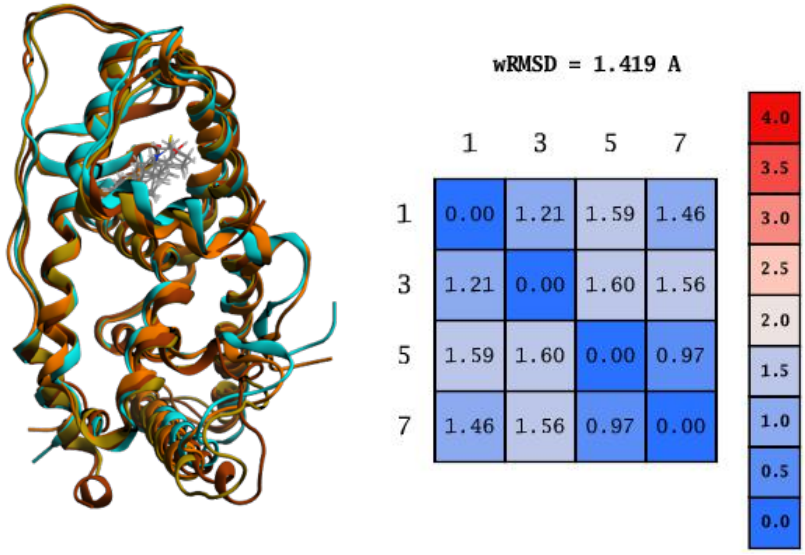

Figure 5. (left) Superposition of AR, PR, ERs LBDs and their respective co-crystallized ligand. (right) RMSD values of superimposed 3D protein structures.

The α-spheres-defined binding site coincides with that defined by co-crystallized hormones, which is closed by some α-helices, including the 12th, and two β-sheets. As an example, Figure 6 shows the molecular surface of the ERα binding site whose secondary structure has been annotated using the specific MOE Module.

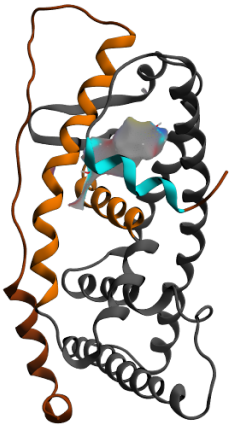

Figure 6 ERα LBD crystal structure on which binding pocket molecular surfaces was calculated and showed.

Table 5 reports the number of chemicals with estimated binding free energy lower than the cut-off value, either from SSA statistic on VEGA dataset or from biochemical evaluation of endogenous hormone binding.

Nuclear receptor	**Cut-off -6.5 kcal/mol**	Cut-off ΔG of endogenous hormone
PR	323	20
AR	194	2
ERα	352	28
ERβ	309	57

Table 5. Number of prioritized chemicals with two different cut-off values (toxicological and biochemical) for each NR selected for EAS.

Considering the first cut-off value, it was found that 30%-35% of the CI compounds bind the estrogen and progesterone NRs with binding free energy values lower than -6.5 kcal/mol, whereas only 20% bind the androgen receptor. Some of these compounds bind transversally all the four NRs; this is the case of compounds #631 and #642 (which are found to be top scoring for both progesterone and androgens). On the other hand, some compounds are selective for estrogen (e.g. compound #669), for progestogens (e.g. compound #503) or for androgens (e.g. #519).
Considering the cut-off values given by the free binding energies of sex hormones on their respective receptors (Table 11), very different scenarios were obtained. For AR, there are only two compounds with ΔG lower than testosterone binding free energy, whereas between 2% and 5% of the compounds have a ΔG lower than that of progesterone for binding PR and of 17β-estradiol for binding ERα and ERβ, respectively.
From a biochemical point of view, these compounds can bind their nuclear receptors at the same concentration as the reference sexual hormones, occupying their binding site. On the basis of the the dissociation constant (K_i) evaluated for the top scoring compound on each receptor (Table 6), concentrations of about 10 nM of the prioritized compounds are sufficient to occupy half of the nuclear receptors and, thus, possibly cause adverse effects.

	PR	AR	ERα	ERβ
Endogenous hormone	-8.1	-9.2	-8.1	-7.7
Top scoring	-10.1	-9.6	-10.1	-9.9
Ki – Top scoring	3.7e-08	8.6e-08	3.7e-08	5.2e-08

Table 6. Binding free energies of endogenous hormones and top scoring compounds for each NR. Dissociation constant of top scoring compounds are also reported.

Figures 7-10 show the docking poses of endogenous hormones in their cognate receptors as well as the framework of their interactions with key amino acids.

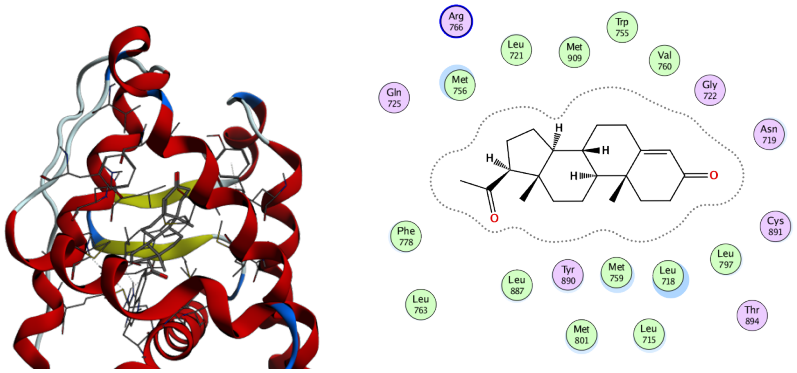

Figure 7. Docking pose of PR:: progesterone (left) and key amino-acids involved in binding (right).

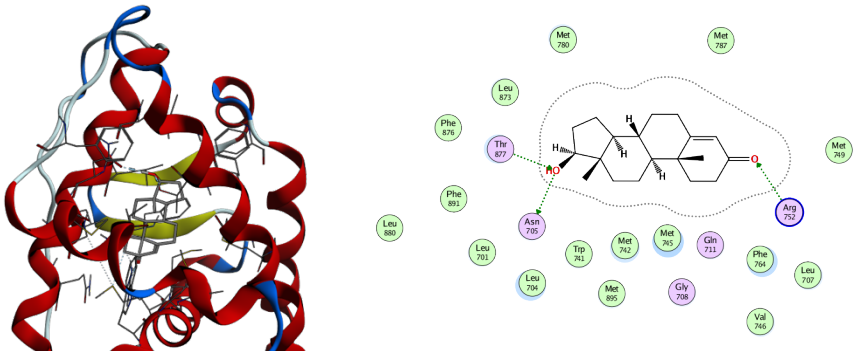

Figure 8. Docking pose of AR:: dihydrotestosterone (left) and key amino-acids involved in binding (right).

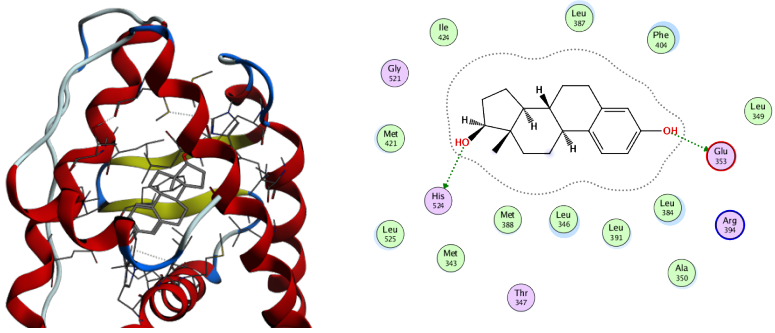

Figure 9. Docking pose of ERα:: 17β-estradiol (left) and key amino-acids involved in binding (right).

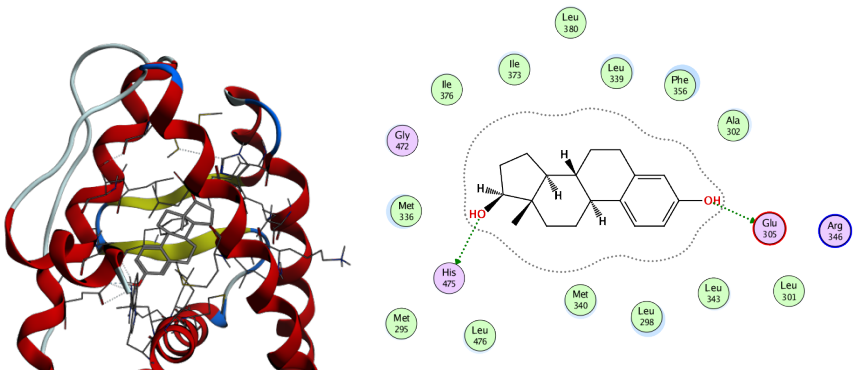

Figure 10. Docking pose of ERβ:: 17β-estradiol (left) and key amino-acids involved in binding (right).

Discussion/Conclusions

From our results, AR is the least sensitive receptor to the compounds present in the CI, whereas ERβ is the most sensitive. In fact, for AR, considering as cut-off the ΔG between the endogenous hormone and the tested chemical, we found that only 2 chemicals have binding free energies lower than dihydrotestosterone. This is partially due to the fact that he binding free energy of endogenous hormones is -9.2 kcal/mol, the lower with respect to the other hormones, but also to the high selectivity of the AR binding pocket. On the other hand, ERβ seems to be the most sensitive to the interferences due to the CI because the binding free energy of its reference hormone is -7.7 kcal/mol. Considering a cut-off value of -6.5 kcal/mol, PR, ERα and ERβ binds approx. the same number of chemicals, suggesting that these receptors are more exposed to EAS effects.
All the prioritized chemicals were further studied both *in vitro* and *in vivo* by EuroMix partners, and the results of these studies are published in EuroMix Deliverables on EuroMix web page (https://www.euromixproject.eu/).

Chapter 2 – Reproductive toxicity

Retinoic Acid (RA) is a small diffusible lipophilic molecule derived from vitamin A (*retinol*), an essential vitamin derived from food of animal origin and carotenes. RA is involved in many embryonic and adult physiological processes and functions, such as: differentiation and development of fetal and adult tissues (Rhinn and Dolle, 2012), stem cell differentiation and apoptosis (Noy, 2010), support of reproductive functions (Chung, Wang, and Wolgemuth, 2009), immune response (Ross, 2013), regulation of energy homeostasis (Villarroya, Giralt, and Iglesias, 1999; Herman and Kahn, 2006) and brain functions (Ransom *et al*., 2014). RA is removed by microsomal enzymes belonging to the Cytochrome P450 (Cyp450) family, which represent an additional level of control of RA availability through tissue-specific oxidative metabolism. Three members of this enzyme class are believed to be the major responsible for RA degradation: CYP26A1, CYP26B1 and CYP26C1, all of which oxidize, with the help of cytochrome P450 reductase (POR), RA into more polar metabolites, namely: 4-hydroxy- and 4-oxo-retinoic Acid (Chithalen *et al*., 2002).
All of the three CYP26 isoforms show complex tissue- and time-specific patterns of expression and genetic ablations of either CYP26A1, CYP26B1, CYP26C1 or their redox partner POR (Ribes *et al*., 2006) lead to defects consistent with an increase in RA signalling.

- CYP26A1 is the first to be expressed (E6.0) in extraembryonic and embryonic endoderm, and at E7.5 is expressed in the head mesenchyme and neuroectoderm, where it is essential for neural antero-posterior patterning (Uehara *et al*., 2007; White *et al*., 2007). CYP26A1-/- mice display truncation of the posterior body region, abnormal hindbrain patterning and transformation of cervical vertebrae (Abu-Abed *et al*., 2001).
- CYP26B1 is found within E9.5–E12.5 in the limb buds, where it is required for proper proximal-distal outgrowth (Yashiro *et al*., 2004); accordingly, CYP26B1-/- mutants exhibit severe limb mal- formations and facial abnormalities (Maclean, Dollé, and Petkovich, 2009).
- CYP26C1 is expressed in the head mesenchyme at E7.5, otic vescicles, branchial arches and, after gastrulation, appears within the hindbrain (Reijntjes, Gale, and Maden, 2004). CYP26C1-/- loss-of- function embryos are viable, although compound inactivation of any other CYP26 results in early embryonic patterning defects: ablation of CYP26A1 and CYP26C1 is lethal within stages E9.5–E10.5 and double-knockout mice show abnormalities in forebrain, midbrain, branchial arches (which are reduced), hindbrain (expanded) and lack of cranial neural crest (Uehara *et al*., 2007).

RA's metabolites have the potential of being biologically active and induce, on certain targets, responses similar to those of RA (Reijntjes *et al*., 2005). However, it is likely that these degradation products are removed and/or form inactive conjugates fast enough not to reach significant concentrations *in vivo*, since both expression data and functional studies indicate that the role of CYP26-mediated RA metabolism is essentially to prevent inappropriate signalling (Pennimpede *et al*., 2010).
The aim of this chapter is to investigate effects of chemicals able to interfere with the retinoic acid pathways, and to provide information about three different approaches, applied to toxicology: structures-based approach, dynamic (PD) modelling and physiologically based pharmaco-kinetic (PBPK) modelling.

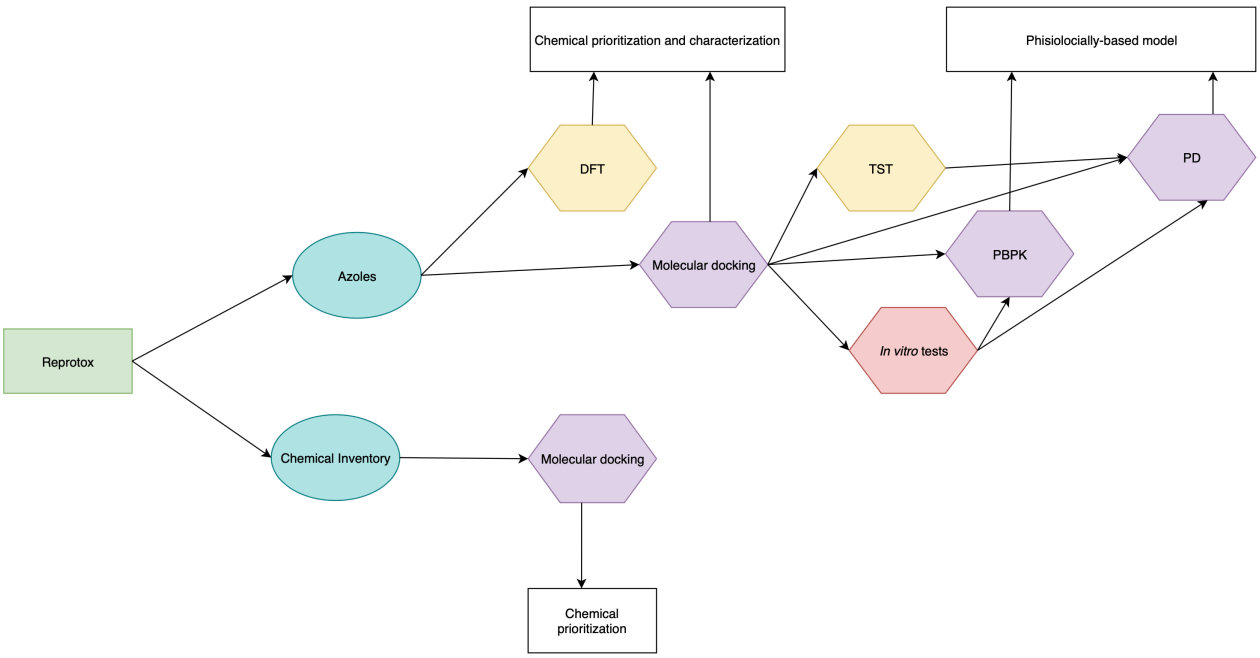

Figure 11: I*n silico* pipeline for reprotox. Yellow polygons represent the ligand-based approaches, the violet polygons represent structure-based approaches (including PD and PBPK), while red polygon represent the *in vitro* experiments. Endpoints are represented as white rectangle.

Part I – Azoles as training set

Introduction

Azoles are synthetic antifungal compounds, derived from triazole or imidazole, that are used for control of fungal pathogens both in humans and in plants thanks to their broad spectrum of antifungal activity and their relatively long persistence. Certain azoles are teratogenic causing the craniofacial malformations (Menegola *et al*., 2006; Marotta & Tiboni, 2010) possibly because they inhibit CYP26 isoenzymes (CYP26A1, CYP26B1 and CYP26C1) that catabolize retinoic acid (RA) during early embryonic development (Marotta & Tiboni, 2010; Ray *et al*., 1997). CYP26 isoforms belong to the Cytochrome P450 super-family and are expressed in discrete regions (rombomers) of rhombencephalon during embryo development. They are involved in the RA-mediated signalling modulation, which is essential in cells to promote the expression of specific genes, expressed during the development of branchial arches (Niederreither *et al*., 2000). In fact, RA concentration is dynamically governed by local tissue-specific synthesis and degradation reactions. In particular, RA is synthesized in a two-step reaction from retinol, catalysed by retinol dehydrogenases (RDHs) and retinaldehyde dehydrogenases (RALDHs), and it is metabolized by CYP26 enzymes (Sandell *et al*., 2012). Disruption of this biochemical pathway can induce specific malformations due to the selective inhibition of specific CYP26 isoforms. Azoles can act either as competitive inhibitors or as CYP26 substrates, binding in both cases to the same active site, in the proximity of the Cyp heme group. Under steady state conditions, binding of azoles to CYP26s reduces the number of free enzymes for RA catabolism, increasing the substrate concentrations and altering RA dynamics and secondary pathway.
Literature reports that the azole ring is oriented toward the heme and, with the exception of tebuconazole that creates specific interactions with heme through the amine group (Mercadante *et al*., 2014). The oxidized metabolite of tebuconazole has been observed by Marcadante *et al* (Mercadante *et al*., 2014) and metabolite structures of other azole are reported in literature, in which azole ring is not involved in metabolism, while Fluconazole is the only non-metabolized azole (Humphrey *et al*., 1985).
However, it is necessary to distinguish between competitive inhibitors and substrates, because the enzymatic kinetics are different. Enzymatic kinetics depends both on binding capability and on xenobiotic concentration, which changes with time. If a xenobiotic acts as substrate, it is catabolized by enzymes increasing its elimination rate, while if a xenobiotic acts as a competitive inhibitor, it is only eliminated by other routes (e.g. excretion).

Results – Ligand-based approach

Semi-quanto mechanics

Three sites of metabolism (SOMs) were computed using SMARTCyp for each compound.
Figure 12 shows retinoic acid SOMs. The second predicted SOM is depicted in blue, which corresponds to carbon 4 that is the observed RA site of metabolism.

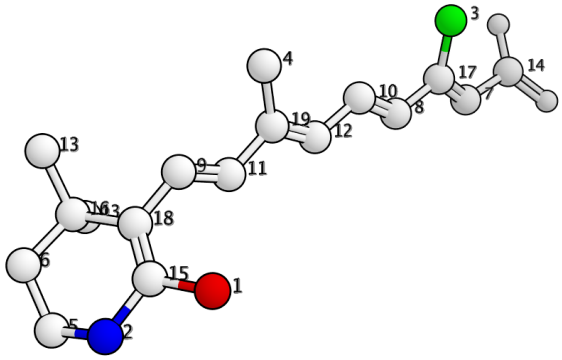

Figure 12. Retinoic acid predicted SOM. Red, blue and green points represent the first, the second and the third SOM.

On the other hand, the best SOM of each azole, except tebuconazole, corresponds with the heme nearest atom, computed through molecular docking simulation. Figure 13 shows the results for fluconazole (left) and tebuconazole (right): in the first case, the first and the third SOM correspond to the closest atom to the heme group; in the second case the SOM reported in literature results to be ranked as eighth predicted SOM. These two azoles will be taken as case studies, in order to compute transition state energy of the first predicted SOM and to verify that both values will be unfavourable for reactions, setting two true negative energetic cut-offs.

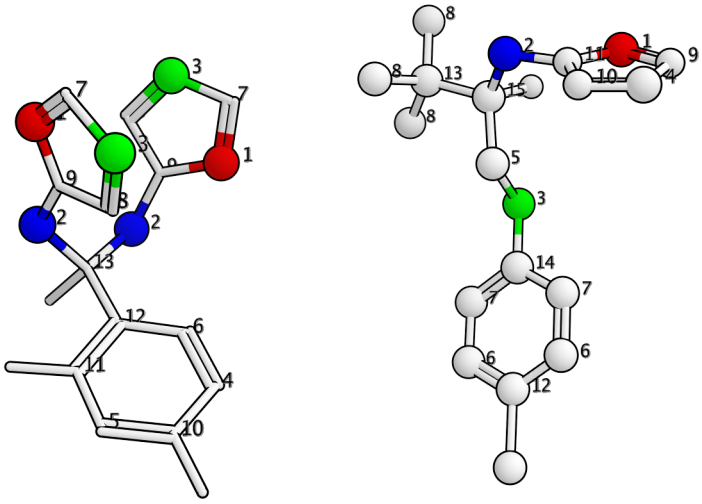

Figure 13. Fluconazole (left) and Tebuconazole (right) predicted SOM. Red, blue and green points represent the first, the second and the third SOM, respectively.

Transition state theory

The transition state of RA was obtained starting from hand-designed reagents and products. From this configuration, it is possible to observe the loss of hydrogen by the RA and to calculate the energy value through a single point in DFT. From this value (which corresponds to the reaction potential barrier) and from those computed from the products and reagents (which compose the initial and final states) it has been possible to calculate energy differences and to assess whether the transition is allowed. The course of the reaction from substrates to products is outlined in Figure 14.

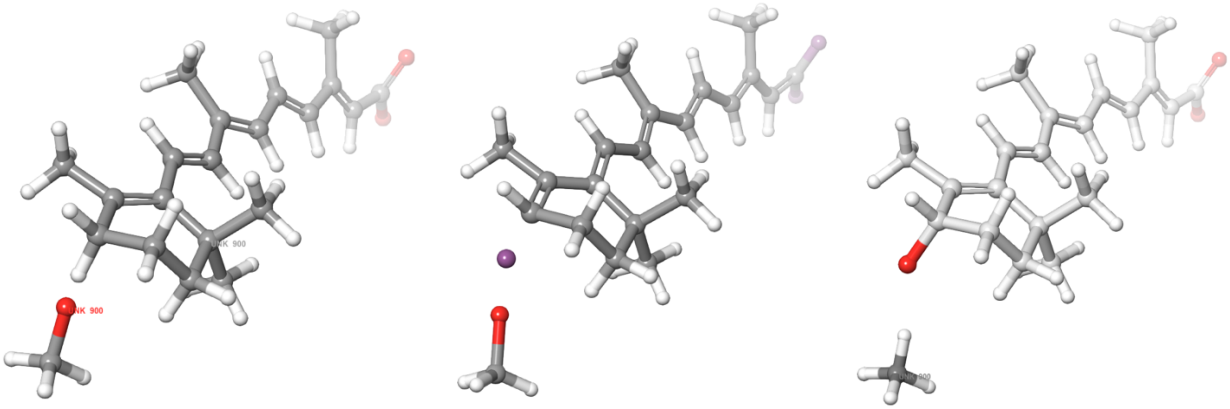

Figure 14. Reactants (left), transition state (centre) and products (right) of RA. Transition state is a computational result, while reactants and products were manually built.

Results – Structure-based approach

Molecular docking

For azoles, RA and thanol, each docking pose was carefully evaluated for the three different isoenzymes of rat CYP26, selecting the correct placements that match the geometric constraints reported in Li *et al* (Li *et al*., 2011). Globally, the binding free energy value for RA bound to the three different isoforms was used as discriminant to detect which compounds bind with lower energy. At the same time, the value of solvation (MMGBSA) was considered in order to cluster these compounds and to depict homogeneous subsets as for binding capability.

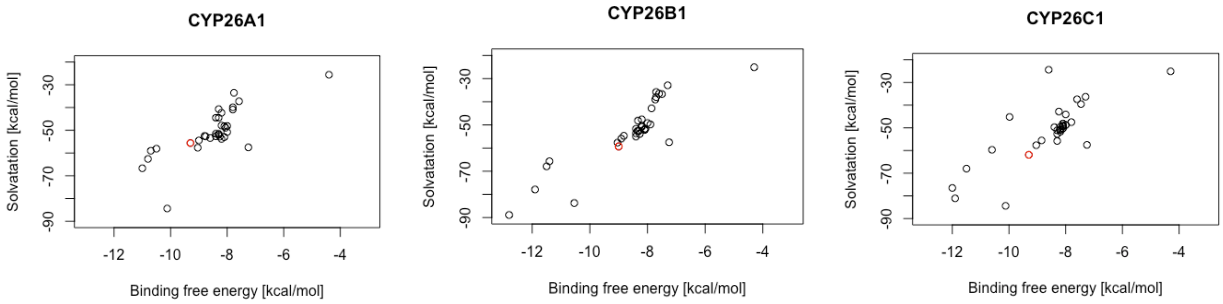

Figure 15. Clustering of chemicals for each rat CYP26 isoenzyme on the basis of both binding free energies and of solvation values.

Figure 15 shows the clustering of the chemicals, on the basis of solvation and binding free energy values. Retinoic acid is highlighted in red and is taken as reference. In the first analysis, all compounds on the bottom-left (with respect to RA point) are compounds that can potentially have more evident toxic effects on foetus development if compared to the top-right compounds.
Ethanol, characterized by binding free energies of about -4/-5 kcal/mol, has a very small molecular surface and the possibility for this compound to act cooperatively is currently being considered. Figure 16 shows the docking pose for RA, while Figure 17 depicts the docking pose of a single ethanol molecule, on whose basis the second calculation is being performed.

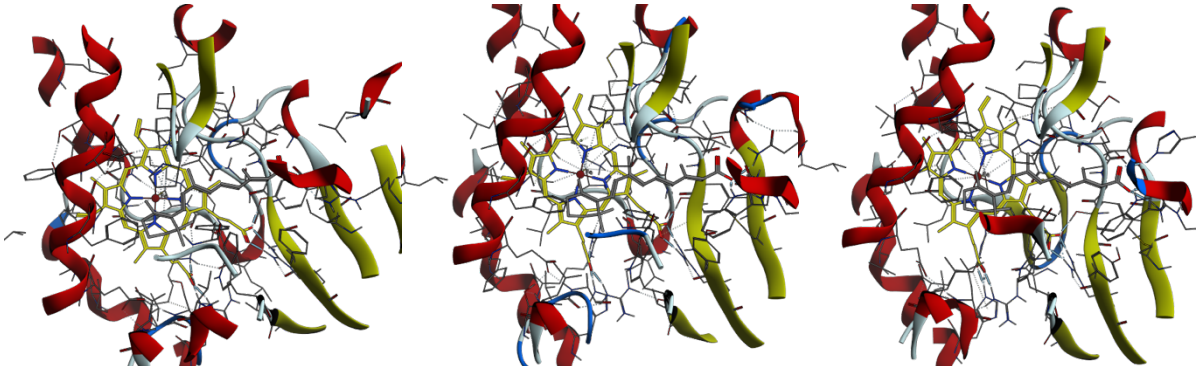

Figure 16. Retinoic acid docking poses on CYP26A1, CYP26B1 and CYP26C1, respectively to the left, centre and right. C4 of RA is placed near the heme (yellow) in each isoform as reported in literature (Li *et al*. 2012).

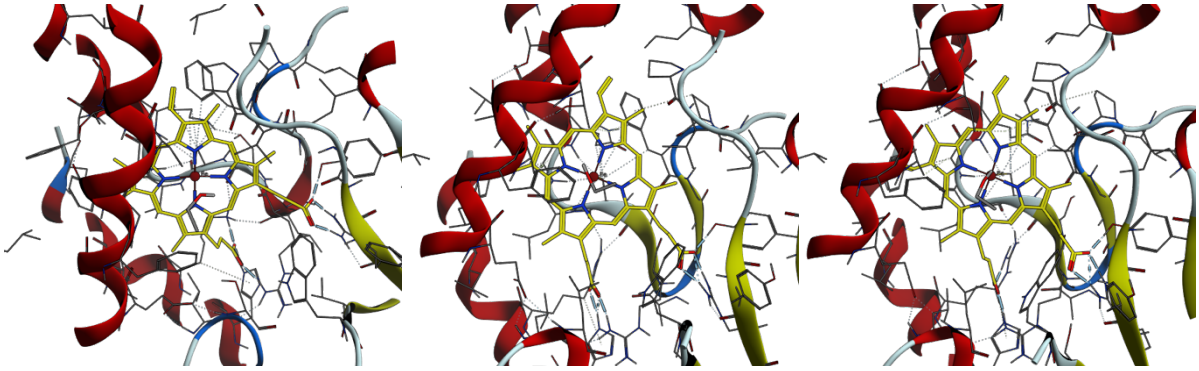

Figure 17. Ethanol docking poses on CYP26A1, CYP26B1 and CYP26C1, respectively to the left, centre and right. It is placed in contact with the heme (yellow) in each isoform.

All azoles show the azole ring in contact with the heme as preferential placing, except to the tebuconazole, which shows the methyl group in contact with the heme, according to Marcadante *et al* (Figure 18).

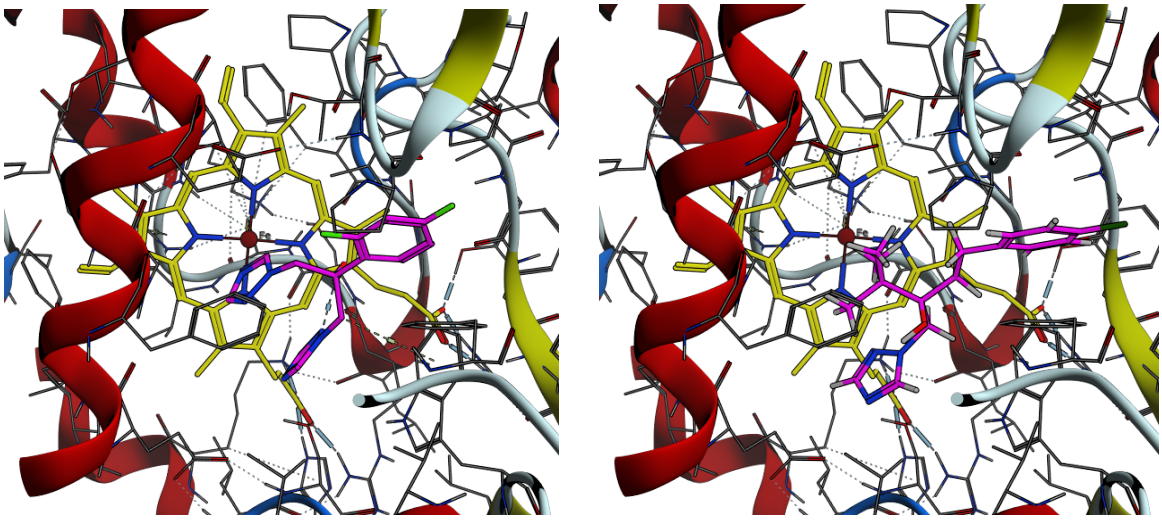

Figure 18. Left: Fluconazole docking pose on CYP26A1. The fluconazole (violet) azole ring is in contact with the heme (in yellow) of the CYP26A1. Right: tebuconazole docking pose on CYP26A1. The tebuconazole (violet) methyl group is in contact with the heme (in yellow) of the CYP26A1.

Discussion/Conclusions

Considering all the azole docking poses, all the Cyp::azole complexes are not compliant with the geometry restraints suggested by Li et al. (2011):

- *the distance between the selected atom and the ferryl oxygen is outside the optimal range which is from 1.65 to 2.60 Å for sp3 atoms and from 1.60 to 2.08 Å for sp2 atoms;*
- *the distance of the basic nitrogen to the ferryl oxygen is less than 4.8 Å;*
- *the distance of any polar atom to the ferryl oxygen is less than 3.2 Å;*
- *more than 2 heavy atoms from the ligands are either further than 14.5 Å or closer than 1.6 Å from the heme iron;*
- *The pose has at least 1 distorted cyclohexane ring*.

In this context, we decided to consider all the tested azoles as inhibitors and not as substrates, disregarding the TST calculation for each azole.
Globally, all the selected azoles seem to be good binders of Cyp26 isoforms, and ketoconazole, itraconazole and posaconazole are the most interesting chemicals that may interfere with the retinoic acid pathway. These results agree with toxicological literature and other EuroMix observations (Battistoni et al., 2018), in which azole-inducted cranio-facial malformations were studied.

All the *in silico* results about azoles were shared with the EuroMix partners to better understanding their effect on both *in vitro* and *ex vivo* systems.

Results – Structure-based approach

The BLAST template search, using as queries the three CYP26 isoforms for human (hCYP26), rat (rCYP26) and zebrafish (zCYP26), identified the crystallographic structure of the Retinoic Acid-bound Cyanobacterial Cyp120a1 (PDB ID: 2VE3) as the best scoring template in the PDB database. Sequence identities and sequence similarities are reported in Figure 19.

	1	3	5	7	10	13	15	18	21	23
1:2VE3.A		32.8	34.1	32.9	33.9	34.5	35.9	33.8	33.3	31.2
3:Cyp26a1	33.8		92.3	70.4	45.2	45.9	45.5	45.2	44.3	41.1
5:G3V861	34.9	91.7		69.6	45.4	45.9	45.3	44.3	43.8	40.3
7:P79739	33.3	69.4	68.9		43.7	43.7	43.3	43.7	43.0	41.1
10:Cyp26b1	34.2	44.4	44.9	43.6		95.8	74.6	53.1	52.3	53.0
13:G3V7X8	34.9	45.1	45.4	43.6	95.8		75.9	54.6	53.6	53.6
15:Q6EIG3	36.3	44.6	44.7	43.1	74.4	75.7		54.8	52.9	52.4
18:Cyp26c1	35.6	46.2	45.6	45.3	55.2	56.8	57.1		87.7	55.8
21:D4AAL3	34.7	44.9	44.7	44.2	53.9	55.2	54.7	86.9		54.2
23:A1L1M2	34.9	44.6	44.1	45.3	58.6	59.2	58.0	59.3	58.1	

	1	3	5	7	10	13	15	18	21	23
1:2VE3.A		51.9	53.1	54.2	54.3	54.6	54.5	51.2	52.3	48.8
3:Cyp26a1	53.4		95.4	82.4	63.5	64.1	63.4	60.8	62.0	57.5
5:G3V861	54.3	94.7		81.3	63.9	64.1	63.6	60.8	61.3	57.7
7:P79739	55.0	81.2	80.6		63.9	64.8	63.6	60.8	62.9	57.3
10:Cyp26b1	55.0	62.4	63.2	63.8		98.2	88.2	71.5	71.9	70.2
13:G3V7X8	55.2	63.0	63.4	64.7	98.2		87.9	72.2	73.2	70.0
15:Q6EIG3	55.0	62.1	62.8	63.3	88.0	87.8		71.1	70.6	68.1
18:Cyp26c1	53.8	62.1	62.6	63.1	74.4	75.1	74.1		92.4	69.4
21:D4AAL3	54.5	62.8	62.6	64.7	74.2	75.5	73.0	91.6		70.2
23:A1L1M2	54.5	62.4	63.0	63.1	77.5	77.3	75.4	73.7	75.2	

Figure 19. Sequence identity matrix among CYP26s and Cyp120a1.

Analysing CYP26 models on the basis of the isoforms global alignment with the template, paying particular attention to the binding site, it was possible to identify some amino acids involved in binding to RA, and in particular Arg95 and Trp117, that are conserved across the three isoforms in each species. In particular, Arg95 binds with specific H-bonds to RA COOH-group, whereas Trp117 interacts with RA C18, displacing the ring to a position incorrect for metabolism (Figure 20). This problem of RA ring orientation can already be identified in the co-crystallized RA of the template used for homology modelling and will be considered in the analysis of docking poses.

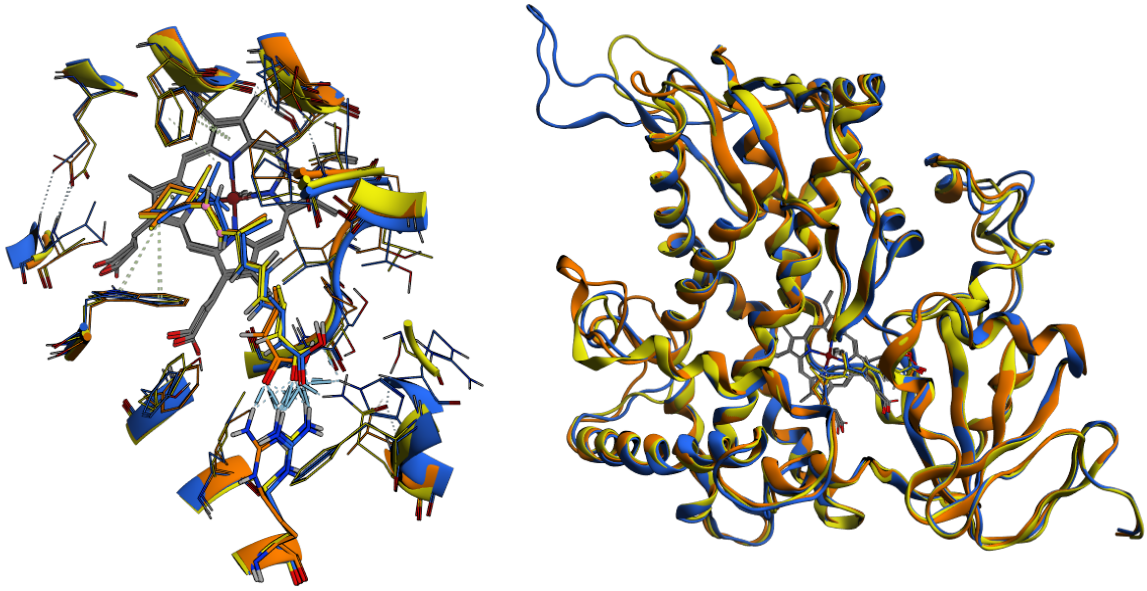

Figure 20. (left) Superimposition of hCYP26s binding sites. Some pivotal amino-acids are highlighted as bold side chains, as for RA and heme. (right) Superimposition of hCYP26s secondary structures. Colour code: yellow - hCYP26A1, orange – hCYP26B1, blue – hCYP26C1. heme is depicted in grey for the three isoforms.

On the other hand, in the Ramachandran plot of the nine models, only one outlier was found for hCYP26A1 and hCYP26B1, and two outliers for hCYP26C1; two outliers were found for each rCYP26 isoenzyme; two outliers were found for zCYP26 and three outliers for zCYP26B1 and zCYP26C1. All outliers are located in amino acids in the loops that do not insist on the binding site. Therefore, it can be stated that the obtained models of the CYP26s have good quality and can be used for docking calculations.
In order to investigate the effect of the CI in the development toxicology field, we tested all the CI compounds on CYP26 isoenzymes of human, rat and zebrafish. For these three species, we found that, using as cut-off the binding free energy value of -6.5 kcal/mol, approx. 50% of chemicals bind all isoenzymes. In this scenario, we used a cut-off not calibrated for the application on CYP26s, but derived from NR (toxicological cut-off) in order to build a common assessment based on a consensus strategy.
On the other hand, using as cut-off the RA binding free energy values (biochemical cut-off), we obtain that only approx. 20% of chemical are prioritized for each CYP26 isoenzyme. Table 7 reports the number of chemicals for each investigated CYP26.

	CYP26 isoenzyme	Cut-off -6.5 kcal/mol	Cut-off GG of RA
Human	CYP26A1	631	230
	CYP26B1	590	176
	CYP26C1	551	183
Rat	CYP26A1	642	226
	CYP26B1	604	205
	CYP26C1	641	188
Zebrafish	CYP26A1	658	212
	CYP26B1	629	191
	CYP26C1	613	192

Table 7. Number of prioritized chemicals with two different cut-off values (toxicological and biochemical) for each CYP26 isoenzyme.

Moreover, considering only the chemicals that bind the three CYP26 isoenzymes for each species, the percentage is reduced to an approx. 40%, using as cut-off -6.5 kcal/mol, and to 10%, using as cut-off, the RA binding free energy as reported in Table 8.

	Cut-off: -6.5 kcal/mol	Cut-off: ΔG of RA
Human	471	125
Rat	494	133
Zebrafish	515	113

Table 8**.** Number of prioritized chemicals with bind free energy lower than the two different cut-off values (toxicological and biochemical) for each specie.

Finally, among the chemicals that bind the three CYP26 isoenzymes of the three species, only 75 chemicals are common binders for all the CYP26 considered.

Discussion/Conclusions

According to our results, 75 chemicals, common binders for all the three CYP26 isoenzymes for human, rat and zebrafish simultaneously, were selected. Top scoring azoles of the training set of the previous part were also found in this selection. All the prioritized chemicals were further studied both *in vitro* and *in vivo* by EuroMix partners, and the results of these studies are published in EuroMix Deliverables on EuroMix web page (https://www.euromixproject.eu/).

Part III – Pharmaco-dynamics

Introduction

Retinoic acid feedback is a mechanism through which RA is able to control its own levels by eliciting up-regulation of CYP26A1 gene – which harbours two synergistic RAREs within its promoter (Loudig *et al*., 2000) – in a negative autoregulatory feedback. Several experiments demonstrated this control mechanism conserved across different model species (e.g. mouse, zebrafish and chick), to occur both *in vitro* and *in vivo* (Abu-Abed *et al*., 1998; Reijntjes *et al*., 2005; Dobbs-McAuliffe, Zhao, and Linney, 2004; White *et al*., 2007), showing an increase in CYP26A1 levels upon treatment with an excess of RA.
Moreover, up-regulation of CYP26A1 does not involve only tissues already expressing CYP26A1, but also tissues where it is not normally present (Pennimpede *et al*., 2010). Therefore, under normal developmental circumstances, it is likely that this feedback control mechanism provides embryos a defense against an excess of maternal retinoids, which may arise physiologically – e.g. of dietary origin.
Interestingly, Rydeen *et al*. (2015) demonstrated that RA self-induced feedback might cause, paradoxically, a depletion of RA. In fact, after exposure to teratogenic doses of RA, an excessive feedback might cause a hyper-stimulation of CYP26A1 expression, and a consequent extremely rapid degradation of RA, resulting in an unbuffered RA loss., As stated by the authors, this might explain why some retinoids-related abnormalities arise both in VAD and CYP26A1-/- embryos. i.e. the phenotype of embryos that experience an excess of RA sometimes resembles the phenotype of RA-deprived embryos.
As reported in Di Renzo *et al*, dose-related teratogenic effects were detected in rat embryos exposed to the different chemicals, e.g. azoles. The specific target for all tested azoles was the branchial apparatus in newborn rats, which was also affected by RA exposure.
The entire ordinary differential equation system is described in Chapter 4, while in the following sections some components of the system will be treated in order to explain their dynamics calibration. In fact, the calibration of the PD model is a dynamic process that provides us step by step information for each of the chemicals parameters, useful to predict mixtures.
All the data are extracted from Battistoni *et al*. (2019) and reported in Chapter 4. *In vitro*/*ex vivo* experimental information can be found in the same source. All the experiments were conducted in presence of 17 mM ethanol, which is demonstrated to be a no effect dose for rat embryo craniofacial malformations. ODE system is re-formalized *ex novo*, in order to improve some mathematical- and biochemical-related issues, inserting the affinity for each chemical.

Results – Model calibration (Single chemical)

Retinoic acid – logit calibration

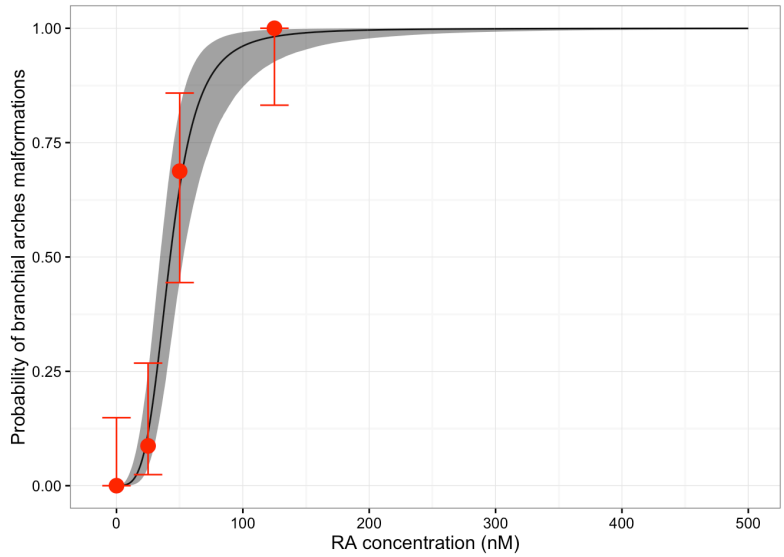

Figure 21: Retinoic acid concentration-response curve.

With the aim to extrapolate the logit parameters, a first run of the PD model was performed setting all the azoles concentration to zero. With this strategy, only retinoic acid is active in the system and data were fitted to extrapolate q_0 and q_1 logit parameter. In fact, these two parameters manage the logit, formalized as follows:

$$probability = \frac{RA^{q_1}}{(RA^{q_1} + q_0^{q_1})}$$

The ODE system, in this chase, can be simplified as follows:

$$\frac{dt}{dADH} = k_{syn_{ADH}} - k_{deg_{ADH}} * ADH + k_{trs_{ADH}} * ETH;$$

$$\frac{dt}{dRA} = k_{trs_{RA}} * ADH * \frac{RO}{(k_{i_{RO}} + RO) * 0.5} - k_{deg_{RA}} * RA - CYP26 * k_{m_{RA}} * RA;$$

$$\frac{dt}{CYP26_{mRNA}} = k_{trs_{CYP26}} + v_{max} * \frac{RA^2}{k^2_{act_{CYP26}} + RA^2} * \frac{FGF^2}{k^2_{inh_{CYP26}} + FGF^2} - k_{deg_{CYP26_{mRNA}}} * CYP26_{mRNA};$$

$$\frac{dt}{dCYP26} = k_{trd_{CYP26}} * CYP26_{mRNA} - k_{deg_{CYP26}} * CYP26;$$

$$\frac{dt}{dFGF} = k_{syn_{FGF}} * 0.5 - k_{deg_{FGF}} * FGF;$$

As first result, we obtained that q0 and q1 shall be set to 41.75 and 4.74, respectively. Both the Monte Carlo Markow Chains converged, strengthening our extrapolation.
With this setting, the logit model, in association with the PD model, is quite good in data representation. In Figure 21 all the *in vitro* data lay on the RA curve (black), while the 95% confidence region (grey) fits with data uncertainty. In this perspective, the logit function and the PD model, with "zero" settings, are descriptive of the *in vitro/ex vivo* data, representative of the malformation percentage at increasing RA concentration. Moreover, the value of RA_{base} was set to 26 nM, because RA exposure is endogenous here and RA baseline value needs to be subtracted in the logit function,

as reported in Battistoni *et al*. (2019). On the other hand, the sample size of the biological data implicates the high uncertainty in the data themselves, increasing the variability of the model, especially for the mixture prediction.

Single azoles fitting step

Three different azoles were considered during the growing step of the PD model: flusilazole (FL), triadimefon (TR) and cyproconzole (CY).

In order to extrapolate the kinetic constant of each azole, the azole-dependent term in the ODE system was switched-on, as follows:

$$\frac{dt}{dRA} = k_{trs_{RA}} * ADH * \frac{RO}{(k_{i_{RO}} + RO) * 0.5} - k_{deg_{RA}} * RA - CYP26 * (k_{m_{RA}} * RA - k_{m_X} * \frac{X}{K_{i_X} + X} * \frac{K_{i_{RA}+RA}}{RA} * X)$$

where "X" term was replaced with the azole concentration for each specific azole in the Hill term.

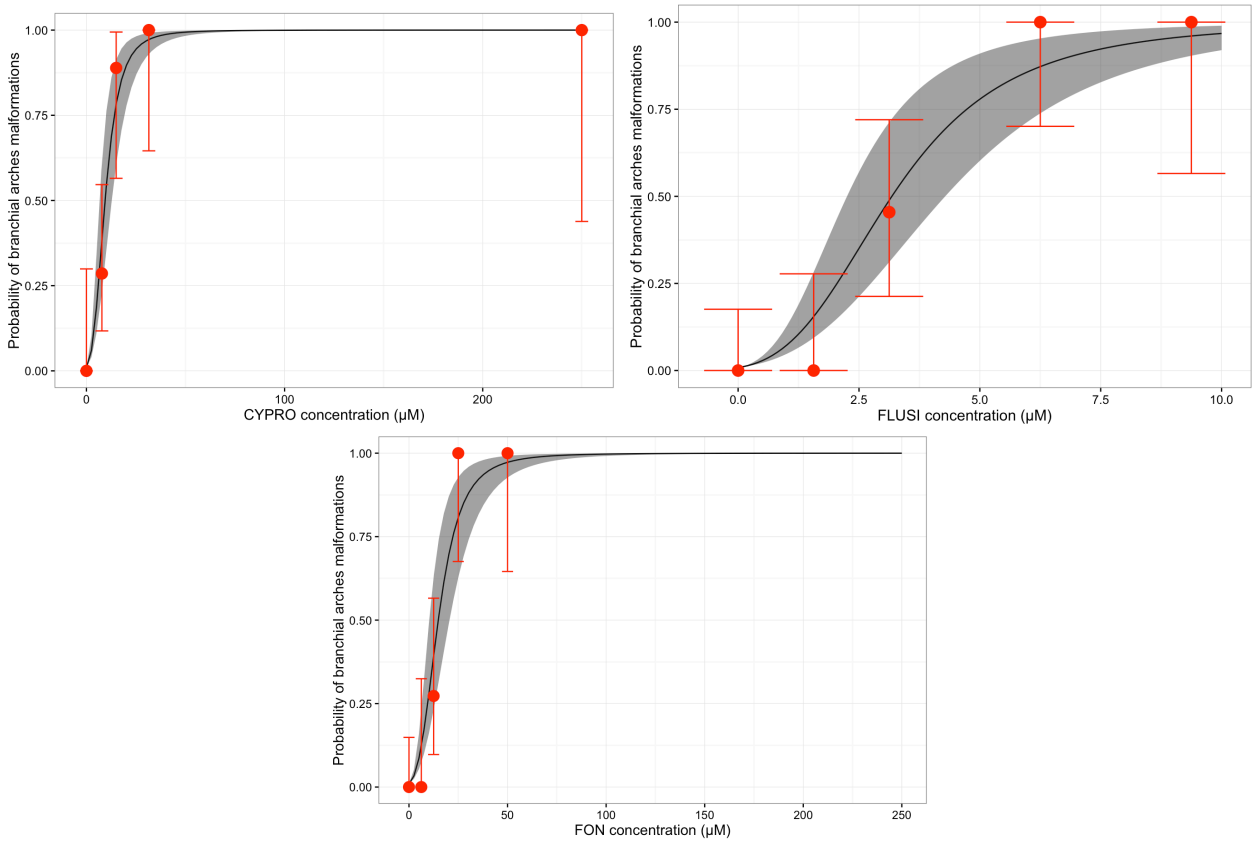

Figure 22: Cyproconazole (top- left), Flusilazole (top-right) and Triadimefon (bottom) concentration-response curve

The cyproconazole concentration-response curve (Figure 22), representative of the concentration and malformations probability relationship, well fit the *ex vivo* malformation data. On the other hand, the curves for FL and TR over-estimate the No Observed effect level (NOEL) and under-estimate the 100% effect dose. Both curves well fit the Low observed effect level (LOEL) since LOEL data

belongs to the black curves. In spite of this behaviour, FL and TR curves and data agree if also confidence intervals are considered.
All the MCMC simulations converged during the fitting steps, obtaining posterior predictions that are summarized in Table 9.

Parameter	Value [1/s]
Km_CY	0.0245
Km_FL	0.0019
Km_TR	0.0155

Table 9: Posterior prediction of azole-specific parameters.

The inhibition constants (Ki) of the three azoles were computed from the binding free energies in Part I of the present Chapter, using the following equation:

$$K_i = e^{\left(\frac{\Delta G}{RT}\right)}$$

where R is the gas constant and T is the temperature set at 20 °C.

Globally, the ODE system description is quite good with respect to malformation data. Probability malformation curve of each azole is included into the data variability, that is high due to the low number of biological embryos tested for each concentration of each azole.

Results – Model predictions (Mixtures)

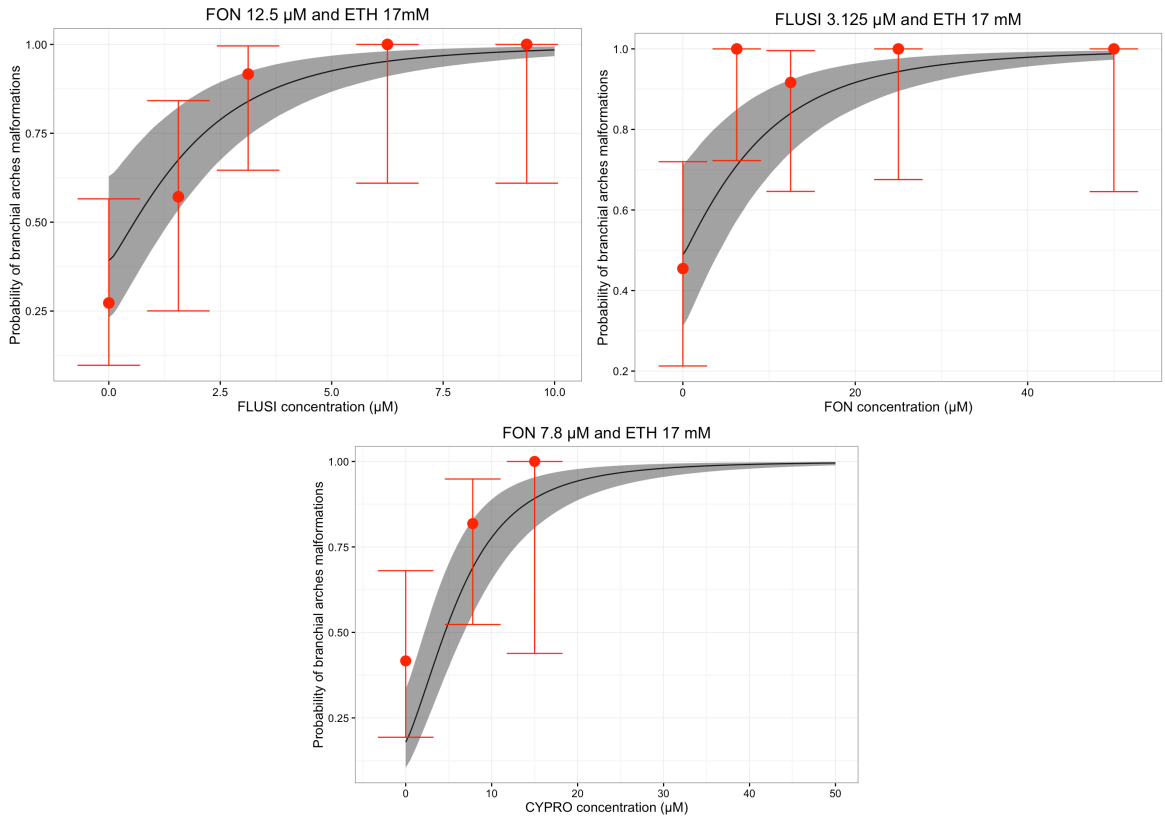

Figure 23: Flusilazole (top-left), Triadimefon (top-right) and Cyproconazole (bottom) concentration-response curve.

Computing by model predictions the effects of mixtures, we obtained the curves reported in Figure 23. Three different binary mixtures of azoles were tested in Battistoni *et al* (2019) and used in the present model:

- flusilazole at different concentration with triadimefon at 12.5 μM;
- triadimefon at different concentration with flusilazole at 3.125 μM;
- cyproconazole at different concentration with triadimefon at 7.8 μM.

Data (in red) were superposed to the predicted curves in order to check the reliability of the model. All the parameters extrapolated from the previous step were fixed in the ODE system and in the logit function.

As shown in Figures 23, model prediction curves, with their respective confidence intervals, are comparable with experimental data and their uncertainty. In detail, Figure 23 presents the same behaviour of the model for single azole, during the training step, with the model that overestimate the data at low flusilazole concentration and that underestimate the data at 100% effects. The data in Figure 23 (bottom) are always underestimated by the model prediction, while in Figure 23 (top-right) we obtained a peculiar behaviour of the data themselves. In fact, the second experimental point (triadimefon at 6.25 μM and flusilazole at 3.125 μM) reaches 100% malformation effect, while the third point (triadimefon at 12.5 μM and flusilazole at 3.125 μM) reaches only 92% of total observed malformations. In this case, the model is unable to reproduce the experimental behaviour, but it is able to reproduce the other data points with a good approximation.

In order to evaluate the effect of 17 mM ethanol on the PD model, we also run the same ODE system, setting to zero the ethanol concentration. As shown in Figure 24, in which the direct comparison between curves are reported (green, ethanol = 0 mM; blue, ethanol = 17 mM), ethanol effect could be preponderant near NOEL and at 100% azole effect dose, acting on ADH equation.

In particular, for all the three tested azoles, 17 mM ethanol effects at low azole concentration seem to affect the model by increasing the ADH transcription and consequently the retinol conversion to retinoic acid eventually leading to an overestimation of NOEL. In order to investigate these effects, we believe that it is necessary to perform some *in vitro* experiment using ethanol as testing chemical. With this aim, the weight of ADH equation and also the effect of mixtures of ethanol and azoles can be modelled and the biochemical pathway clarified.

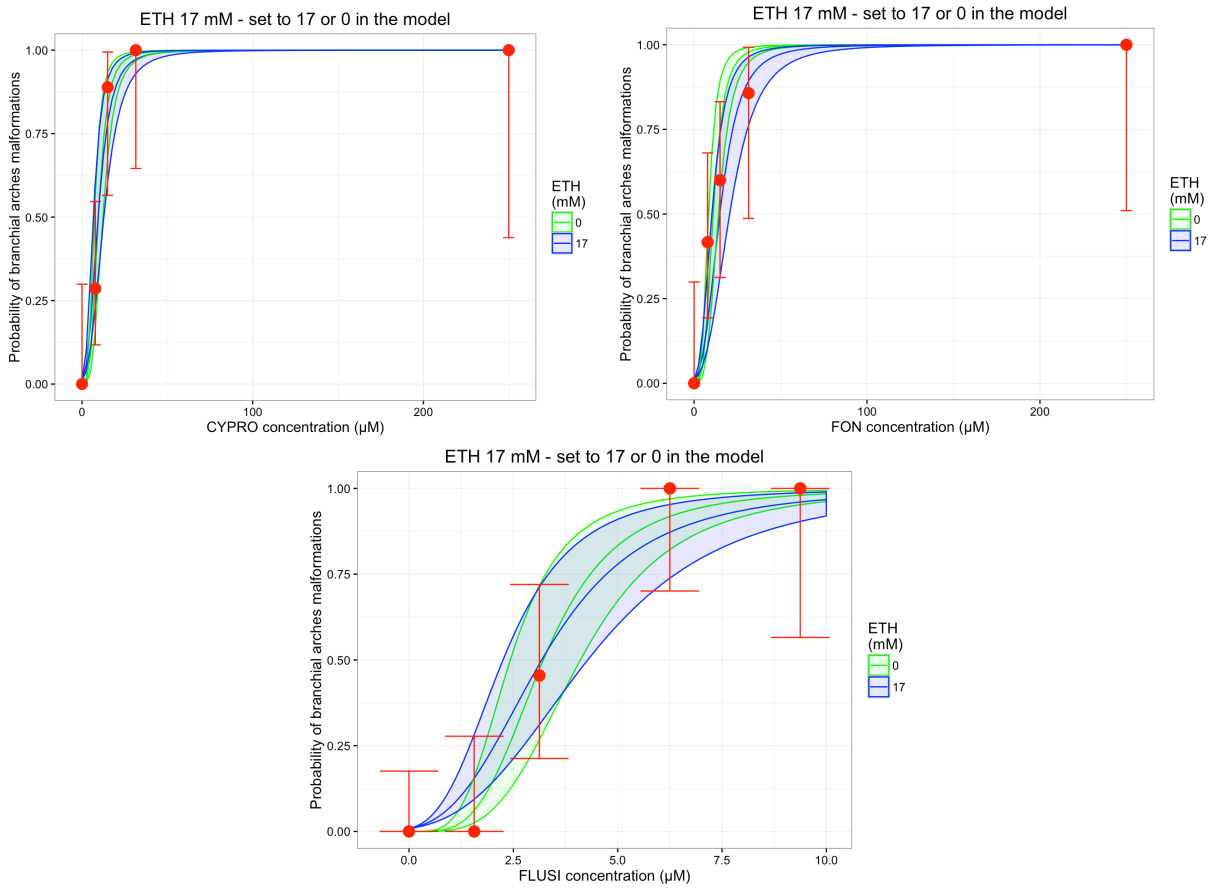

Figure 24: Cyproconazole (top-left), Triadimefon (top-right) and Flusilazole (bottom) concentration-response scurve.

Discussion/Conclusions

As in Battistoni *et al*, we developed a set of differential equations to describe the occurrences of cranio-facial malformations in rat embryos, considering not only the RA/azoles kinetic but also inserting biochemical information about affinity for CYP26.
According to data, our model confirms that RA is a very important morphogen, and its perturbation in developmental stage of embryos can increase the probability that foetal malformations occur. This model is also in agreement with Goldbeter *et al*., despite the greater degree of complexity of our equations.
Logit function is quite good to represent data, while the biochemical interaction among chemicals in the RA equation, described by Hill terms, is a likely approximation of cooperative interactions of chemicals which have common CYP26-mediated pathways.
Our model has two limitations: the first is that it is not applicable to describe the whole RA concentrations asa function of time in the whole embryo hindbrain, the second is that more data could strengthen the model, especially correcting some incongruence in mixtures.
In fact, with respect to spatial representation of RA concentration with time, different rombomers express different CYP26 isoenzymes at different developmental stages. In our model, we approximated all isoenzymes to CYP26A1, which is the only one induced by RA concentration, and we assumed embryo as a point in space.
Our model predicts the azoles dose-addition effect, and, after a training, can be applied also to other chemical mixtures which have the same AOP. Since the retinoic acid pathway is conserved among different vertebrate species, our model can be easily extended to other species, using the structure-based approach to compute the binding energies of the chemicals to species-specific CYP26 enzymes.

Globally, pharmaco-dynamics is a powerful tool to model this kind of systems, from biochemical pathways involving enzyme kinetics to adverse effects. Furthermore, biological interactions modelled through this model may be interpreted qualitatively to explore the critical nodes that regulate certain physiological or pathological phenomena, or they may be trained on experimental dataset to output quantitative results, usually with an order of magnitude accuracy. In either scenario, if correctly built, pharmaco-dynamic models overcome experimental cost, time and physical limitations by allowing a full exploration and manipulation of the system parameters and variables.
In the present Part, we have successfully integrated structural bioinformatics and systems biology simulations to deliver a working model describing RA dynamics during hindbrain development.

Part V – Physiologically based pharmaco-kinetics model

Introduction

Zhu *et al*. (2007) studied the stereoselective degradation kinetics of a well-defined racemic mixture of tebuconazole in rabbits. They presented concentration data in plasma, brain, adipose tissue, heart, kidney, liver, lung, muscle and spleen. Andreu-Sánchez *et al*. (2011) studied acute toxicity and bioconcentration of tebuconazole in zebra fish and published concentration data both in basin water and in total zebra fish body.
These last authors presented a classical pharmacokinetic model for tebuconazole total body burden in zebra fish, taken up through the gills from basin water, which is not really scalable to humans. There seems to be no model for tebuconazole in mammals. There is a physiologically based pharmacokinetic (PBPK-) model for triadimefon and its metabolite triadimenol in rats and humans (Crowell *et al*. (2011)). However, the data for triadimefon and triadimenol are from rats only and the kinetics shown by the data in plasma, liver, kidney, brain and fat and modelled kinetics do not really match. Also, it is not clear at all how to scale a model for triadimefon and triadimenol to tebuconazole. It was decided to develop a PBPK-model for tebuconazole in the rabbit, based on the experimental findings of Zhu *et al*. (2007).

Results

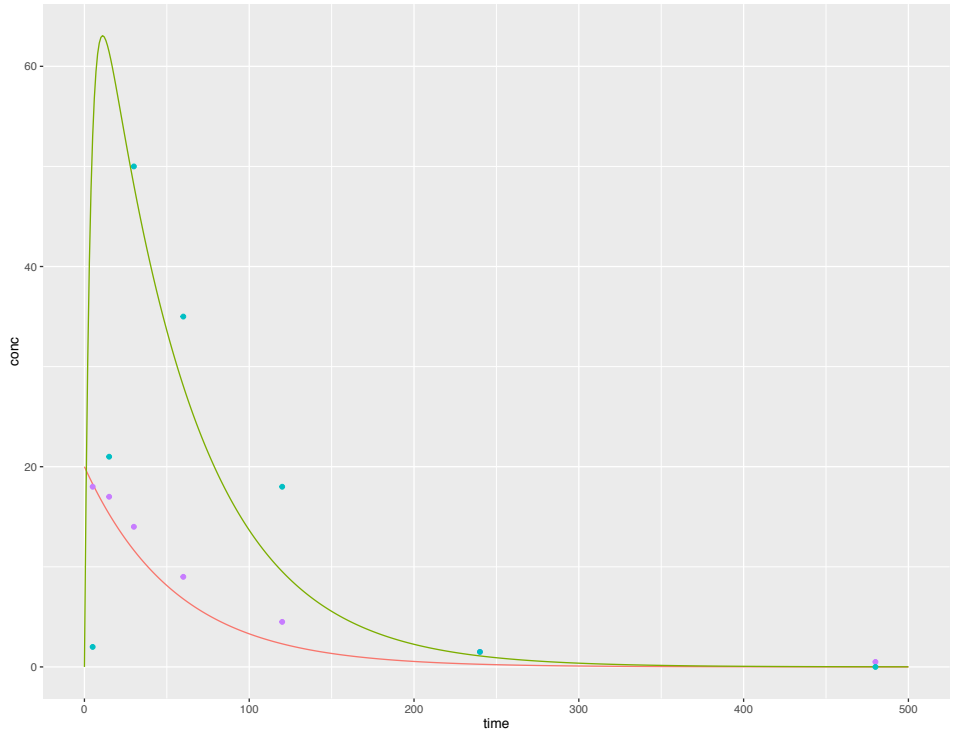

Figure 25: Amount of tebuconazole in brain expressed in µg/ml. Green lines represent the predicted concentrations in brain, while red line represents the plasma concentration, used as graphic scale. Points are the measured concentration (Zhu *et al*. 2007).

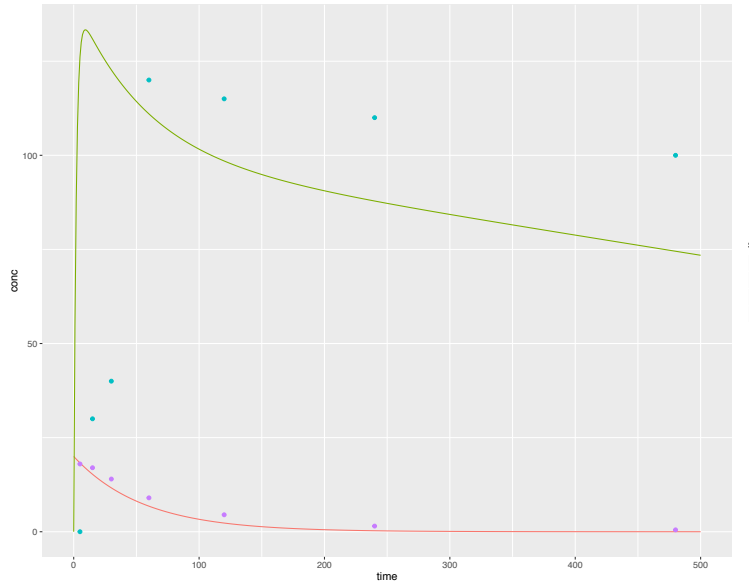

Figure 26: Amount of tebuconazole in adipose tissues expressed in µg/ml. Green lines represent the predicted concentrations in adipose tissues, while red line represents the plasma concentration, used as graphic scale. Points are the measured concentration (Zhu *et al*. 2007).

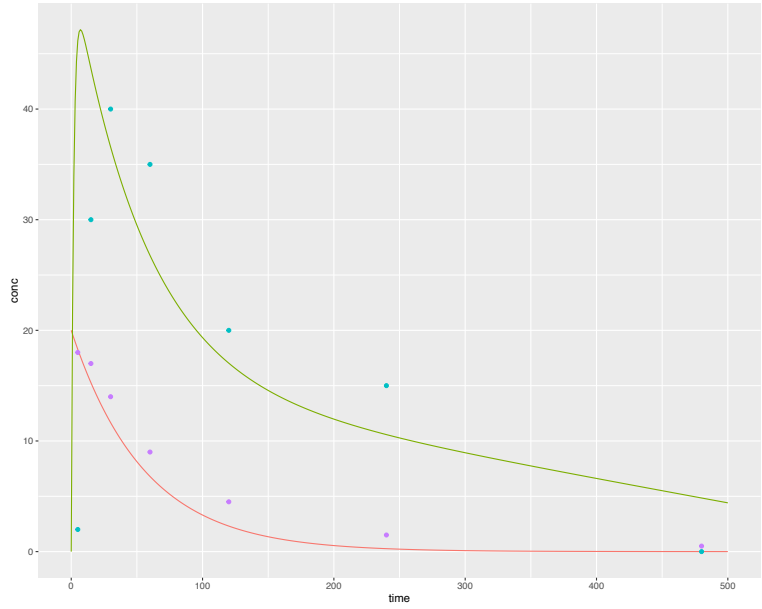

Figure 27: Amount of tebuconazole in heart expressed in µg/ml. Green lines represent the predicted concentrations in heart, while red line represents the plasma concentration, used as graphic scale. Points are the measured concentration (Zhu *et al*. 2007).

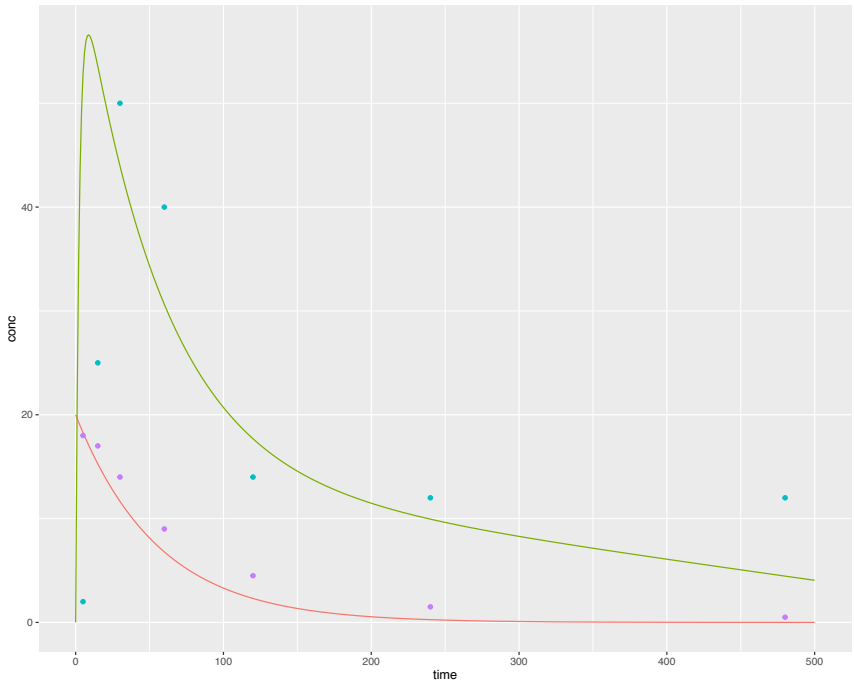

Figure 28: Amount of tebuconazole in kidney expressed in µg/ml. Green lines represent the predicted concentrations in kidney, while red line represents the plasma concentration, used as graphic scale. Points are the measured concentration (Zhu *et al*. 2007).

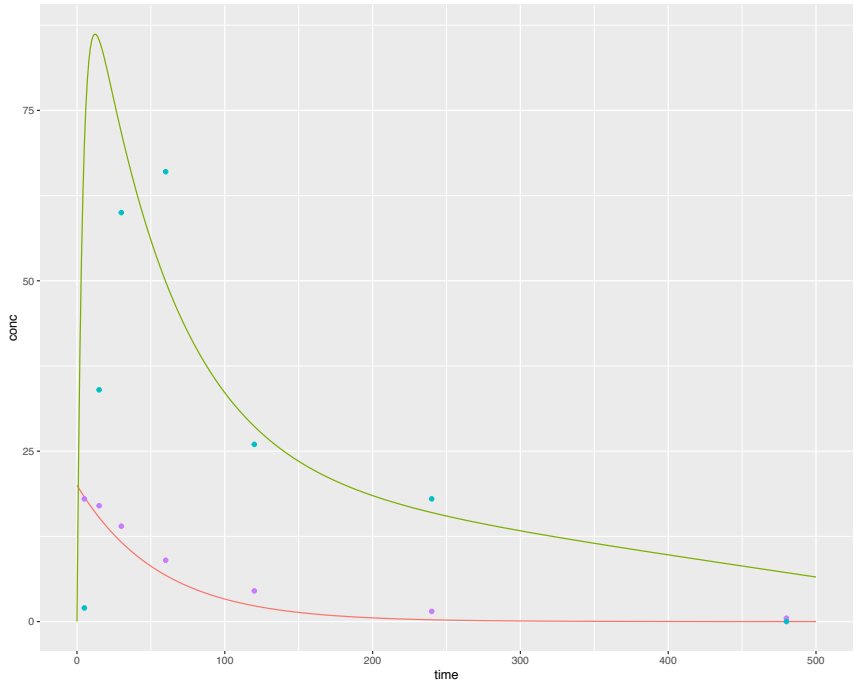

Figure 29: Amount of tebuconazole in liver expressed in µg/ml. Green lines represent the predicted concentrations in liver, while red line represents the plasma concentration, used as graphic scale. Points are the measured concentration (Zhu *et al*. 2007).

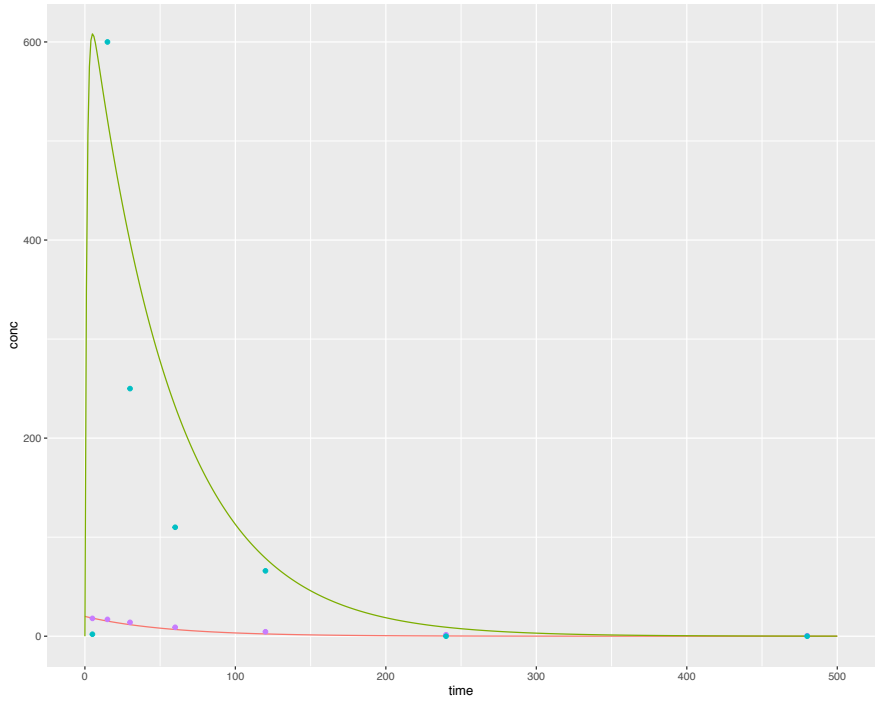

Figure 30: Amount of tebuconazole in lung expressed in µg/ml. Green lines represent the predicted concentrations in lung, while red line represents the plasma concentration, used as graphic scale. Points are the measured concentration (Zhu *et al*. 2007).

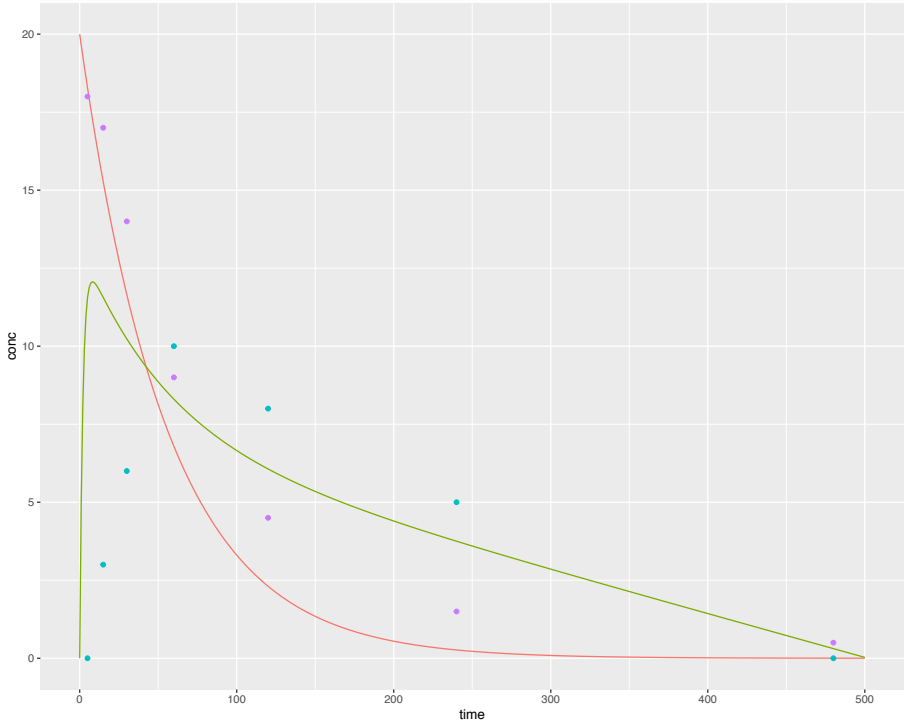

Figure 31: Amount of tebuconazole in muscles expressed in µg/ml. Green lines represent the predicted concentrations in muscles, while red line represents the plasma concentration, used as graphic scale. Points are the measured concentration (Zhu *et al*. 2007).

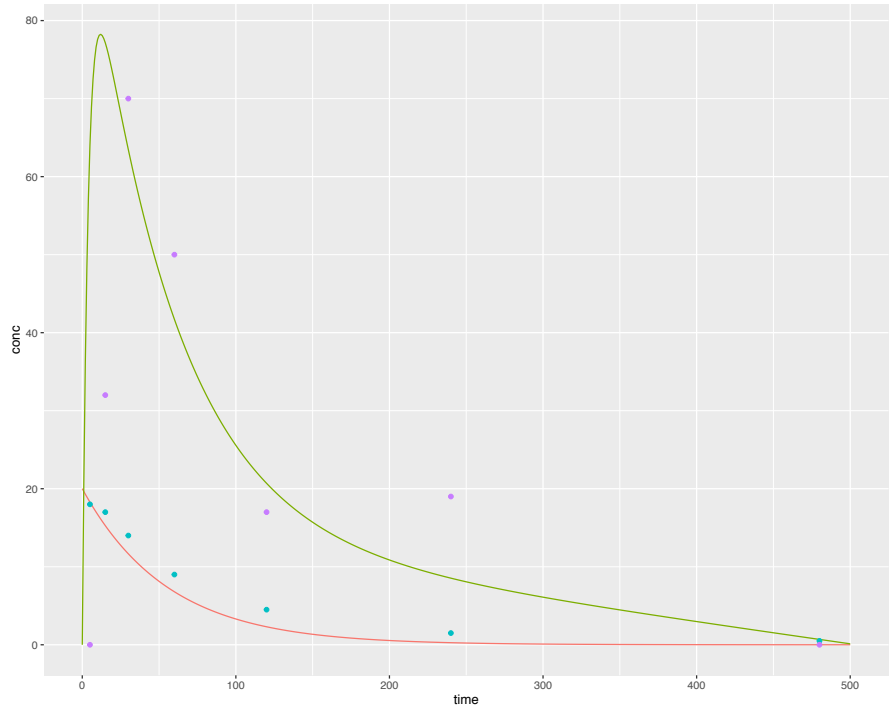

Figure 32: Amount of tebuconazole in spleen expressed in µg/ml. Green lines represent the predicted concentrations in spleen, while red line represents the plasma concentration, used as graphic scale. Points are the measured concentration (Zhu *et al*. 2007).

A full compartment fit was carried out using all the digitalized data simultaneously, in order to estimate the partition coefficient for each tissue and the liver clearance (Table 10)., The concentrations predicted through this approach (green lines) are also plotted versus the concentrations measured for tebuconazole in each of the tissues (violet points), using the plasma concentrations (red line and light blue points) as reference. (Figures 25-32).

Tissues	Partition coefficient
Fat:	12
Brain:	4.6
Heart:	4.3
Kidney:	4.1
Liver:	6.8
Lung:	0.2
Spleen:	5.0
Muscle:	9.0
Remaining tissues:	11

Table 10: Partition coefficients for selected tissues

The liver clearance value is 0.07 L/min. The percentage of regional blood flows with respect to the cardiac output (Table 11) was extrapolated from data on rats in Table 23 of Brown *et al*. (1997),

Tissues	Percentage
Adipose tissue	7.0%
Brain	2.0%
Heart	5.1%
Kidney	14.1%
Liver	2.1%
Spleen*	0.6%
Lung*	15.3%
Muscle	27.8%

Table 11: Percentage of the cardiac output for selected tissues

All the fitted curves seem to anticipate by approx. 1 hour the maximum concentration measured *in vivo*; for adipose tissue the fitted curved underestimates the accumulation effect. This outcome could be due to uncertainties in the value of the fitted parameters i.e. distribution kinetics, and Plasma::Tissues partition coefficient, or could be connected with the competition between (R)-tebuconazole and (S)-tebuconazole in physiological systems. This competition is not covered by our model, which considers the enantiomers as a single compound; however, from our molecular docking simulation it is clear that the two forms of tebuconazole have different binding energies on cytochromes and other enzymes. On the other hand, the modelled kinetics in plasma complies with experimental data.

The trends seen in the curves modelled for all the tissues reflect the *in vivo* data: a maximum is attained in the first hour followed by a slow decrease to a minimum, near zero, for all the tissues, except adipose tissue and kidney. Lung and brain reach a steady state in 250 minutes, while the other curves keep decreasing.

As a first application of the PBPK model on white Japanese male rabbits, we simulated the acute oral exposure to 1 mg tebuconazole per kg of body weight (Figure 33) in comparison with intra-venous bolus dosing of the same amount of the drug (Figure 34); in both figures the circulating concentration of tebuconazole is plotted with a blue line, the concentration in liver with a red line

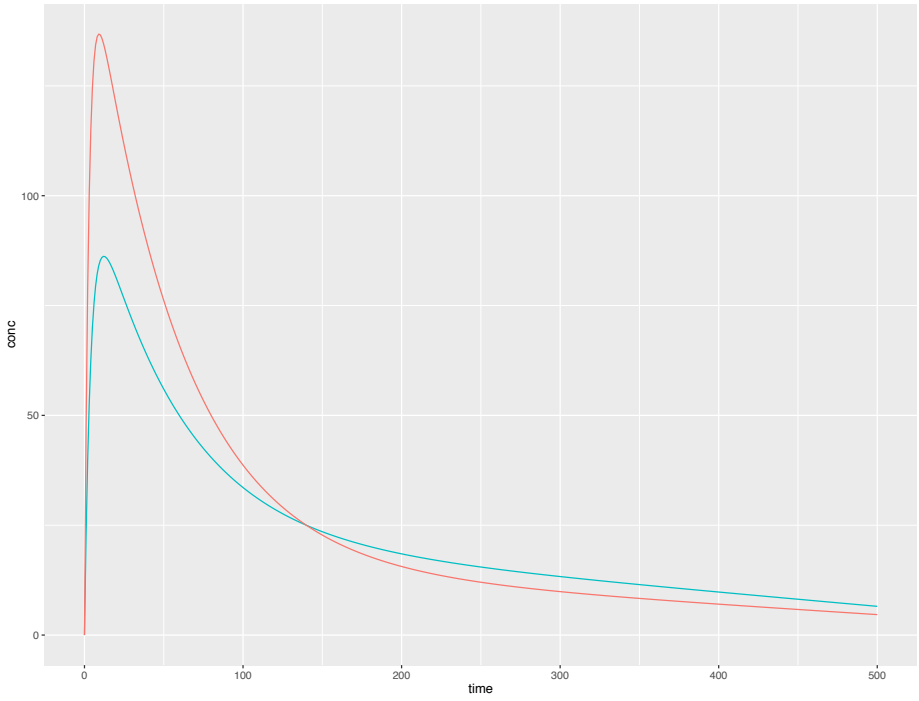

Figure 33: Plasma (blue line) and liver (red line) concentrations of tebuconazole after a acute oral exposure to 1 mg per kg of body weight.

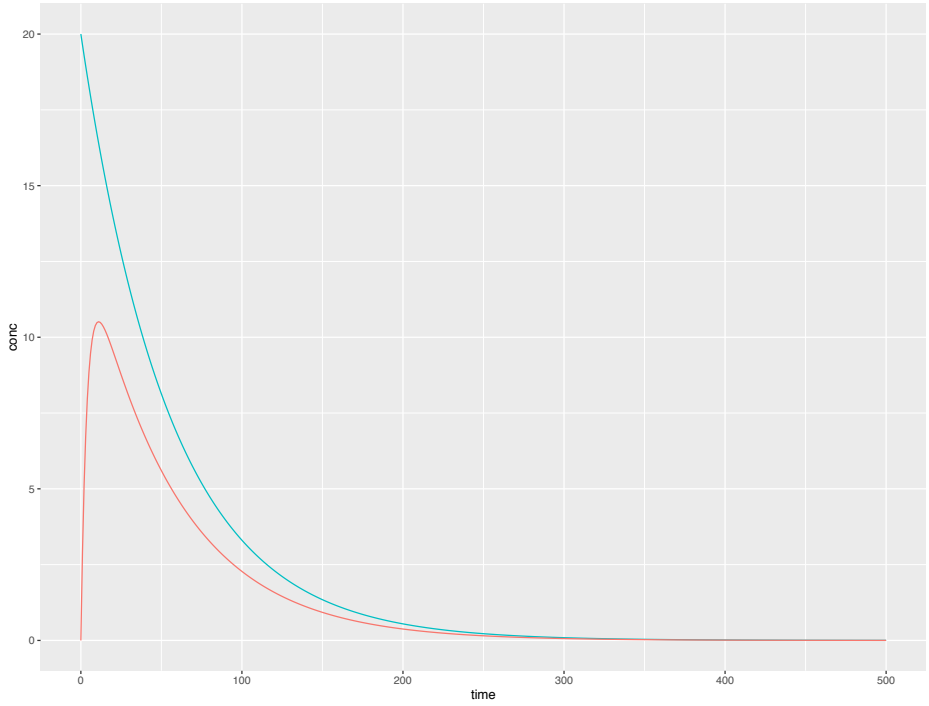

Figure 34: Plasma (blue line) and liver (red line) concentrations of tebuconazole after an intravenous injection of 1 mg per kg of body weight.

As expected, concentration in plasma is constantly higher after administration by intravenous than by oral route; in both cases the circulating concentration decreases after its peak with the same pendency. On the other hand, in liver, after oral intake drug concertation reaches higher values than after intravenous injection, and shows a slower elimination kinetics.
Considering the same oral doses of 1 mg tebuconazole per kg of body weight, we simulated a scenario in which tebuconazole is given to Japanese white rabbits every 2 hours, in order to evaluate the capability of the equations to predict the kinetics of the physiological model. We simulated the events during 8 hours span and report here the curves for brain (Figure 33) and liver (Figure 34).
In both tissues, the first peak is associated with the lowest maximum, while the remaining are (very) slowly increasing. No steady state is reached within 8 hours, whereas it is reached after approx. 12 hours when running a 24 hours simulation (data not shown).

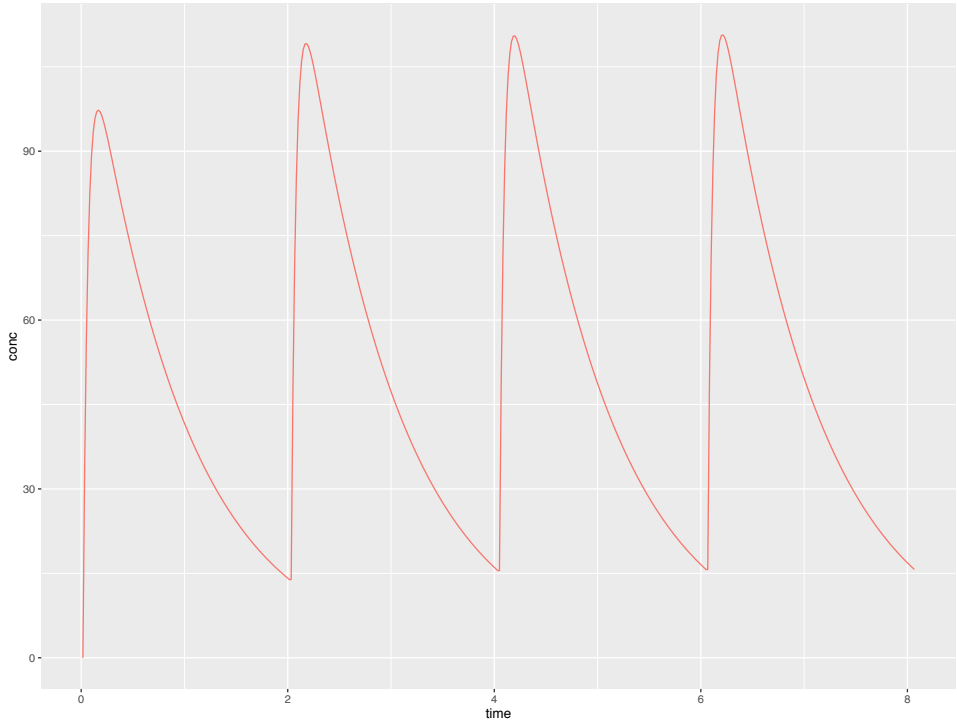

Figure 35: Tebuconazole kinetics in brain (rabbit).

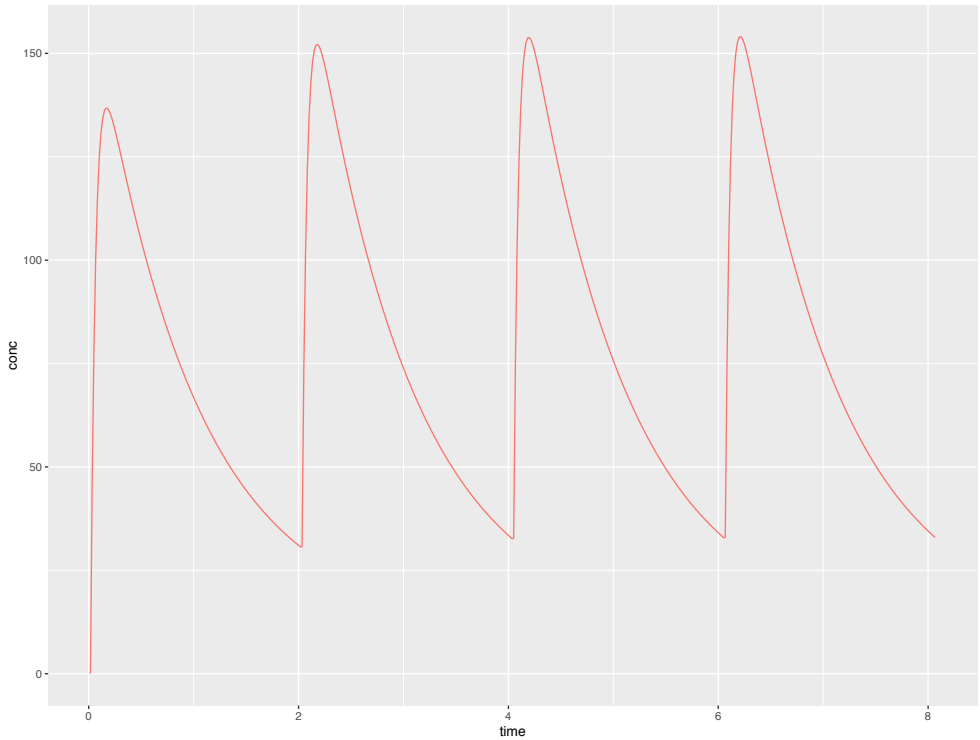

Figure 36: Tebuconazole kinetics in liver (rabbit).

On the basis of these results, we decided to extrapolate human parameters, building a human model and simulating the same kinetics at same doses. Calibrating the human model, we found that the elimination rate of tebuconazole is slower than in Japanese rabbits, so we extended the simulation to 4 days. Tebuconazole kinetics is plotted in Figure 35 for brain, in Figure 36 for liver and in Figure 41 for adipose tissue. Also in humans we reproduced the same behaviour as in rabbits, with the first pick in each tissue or in plasma reaching a lower concentration than the others.

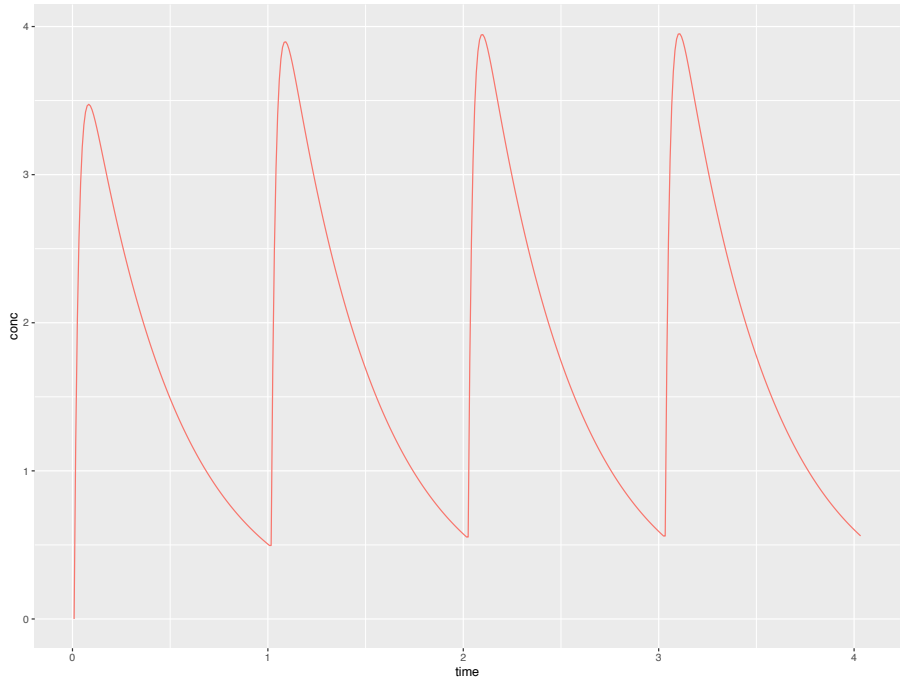

Figure 37: Tebuconazole kinetics in brain (human).

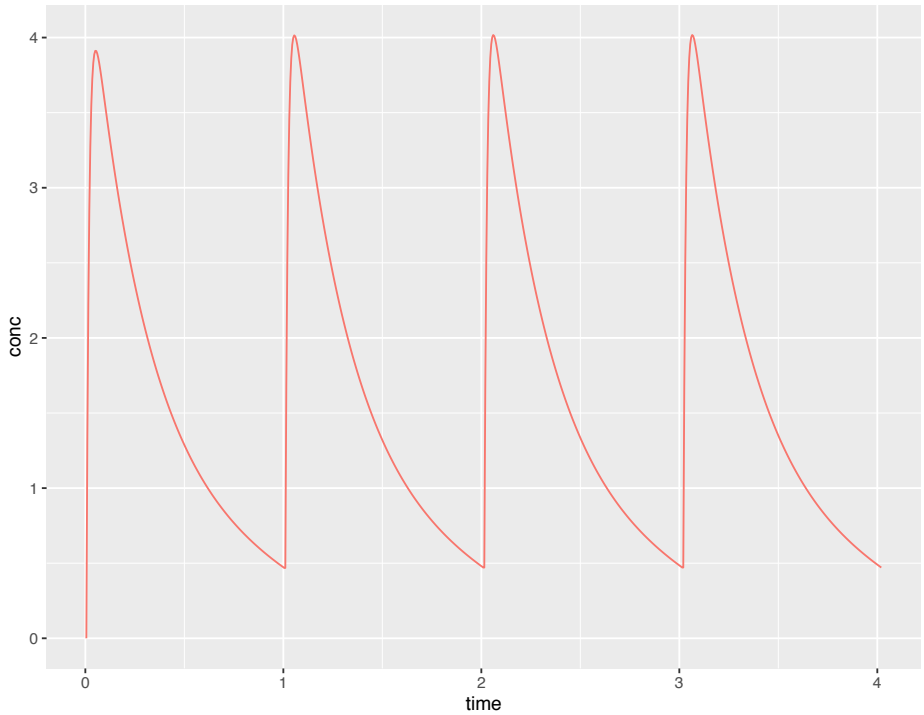

Figure 38: Tebuconazole kinetics in liver (human).

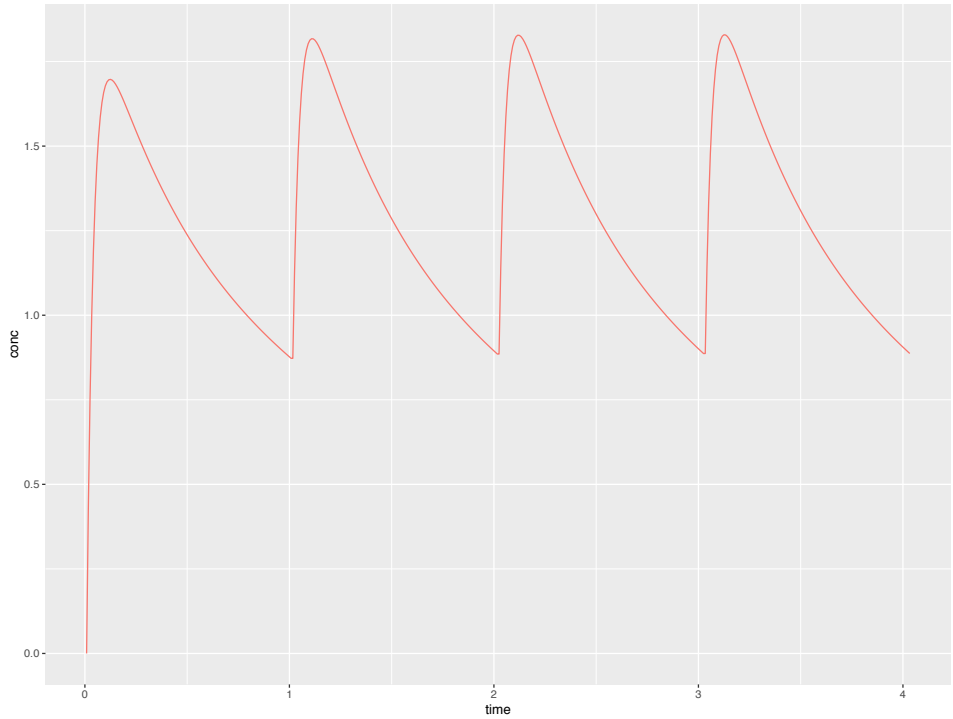

Figure 39. Tebuconazole kinetics in adipose tissue (rabbit).

Discussion/Conclusions

Here we present the tebuconazole PBPK model on both rabbit and human, starting from Japanese white male rabbit. All the data, extracted from Zhu *et al*., are based on a single rabbit per point and, due to this fact, are subjected to a high uncertainty. On the other hand, we merged the (R)- and (S)-enantiomers of tebuconazole into a single chemical. With this choice, we simplified the system, avoiding to model the (R)- and (S)-tebuconazole interaction or competition but likely introduced a source of uncertainty in our model. All of these limitations notwithstanding, the ODE system seems to reproduce the experimental data in rabbit, after a single intravenous injection of tebuconazole. Our extrapolation to the oral dose as well as our scenario for rabbit simulation need to be confirmed by *in vivo* experiments in order to refine the model to be eventually applied to humans.
Our model can be extended to other azoles/chemicals following the same kinetics. In particular, it can be applied to the above studied azoles to devise, from the *in vitro* data, the appropriate concentrations to be tested *in vivo* to promote (re)myelination in an animal model of multiple sclerosis. Other studies shall be performed to calibrate the extrapolation of human parameters from animal figures, while considering clinical data of accidental chemical assumption.
On the other hand, our model seems to be effective in describing the rabbit model; our extrapolation to humans, based on literature, can be assumed as a first step of a physiologically-based approach to study tebuconazole and its kinetics.

Part V – (Re)myelinating effect of azoles

Part V, which is not directly connected with the main theme of the present PhD thesis, has been added with the aim to show how to repurpose the same in silico methodology developed for the toxicology on another field, having the same molecular initiating event. The Part V research was founded by FISM trough a project granted during my second year of PhD, in which I contributed as participant both in the *in silico* part and in statistical analysis of the *in vitro* experiments. Part I of this chapter was used as preliminary results in the purposed project.

Introduction

Recently, an unforeseen activity on promoting (re)myelination in either *in vitro*, *ex vivo* and *in vivo* models of multiple sclerosis (MS) has been proposed for two drugs approved for clinical use in skin infections and disorders. In particular, miconazole showed a direct effect as (re)myelinating agent with no effect on the immune system.
Several other azoles are currently available for systemic use as antifungal agents, including triazoles (fluconazole, itraconazole, voriconazole, posaconazole, and isavuconazole) and an imidazole (ketoconazole).
Due to their long-standing use in clinic, their pharmacokinetics, safety and antimycotic activity are well characterized. However, nothing is known about the mechanism underlying the effects of miconazole on Oligodendrocyte Precursor Cells (OPC) and the potential pro-myelinating activity of other members of the azole family.
These observations provide the rationale for further investigation of the repurposing potential of these drugs, or structurally modified derivatives, for their ability to enhance remyelination in MS patients.
Antifungal azoles are potent teratogenic agents and concentration-related (125-500 μM) teratogenic effects have been also observed after *in vitro* exposure of rodent embryos: the abnormalities were specifically at the level of the branchial arches (the embryonic precursors of the facial elements) (Tiboni, 1993; Menegola *et al*., 2001)**.** Even if the adverse outcome pathway is not definitively demonstrated, it has been hypothesized that CYP26 inhibition could be at the basis of azole teratogenicity. Similarly to what described in patients treated for acute promyelocytic leukaemia (Vanier *et al*., 2003), the suggested mechanism accounting for teratogenicity is the enhancement of the endogenous levels of RA, mediated by the inhibition of specific embryonic CYP26 enzymes (Menegola, Broccia, Di Renzo, *et al*., 2006). This hypothesis, indicating that azole fungicides act through an indirect teratogenic mechanism mediated by an endogenous increase of RA content, is supported by: (1) the evidence that the observed abnormalities are quite similar to those evoked by RA exposure; (2) the abnormalities induced by the co-exposure to sub-teratogenic concentrations of fluconazole and RA, and (3) the evidence that the co-administration of a specific RA synthesis inhibitor (citral) reduces the effects of triazole-derivatives in *in vitro* developing embryos (Menegola *et al*., 2004; Di Renzo *et al*., 2007). A retinoic-like disruption of gene expression during branchial arch formation has also been demonstrated after exposure to some azole fungicides (Marotta & Tiboni, 2010; Di Renzo *et al*., 2011).
Interestingly, vitamin A, RXR agonists and retinoids have been proposed for the use in regenerative therapy in the CNS, including demyelinating disorders, and tested in experimental autoimmune encephalomyelitis (EAE) murine models of MS (Huang *et al*., 2011; Diab *et al*., 2004). Indeed, retinoids can stimulate oligodendrocyte differentiation and remyelination in the injured CNS through the positive regulator of endogenous OPC maturation RXR-gamma. Moreover, the RA receptor RXR-gamma is expressed after focal demyelination and in active MS lesions, suggesting that RXR-gamma is a physiological signal of injury in the acutely lesioned brain (Huang *et al*., 2011).

On this basis, we hypothesise that the mechanism underlying the enhanced myelination induced by miconazole may be linked to the inhibitory effect of azoles on the RA catabolic isoenzymes CYP26. The increase of cellular and tissue concentration of RA induced by azole antifungals thus represents a promising (re)myelinating strategy for antimycotic drugs to be repurposed for MS clinical indications.
This research was founded by Fondazione Italiana Sclerosi Multipla - FISM and *in vitro/ex vivo* experiments has been conducted in collaboration with dr. Parravicini and prof. Menegola's laboratory of Università degli Studi di Milano. This Part of the present Chapter follows the scientific report delivered to FISM in May 2018.

Results and discussion – Structure-based approach

Seven different azoles in clinical use for human pathologies (ketoconazole, isavuconazole voriconazole, posaconazole, fluconazole, itraconazole, miconazole) were selected with the aim of investigating their ability to induce the local increase of retinoic acid (RA) concentration, assumed to be responsible for the (re)myelinating effects observed in specific experimental models (Najm *et al*., 2015).
All the generated complexes (azole::CYP26s) were carefully inspected, to select only the ones with the azolic ring coordinating the CYP26 heme group, as reported in literature (Li *et al*., 2012).
Itraconazole, isavuconazole, and posaconazole were selected, on the basis of the computed binding free energies, for further *in vitro* testing.
Top-scoring poses from the docking procedure were refined by using the MOE "QuickPrep" procedure, aimed at relaxing the ligand within the CYP26 binding pocket and at refining the complex through a constrained forcefield EM. Then, the dissociation constant (Ki) was computed starting from affinity values (binding free energy, ΔG), according to the equation:

$\Delta G = RT \ln(K_i)$,

where R represents the gas constant and T the temperature (300 K).

Azoles on human CYP26s	Binding free energy [kcal/mol]	Affinity [kcal/mol]	Ki	CYP26 isoenzyme
Itraconazole	-11.8	-13.4	9.9	CYP26B1
Posaconazole	-11.1	-13.3	9.8	CYP26B1
Ketoconazole	-9.9	-12.3	9.1	CYP26B1
Isavuconazole	-9.3	-9.6	7.1	CYP26A1
Retinoic Acid	-8.3	-8.5	6.3	CYP26C1
Miconazole	-8.2	-8.7	6.4	CYP26A1
Voriconazole	-7.6	-13.4	9.9	CYP26B1
Fluconazole	-7.0	-7.6	5,6	CYP26A1

Table 12. Binding free energy and affinity values of selected azoles on human CYP26 isoenzymes

Azoles on rat CYP26s	Binding free energy [kcal/mol]	Affinity [kcal/mol]	Ki	CYP26 isoenzyme
Itraconazole	-11.2	-12.1	8.9	CYP26A1
Posaconazole	-9.7	-10.8	7.9	CYP26A1
Ketoconazole	-9.4	-13.7	10.1	CYP26A1

Isavuconazole	-8.5	-9.8	7.2	CYP26A1
Retinoic Acid	.8.3	-8.6	6.3	CYP26A1
Miconazole	-8.0	-8.6	6.3	CYP26A1
Voriconazole	-7.1	-8.4	6.2	CYP26C1
Fluconazole	-7.0	-7.1	5.2	CYP26C1

Table13. Binding free energy and affinity values of selected azoles on rat CYP26 isoenzymes.

In detail, as shown in Table 12 and Table 13, itraconazole and posaconazole were selected as the most promising compounds to be tested for their high affinity for the CYP26 family. Since they exhibited high affinity for both CYP26B1 and CYP26C1 isoenzymes, but not for CYP26A1, and no information is currently available on their differential expression in OPCs, isavuconazole, the top-scoring compound for hCYP26A1, was included in our analysis too. Moreover, the effect of fluconazole, which has the lowest affinity for the CYP26 family, was also evaluated.
Very interestingly, the affinity and Ki (pKi= 6.37) values obtained for miconazole are consistent with literature data (Najm *et al*., 2015). Globally, no differences in affinity for the investigated azoles was found between human and rat CYP26s, suggesting that rat OPC cultures are a suitable model for testing clinically used azoles.

Results and discussion – In vitro approach

OPC cultures
Figure 40 shows an enlargement of a typical myelin basic protein positive (MBP)+ cell while Figures 41 and 42 show typical fields for each azole treatment, in absence and in presence of citral.
Count results are shown in Figure 47. Liner mixed effect type III analysis of variance with Satterthwaite's method resulted in $p<0.001$ validating comparisons with "treatment contrast" (i.e. control vs everyone). Itraconazole increases significantly the level of oligodendrocyte precursors cells (OPC) differentiation compared to control (vehicle) while posaconazole decreases it significantly. A borderline ($p < 0.1$) increases in OPC differentiation level is registered for citral while the combination of citral and posaconazole results in a borderline decrease.

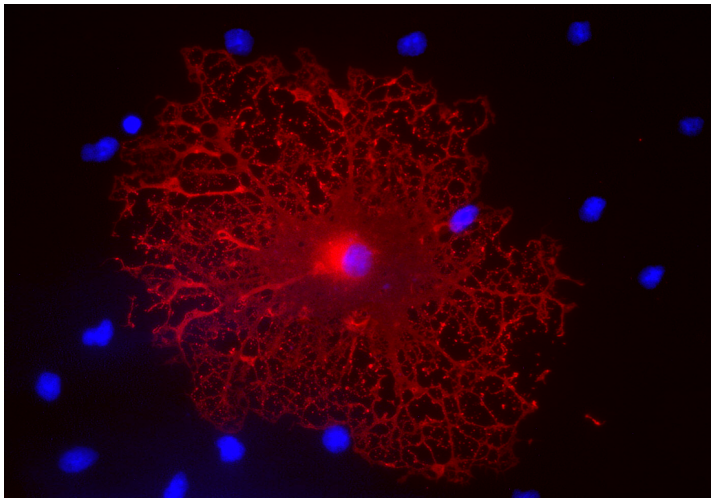

Figure 40. 40X magnification of one OPC expressing MBP (red)

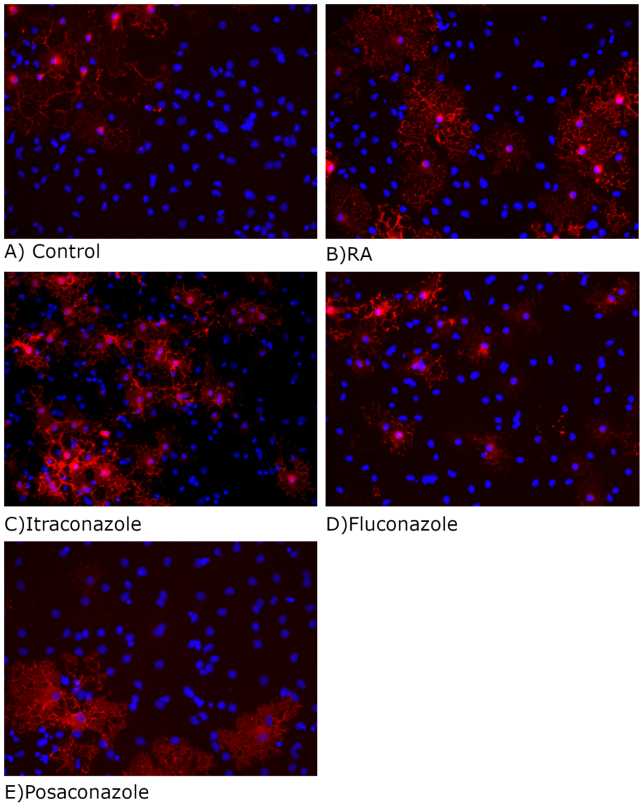

Figure 41. expression of MBP (red) in OPC cells treated with the reported condition. Nuclei are stained in blue.

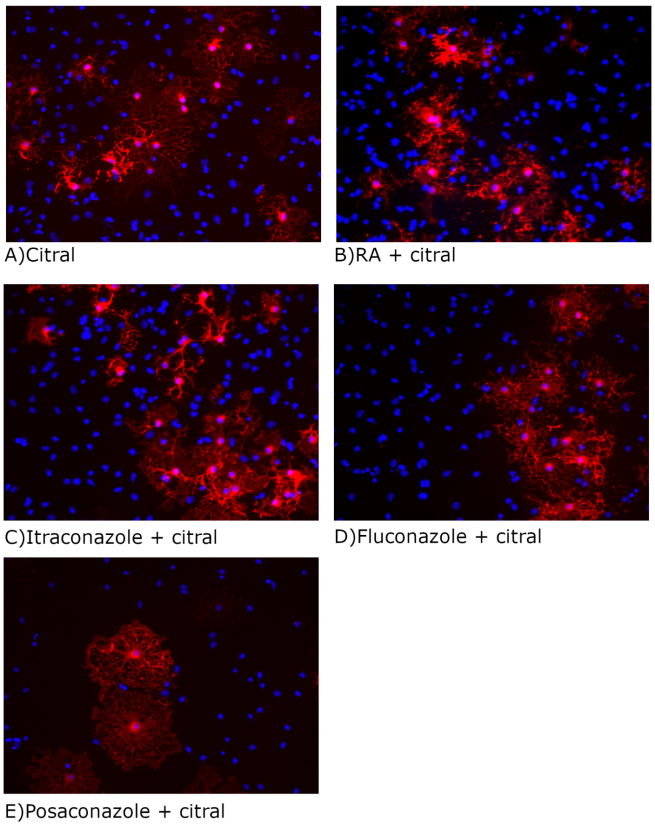

Figure 42. expression of MBP (red) in OPC cells treated with the reported condition. Nuclei are stained in blue

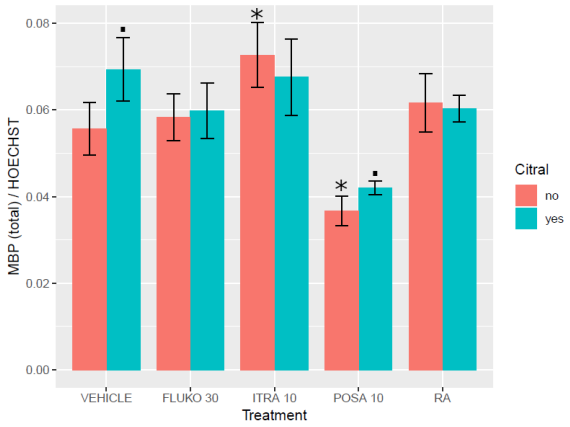

Figure 43. FLUCO: fluconazole; ITRA: itraconazole; POSA: posaconazole; RA: retinoic acid. Ratio of MBP / HOECHST for all experimental groups with or without Citral. Errorbars represent the standard error of the mean (* means $p < 0.05$ while · means $p < 0.1$).

DRG-OPC co-cultures

To determine whether CYP26 inhibitors can affect the myelination process, we performed a series of experiments using the OPC/DRG co-culture system. To this purpose, OPCs co-cultured with DRG were exposed to the following mixtures: retinoic acid (50 nM), retinoic acid (50 nM) + Citral (150 μM), Itraconazole (10 nM), Itraconazole + Citral, Fluconazole (30 nM), Fluconazole + Citral. After fixation, cells were immunostained for MBP to visualize myelinated axons and for Smi31 and Smi32 to visualize neurofilaments, we then measured the intensity of the fluorescent signal arising from the co-localisation of markers for neurofilaments and MBP.

Figure 44 shows representative samples of coverslips for each treatment as seen at confocal microscope (panels B-H) and myelination index results (in panel A). Liner mixed effect type III analysis of variance with Satterthwaite's method resulted in $p < 0.001$ validating comparisons with "treatment contrast" (i.e. control vs everyone). As in the case of OPC counts itraconazole shows the highest increase the level of myelination compared to control ($p < 0.001$). Also RA ($p < 0.01$), RA + citral ($p < 0.001$) and fluco ($p < 0.01$) show significant increases of myelination level.

OPC-DRG data show how the co-administration of citral reduces the effect induced by the azoles. This is in contrast with the evidence on mono-culture of OPC, suggesting a mayor role of DRGs in the regulation of RA levels and, consequently, of OPCs differentiation.

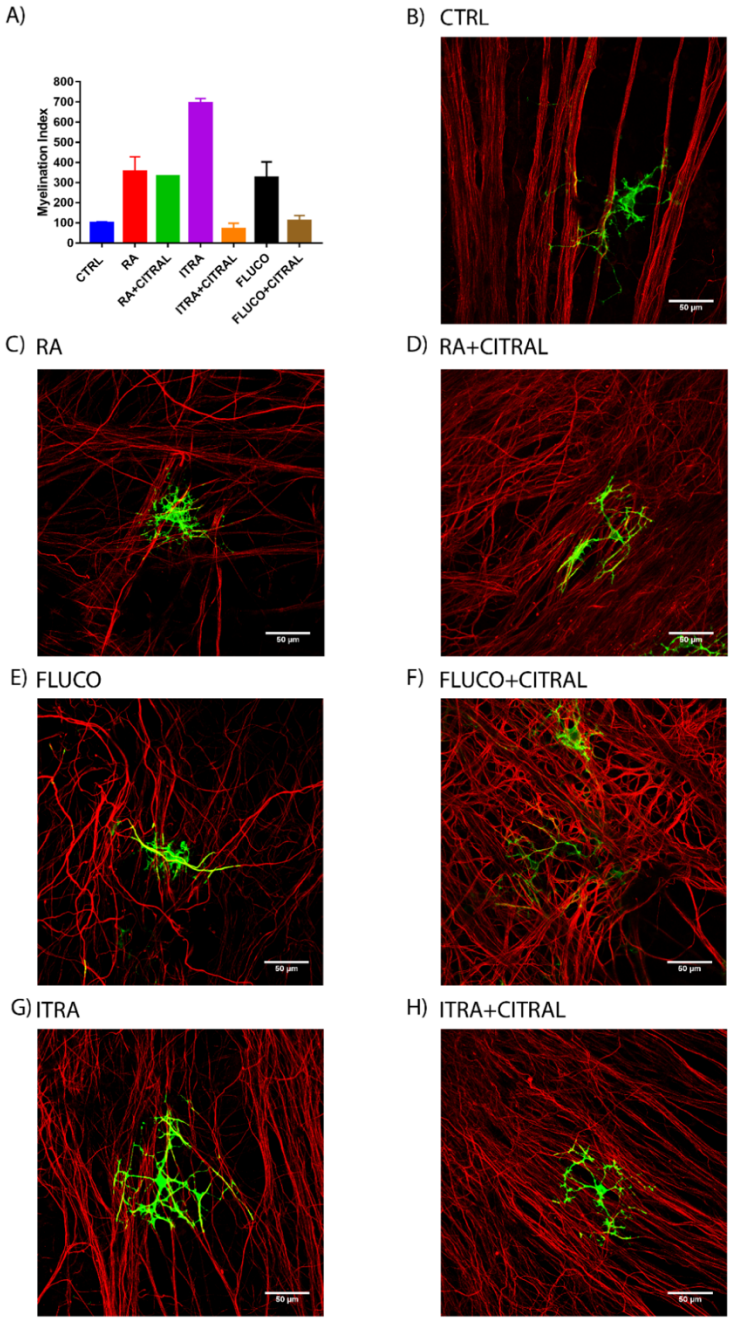

Figure 44. MBP: green; NF: red. A: myelination index (** $p < 0.01$, ***$p < 0.001$).
B-H representative samples of coverslips for each treatment as seen at confocal microscope.

Micromasses

Micromass test involves exposing undifferentiated rat embryo midbrain cells to test compounds and observing the subsequent effect on cell differentiation. In comparison to the other *in vitro* tests, the micromass test falls between the single cell system and organ cultures. Undifferentiated mesencephalic cells, in fact, are disaggregated before culture but are then put in culture at high density. Within these high-density cell colonies, cells that are destined to differentiate move together and form distinct foci (three-dimensional aggregation of cell bodies) interconnected by bundles (aggregation of neuronal processes, differentiated foci) which can be distinguished from foci without bundles (undifferentiated foci) (Flint, 1983; Flint & Orton, 1984; Girling & Flint, 1984).

Results confirmed 5HT inhibitory effects at 50-100 μM. Between the two test conazoles, fluconazole and itraconazole, the most promising molecule in our model was fluconazole. Fluconazole resulted, in fact, unable to affect foci formation and differentiation at any tested concentration and showed, similarly to miconazole, a positive action in foci formation. In order to test protective effects of fluconazole on 5HT effects, we co-exposed micromasses to mixtures of 5HT and fluconazole during the whole culture period (5HT 1-10-50 μM + fluconazole 50 μM). Results show that co-exposed groups were not different from the unexposed group (control, exposed to the DMSO solvent alone), suggesting a protective effect of fluconazole.

A second set of experiments were devoted to the evaluation of a fluconazole-related reparative effect. Cultures were exposed during the first day to 5HT 1-10-50-100 μM alone and during the remaining culture days to fluconazole 5-25-50 μM alone. Results show that fluconazole exposure after 5HT one-day exposure allowed micromasses to develop not differently from the unexposed group (control, exposed to the DMSO solvent alone), suggesting a reparative effect of fluconazole.

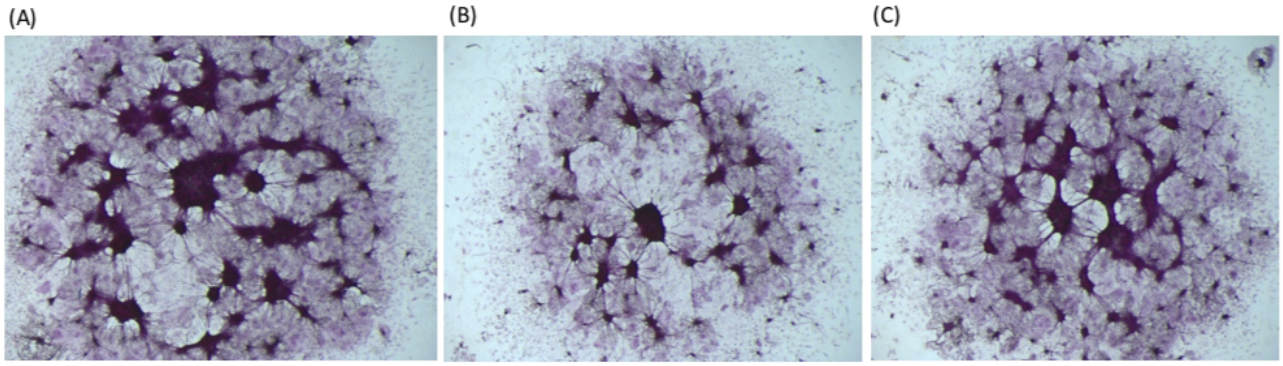

Figure 45. Micromasses at the end of the culture (7 days) treated with (A) vehicle, (B) 5HT at 50 μM and (C) 5HT at 50 μM with fluconazole at 50 μM.

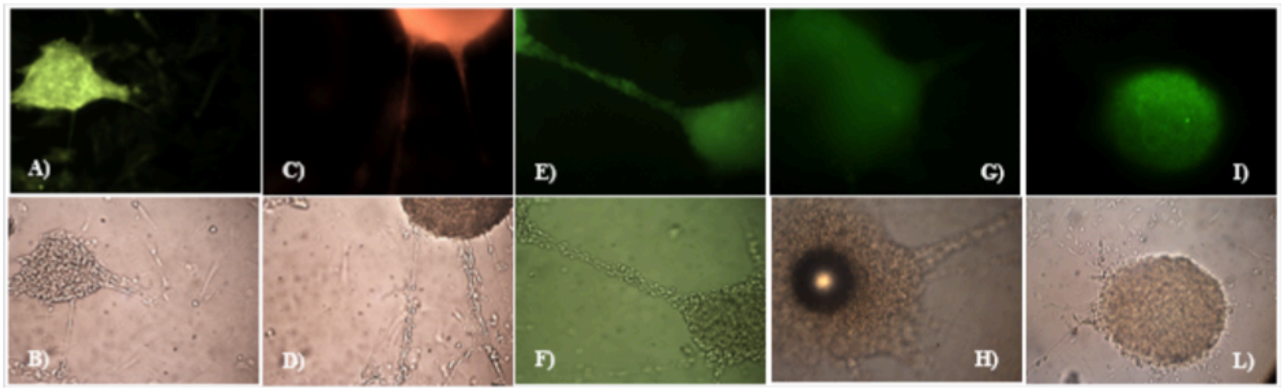

Figure 46. Micromasses immunostained control with specific antibodies; at the top (A, C, E, G, I) fluorescence image, at the bottom (B, D, F, H, L) respective microscopic differential contrast vision. A, B: NF 160; C, D: actin; E, F: Neu-N; G, H: CYP26A1; I, L: MBP.

Discussion/Conclusions

In this Part, seven azoles were selected to study their possible ability to induce remyelination by increasing RA concentration through inhibition of CYP26, an enzyme deputed to the catabolism of RA, therefore favouring OPC maturation and cell differentiation.
The results confirm that molecules interfering with the RA metabolic pathway indeed alter the myelination profile of differentiating OPCs when they are cultured alone or in the presence of neurons, providing the proof of concept of the remyelinating activity of CYP26 inhibitors and supporting the proposed mechanism of action i.e. that azoles may increase myelin levels in OPCs by inhibiting RA degradation operated by Cyp450 microsomal enzymes.
However, these data also suggest a differential anabolic behaviour for RA in OPC and DRG-neurons and, as a consequence, a different sensitivity of the two models to the RA synthesis inhibitor citral.
In addition, on the basis of these results, it can be hypothesized that citral itself can interfere with nuclear RA receptors pathway: further studies, however, are needed to elucidate whether this effect is direct or indirect.
From these data, itraconazole emerges clearly as the putative candidate for repurposing as it is the only molecule giving clear indication of increase in differentiation of OPC and of remyelination in OPC-DRG experiments.
Recent evidence from *in vivo*, *in vitro* and clinical studies has demonstrated also an anti-neoplastic effect of this conazole; it's safe use in humans and its low cost make it a viable option for future studies. By avoiding the lengthy process and cost-implications associated with bringing a novel drug to market, the potential repurposing benefits of itraconazole, both in demyelinating disorders and cancer, make it an attractive prospect.

Chapter 3 – Liver steatosis

Liver steatosis is a manifestation of liver toxicity. For instance, steatosis appears to be a prerequisite for the development of non-alcoholic fatty liver disease (NAFLD), a clinic-pathological condition encompassing a wide spectrum of liver damage, ranging from steatosis alone to steatohepatitis, advanced fibrosis and cirrhosis, and characterized by the accumulation of lipid droplets in the hepatocytes.
Hepatic steatosis is triggered by NRs activation through modulation of genes responsible for lipid homeostasis which subsequently leads to increase of *de novo* fatty acids/triglycerides synthesis and fat influx from the peripheral tissues to liver (Mellor *et al*., 2015). The accumulation of lipid in the hepatocytes can cause cytoplasm displacement, nucleus distortion, mitochondrial toxicity and eventually necrosis and/or apoptosis. The progression of this condition leads to tissue inflammation (steatohepatitis) and fibrosis with the involvement of other hepatic structures like the Kupffer (inflammation) and the stellate (fibrosis) cells.
Since NRs are involved also in this case, the molecular initiating event (MIE) is determined by an incorrect activation of NRs mediated by xenobiotic. This activation can affect simultaneously several NRs, since many xenobiotics have the ability to bind to two or more receptors. Figure 47 shows the LXR-mediated adverse outcome pathway (AOP), in which some NRs have common paths.

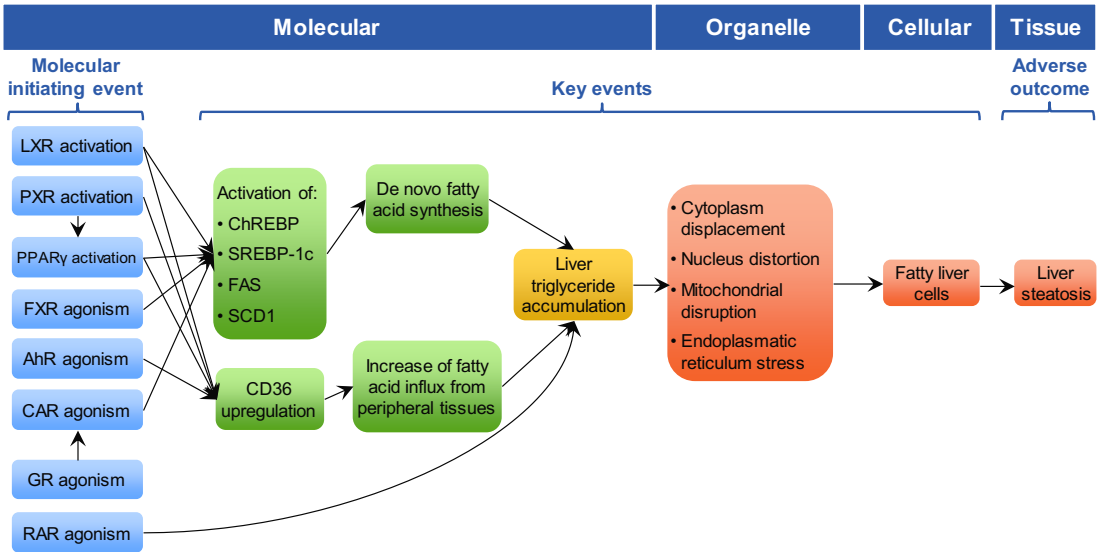

Figure 47. LXR-mediated AOP as example of adverse pathway for livers toxicity and, in particular, for steatosis (Source: EuroMix deliverable D3.2).

This MIE is common for all considered NRs, except for AHR that shows a 3D structure very different from the others. It is characterized by two different domains, PAS-A and PAS-B, that are involved in dimerization and molecular binding, respectively, without showing the same structural pattern in which the 12th α-helix of the others is determined (Mellor *et al*., 2015).
Chapter III discuss the pipeline of the procedures for prioritization and validation of chemicals as putative ligands and their application to the EuroMix chemical inventory, extending the study field to a set of nuclear receptors involved in hepatic steatosis. In particular, this chapter will be divided in two part in which we tested the *in silico* prioritization using a training set and we then applied our pipeline to the EuroMix chemical inventory. We also focused our attention on AHR, performing some *in vitro* experiments.

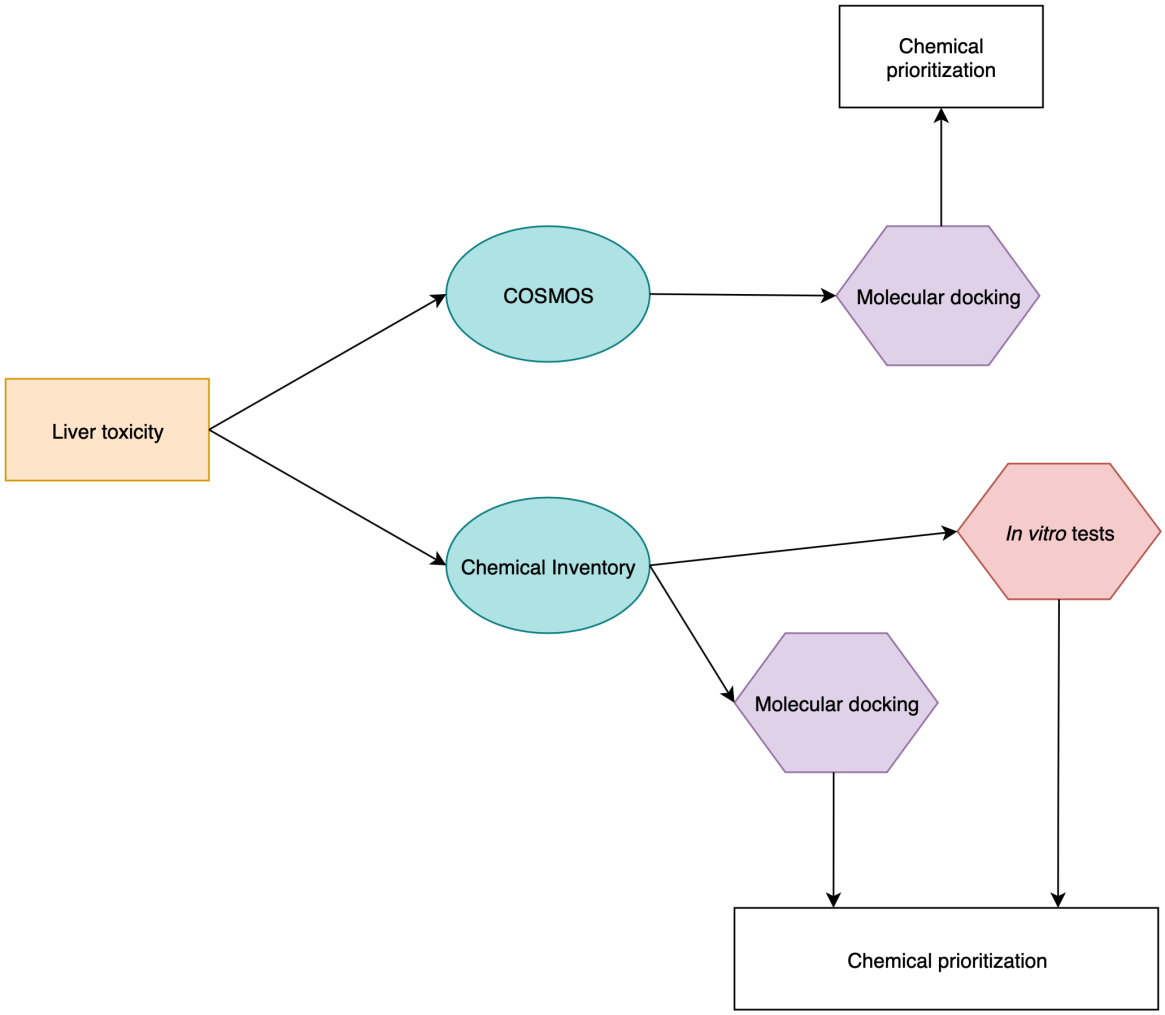

Figure 48: Liver toxicity *in silico* pipeline. Violet polygons represent structure-based approaches, while red polygon represent the *in vitro* tests. Endpoints are represented as white rectangle.

Results – Structure based approach

The selected crystallographic structures of NRs involved in hepatic toxicity are good 3D structures on which to perform all molecular docking calculations. In fact, the outliers, up to two *per* receptor, highlighted by the Ramachandran Plot analysis are placed in loops outside the binding region.
Moreover, NRs secondary structures are globally superimposable, with an average RMSD of about 4 Å. This high RMSD value is due to the fact that some receptors (e.g. PPARs, RARs and RXRs) exhibit both a much longer loop than the others and differ in the set-up of the β-sheets. If considered by themselves, α-helices are associated with a lower average RMSD value. The NRs structures analysis shows that among all NRs, PXR has a slightly different structure with respect to an average ensemble structure, because it has five β-sheets (of which two before the last α-helix) and an extended loop. In Figure 49, the structures of PXR and RARα are superimposed in order to show structural differences in both β-sheets and loops. 12th α-helices of the two NRs are perfectly coincident.

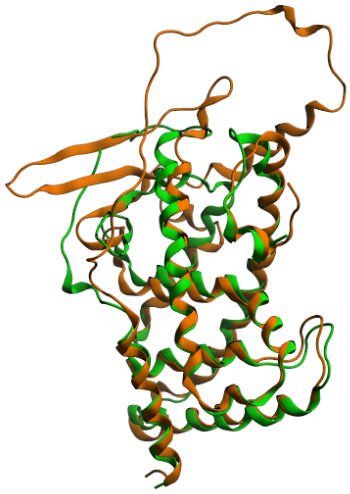

Figure 49. Superimposition of PXR and RARα secondary structures.

Analysing the binding site in each NR, it appears that the site defined by α-spheres is in good agreement with that determined by the ligand co-crystallized with each receptor. In addition, when receptors are in closed conformation all binding sites are occluded by the 12th α-helix.
As for AHR, a single outlier was found in Ramachandran plot; the affected amino acid, however, was part of a loop not involved in the binding site. The binding site found from the α-spheres analysis is in agreement with that identified by Bisson *et al* (Bisson *et al*., 2009); this site is smaller than the average of the other NRs.
Figure 50 shows the secondary structure of AHR PAS-B domain model with the identified binding site surface: as can be seen, AHR PAS-B (LBD) is totally different from other NRs and therefore it was not possible to make a direct comparison of its secondary structure with the other NRs.

Figure 50. AHR PAS-B domain secondary structure and its binding pocket surface computed as molecular surface.

Despite a sequence identity between the two sequences of only 25%, this AHR model is better than the one obtained by Bisson *et al* (Bisson *et al*., 2009); these authors built the model of the human protein starting from a model of mouse AHR and from the human HIF-2α PAS domain, using a two-step homology modelling procedure. A reference ligand of AHR, dioxin, docked to their model with a high binding energy value, suggesting that the structure was biased, at least in its binding site.

The analysis of the molecular docking results on the 16 different NRs involved in hepatotoxicity shows fewer specific results than the previous ones. This may be due to the fact that COSMOS training set does not include NRs as specific targets.
SSA statistic was applied to docking results, and two different energy cut-off values for different NRs were obtained. Tables 14, 15 and 16 report the specificity, sensitivity and accuracy values for different binding free energies (-5.5 kcal/mol, -5 kcal/mol and -4.5 kcal/mol) for all NRs, except AHR that will be individually discussed.

Nuclear receptor	Sensitivity	Specificity	Accuracy
CAR	0.62	0.57	0.60
FXR	0.58	0.62	0.60
LXRα	0.55	0.61	0.57
LXRβ	0.59	0.61	0.60
PPARα	0.55	0.67	0.61
PPARδ	0.55	0.63	0.58
PPARγ	0.57	0.61	0.59
PXR	0.59	0.66	0.62
RARα	0.55	0.61	0.57
RARβ	0.60	0.60	0.60
RARγ	0.61	0.55	0.58
GR	0.51	0.69	0.59
RXRα	0.59	0.63	0.61
RXRβ	0.70	0.45	0.59
RXRγ	0.58	0.61	0.59

Table 14: Cooper' statistic using the binding free energy of -5.5 kcal/mol as cut-off.

Nuclear receptor	Sensitivity	Specificity	Accuracy
CAR	0.78	0.45	0.63
FXR	0.70	0.51	0.62
LXRα	0.66	0.53	0.60
LXRβ	0.74	0.46	0.61
PPARα	0.66	0.55	0.61
PPARδ	0.69	0.51	0.61
PPARγ	0.74	0.46	0.62
PXR	0.69	0.54	0.62
RARα	0.74	0.44	0.61
RARβ	0.74	0.43	0.61
RARγ	0.78	0.41	0.62
GR	0.65	0.55	0.61
RXRα	0.72	0.48	0.61
RXRβ	0.88	0.28	0.61
RXRγ	0.72	0.44	0.60

Table 15: Cooper' statistic using the binding free energy of -5 kcal/mol as cut-off.

Nuclear receptor	Sensitivity	Specificity	Accuracy
CAR	0.88	0.25	0.60
FXR	0.83	0.36	0.62
LXRα	0.85	0.39	0.65
LXRβ	0.89	0.26	0.61
PPARα	0.83	0.38	0.63
PPARδ	0.84	0.36	0.63
PPARγ	0.90	0.26	0.61
PXR	0.83	0.38	0.63
RARα	0.88	0.19	0.57
RARβ	0.89	0.18	0.57
RARγ	0.91	0.20	0.59
GR	0.81	0.40	0.63
RXRα	0.90	0.24	0.61
RXRβ	0.98	0.06	0.57
RXRcγ	0.90	0.22	0.60

Table 16: Cooper' statistic using the binding free energy of -4.5 kcal/mol as cut-off.

Cooper' statistic values, that are considered best for each receptor, are highlighted in red in the previous tables. Figure 51 shows ROC curves for all selected NRs. It is very difficult to discriminate uniquely on the basis of SSA statistics which ΔG cut-off values can be the best to use in prioritization.

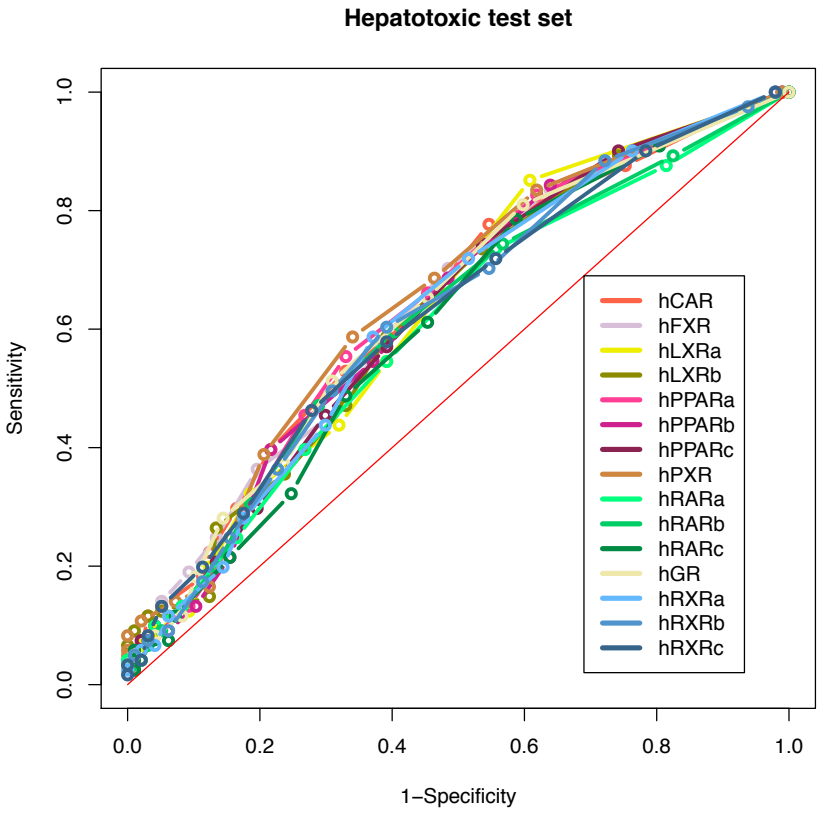

Figure 51. ROC curves for al NRs involved in steatosis. Points are representative of different binding free energy cut-offs.

In order to consider the overall MIE effect for each receptor, it was decided to use as the unique cut-off for hepatotoxicity the binding free energy value of -5 kcal/mol, that corresponds approx. to 100* E-06 for the dissociation constant (K_d).
For AHR, the following SSA statistic values were obtained using a cut-off of -5 kcal/mol: accuracy 0.46; sensitivity 0.39; specificity 0.56. These values are lower than for other NRs, because AHR has a much smaller binding site and therefore can bind only small ligands. AHR is more selective for these small ligands than other NRs involved in hepatotoxicity. This is evident in the database, in particular for very negative values of ΔG, in which the small aromatic ligands have a superimposed aromatic ring in their binding poses while bigger ligands have not-acceptable poses (or are not docked). Moreover, among the 16 top scoring compounds with ΔG less than -5 kcal/mol, only 5 are classified as hepatotoxic, while the other 11 are non-hepatotoxic.
Figure 52 shows the top scoring compound, with ΔG equal to -9.6 kcal/mol (left), and a compound that has a ΔG of 177 kcal/mol, equivalents to "not docked".

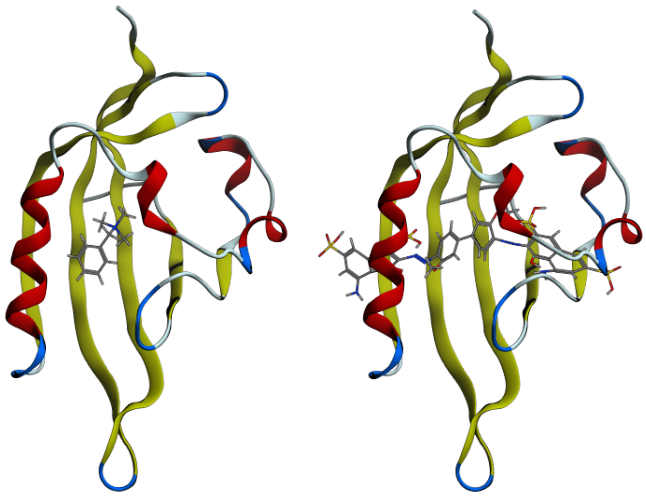

Figure 52. Top (left) and worst (right) scoring docking poses on AHR. Small ligands can be included in the small pocket with good binding free energies, while the very large ligands, even if they had bound, they would have had unacceptable poses for the AHR LBD due to its dimensions that are comparable with the length of AHR PAS-B.

Results – Structure-based approach

Analysing CI docking results on each NR selected for hepatotoxicity, it was found that approx. 90% of the compounds bind each receptor, when taking -5 kcal/mol as the cut-off value. Table 17 shows the number of prioritized compounds for each receptor, also considering a -6.5 kcal/mol cut-off, as for EAS, to operate a quantitative comparison; using the latter free binding energy value, the compounds selectivity decreases, shifting from about 90% to 40%-50%, except for AHR and RXRβ.

Nuclear receptor	Cut-off: -5 kcal/mol	Cut-off: -6.5 kcal/mol
AHR	337	53
CAR	928	599
FXR	909	501
LXRα	888	446
LXRβ	906	453
PPARα	927	513
PPARδ	889	425
PPARγ	905	389
PXR	923	433
RARα	904	393
RARβ	862	351
RARγ	927	473
GR	918	457
RXRα	909	414
RXRβ	952	709
RXRγ	911	430

Table 17. Number of prioritized chemicals for each NR, using two different cut-offs. CI is composed by 1193 different compounds.

The choice of this first cut-off value for this NRs was operated following the SSA statistics analysis of the molecular docking results, obtained from a non-specific training set for the selected NRs. Therefore, it is very likely that this has led to a systematic error, overestimating the real cut-off value and prioritizing compounds that should not have been. On the other hand, a structural analysis of selected NRs shows that they have a much larger binding pocket than the nuclear receptors for sex hormones. This detail could justify the pronounced difference observed in the number of compounds that can bind to the NRs. Moreover, it could be necessary to compute different cut-off values either for each nuclear receptor, or for each toxicological outcome (e.g. hepatotoxic, steatosis, cholestasis, etc). AOPs of these toxicological outcomes involve different NRs in different biochemical pathways, increasing the system complexity. All the prioritized chemicals were further studied both *in vitro* and *in vivo* by EuroMix partners, and the results of these studies are published in EuroMix Deliverables on EuroMix web page (https://www.euromixproject.eu/).

In addition, there is an important difference between AHR and all other NRs prioritization results., With a cut-off of -5 kcal/mol, AHR binds about 35% of the compounds, but with a cut-off of -6.5 kcal/mol, it binds only 5% of them. This fact can be explained by the structural considerations already made on the AHR binding site, and its ability to bind only small ligands.

For this reason, in collaboration with the German Federal Institute for Risk Assessment, German Centre for the Protection of Laboratory Animals (Bf3R) within the EuroMix Project, we further investigated the Propiconazole::AHR complex. In a first step molecular docking simulations were performed to assess *in silico* whether propiconazole (Pi) can bind the ligand binding domain of human AHR. A negative ΔG value of -3.8 kcal/mol was predicted (Figure 53.A), suggesting that an association between the AHR and Pi is favourable from an energetic point of view. TCDD, a reference ligand for AHR, showed a ΔG value of -5.0 kcal/mol (Figure 53.B). This can still be regarded as a critical value, indicating that the human AHR ligand binding domain interacts rather weakly with its reference ligand. The superposition of TCDD and Pi in the AHR ligand binding site showed a partial overlap of the aromatic rings of these two chemicals (Figure 53.C). The predicted ΔG value is suggestive but not sufficiently negative to firmly support the binding of Pi to AHR, just on the basis on our *in silico* data.

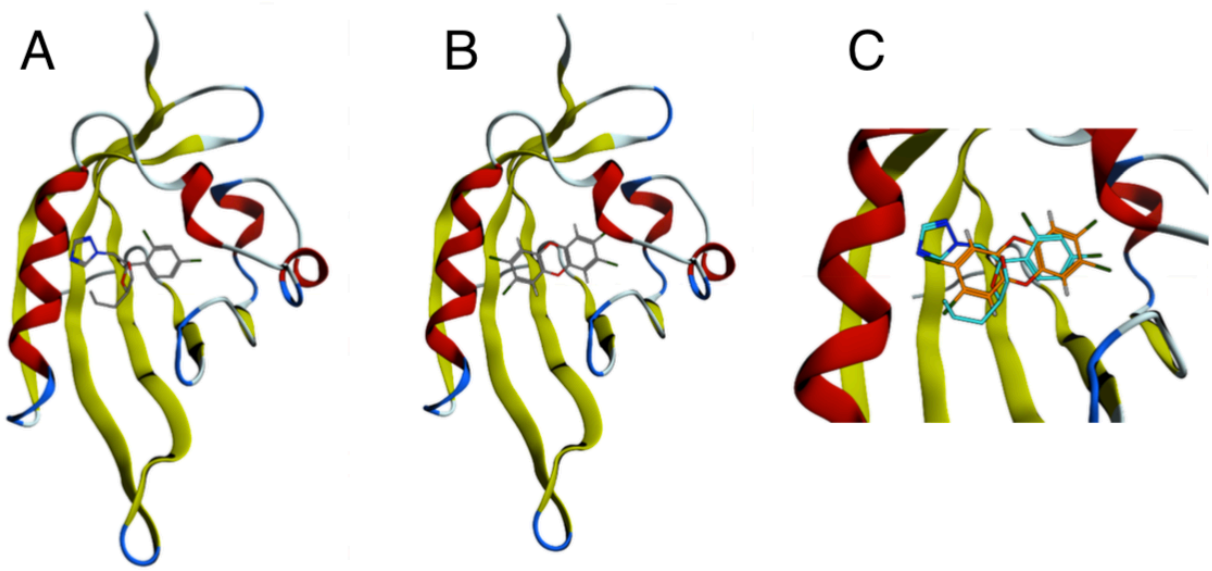

Figure 53: *In silico* molecular docking analyses of Pi to the AHR ligand binding domain are shown as graphic representations of the top-scoring complexes between Pi and AHR (A), the reference AHR ligand TCDD and AHR (B), and a superposition of Pi and TCDD (C).

Results – AHR *in vitro* assay

These results have already been published in Knebel et al. (2018) in the EuroMix framework.

Microarray gene expression data indicate AHR activation by Pi in human cells

In the course of an *in vitro* study aimed at investigating the global transcriptomic responses of human liver cells to the fungicidal active substance Pi, we discovered that Cyp1A1 and Cyp1A2, the most classic target genes of the nuclear receptor AHR, were among the top upregulated genes in HepaRG hepatocarcinoma cells. Microarray analysis was verified by conventional real-time RT-PCR of Cyp1A1 and Cyp1A2. The literature-based bioinformatic IPA (Ingenuity Pathway Analysis) was used to unravel possible further hints for AHR activation by Pi. These analyses revealed that other genes which have been previously linked to AHR activation were also altered by Pi (Figure 54).

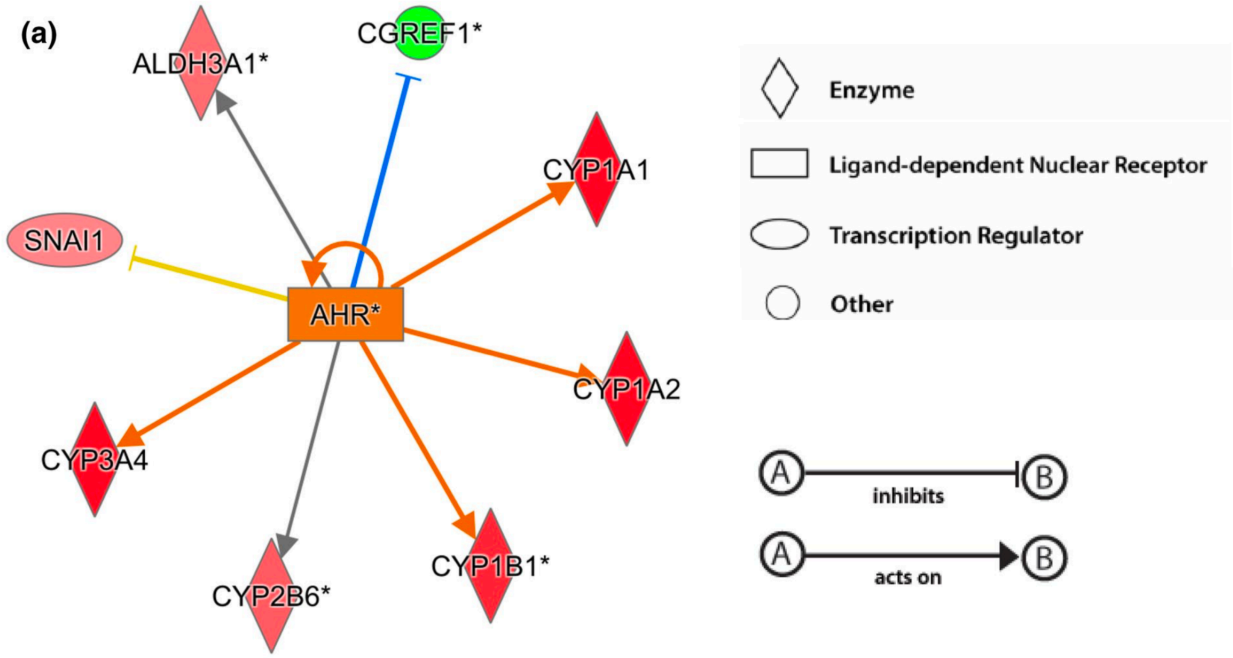

Figure 54: Bioinformatic data mining and in silico modeling indicate a possible interaction of propiconazole (Pi) with the AHR. a Bioinformatic analysis of microarray gene expression data with IPA indicates AHR activation by propiconazole (Pi) in HepaRG cells. The global transcriptomic responses of HepaRG cells to 10 µM Pi were analysed with the help of the microarray Agilent Expression Profiling Service. Ingenuity Pathway Analysis (IPA) of the data indicates that classic target genes of the nuclear receptor AHR were up- (red) or downregulated (green). Duplicates gene identifiers marked with an asterisk (*) indicate that multiple identifiers in the dataset file map to a single gene in the Global Molecular Network. Colours of the connections represent the predicted relationships [activation (orange), inhibition (blue), findings consistent with state of downstream molecule (yellow), and effects not predicted (grey)].

For most of these genes the direction of regulation was in line with previously published data on AHR-dependent activation or inhibition (Figure 54). As the results from bioinformatic data mining indicated a possible involvement of AHR in Pi-induced effects in human liver cells, further experiments were performed for verification.

Pi effects on AHR-dependent transcription, target mRNA, protein amount, and enzyme activity
In a following step we therefore analysed whether Pi would activate AHR-dependent transcription using a luciferase reporter system driven by either a 1.2 kbp fragment of the human Cyp1A1 promoter, a similar Cyp1A1 promoter-derived luciferase reporter lacking the four functional AHR binding sites ("-CDEF"), or an artificial promoter construct consisting of three AHR-responsive DRE sequences ("3xDRE"). As shown in figure 56, Pi dose-dependently induced luciferase reporter activities from the Cyp1A1 promoter and 3xDRE constructs in HepG2 human hepatoma cells with statistical significance, whereas no induction was visible with the AHR binding site-deficient mutant (-CDEF) reporter (Figure 55). When compared to the positive control, the aromatic hydrocarbon and known AHR inducer Benzo[b]fluoranthene (BbF), it became obvious that Pi showed an onset of reporter gene activation only at substantially higher concentrations than needed for BbF to produce a response. Thus, Pi constitutes a substantially weaker AHR activator than BbF. Analyses of Pi-induced effects at higher concentrations than 40 μM, in order to add information to the right side of the dose-response-curve, were hampered by cytotoxic effects occurring at these concentrations. To exclude that the observed AHR activation was caused by impurities potentially present in technical grade Pi, the experiments were repeated with analytical grade Pi and the results were reproduced.

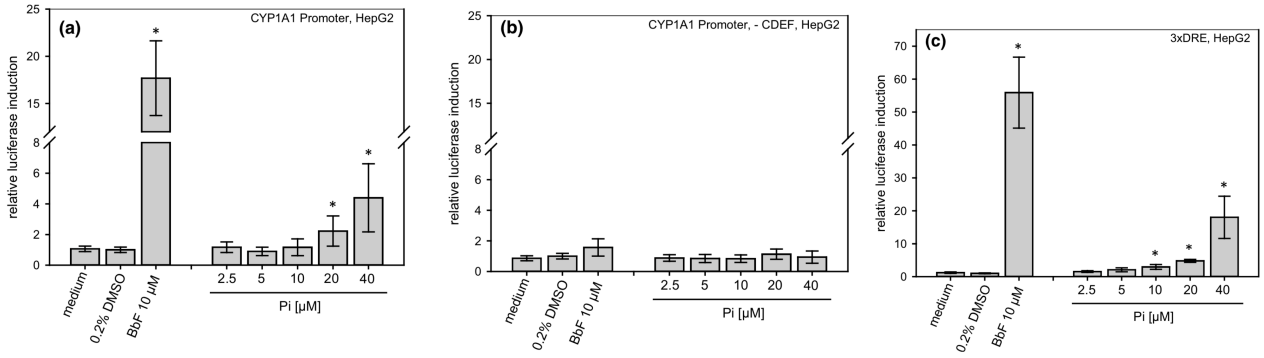

Figure 55: Propiconazole (Pi) induces AHR-dependent transcription in ▸ HepG2 cells. a Dose-dependent induction of a luciferase reporter system driven by a 1.2-kbp fragment of the human CYP1A1 promoter. By contrast, no induction is measurable with a similar reporter lacking the four functional AHR binding sites ("-CDEF"). c Pi also leads to a dose-dependent induction of the artificial promoter construct consisting of three AHR-responsive DRE sequences ("3xDRE"). Induction by the model AHR ligand BbF is shown for comparison. Fold induction above solvent control (0.2% DMSO) was calculated. Mean±SD (n=3 independent experiments, each in three replicates) is depicted. Statistical significance ($p<0.05$) against the solvent control is indicated by asterisks

Dose-dependent induction of AHR activity was subsequently confirmed by real-time RT-PCR analyses of the model AHR target genes Cyp1A1 and Cyp1A2 in HepaRG cells (Figures 56A and 58B). These results well resembled the findings at the reporter gene level. Expression of the AHR mRNA itself was not altered (data not shown). In addition, abundance of Cyp1A1 was quantified at the protein level using a mass spectrometry-based approach. Results of these analyses showed Pi-dependent induction of Cyp1A1 protein (Figure 56C), consistent with the findings presented above. To further substantiate our findings, we studied Cyp1A1-dependent catalytic activities using the classic EROD (ethoxyresorufin-O-deethylase) assay for Cyp1A1 activity. Figure 56 demonstrates that Pi was able to significantly induce Cyp1A1-dependent enzymatic substrate conversion in human HepaRG cells in a dose-dependent manner.
Similar effects were observed in rat liver: Cyp1a1 and Cyp1a2 gene expression was significantly increased at the top dose level in Pi-treated rats (Figure 57A and 57B). Additionally, Cyp1a1 and Cyp1a2 enzyme activities were significantly increased in a dose-dependent manner (Figure 57C and 59D).

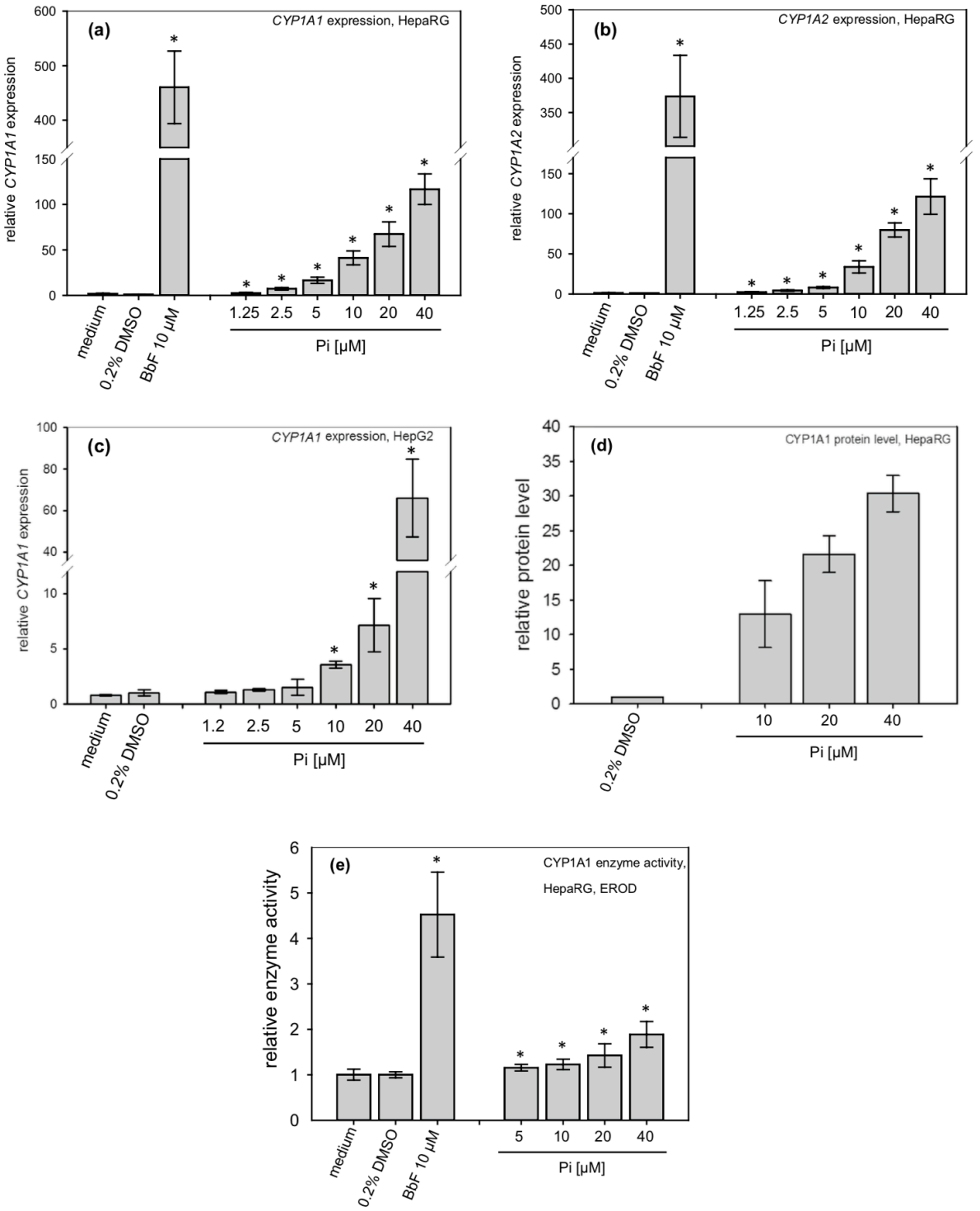

Figure 56: Propiconazole (Pi) is an agonist of human AHR. Induction of CYP1A1 (a) and CYP1A2 (b) mRNA levels in HepaRG human hepatoma cells and CYP1A1 (c) in HepG2 human hepatoma cells by Pi, as measured by quantitative real-time RT-PCR. d Pi-dependent induction of CYP1A1 protein level was observed by using a mass spectrometry-based approach. e Induction of CYP1A1 enzyme activity by Pi, as measured by the EROD assay. Fold induction above solvent control (0.2% DMSO) was calculated. Mean±SD (n≥3) is depicted. Statistical significance ($p<0.05$) against the solvent control is indicated by asterisks. No statistical significance was calculated for the data in panel d, due to the fact that these values were not derived from entirely independent experiments

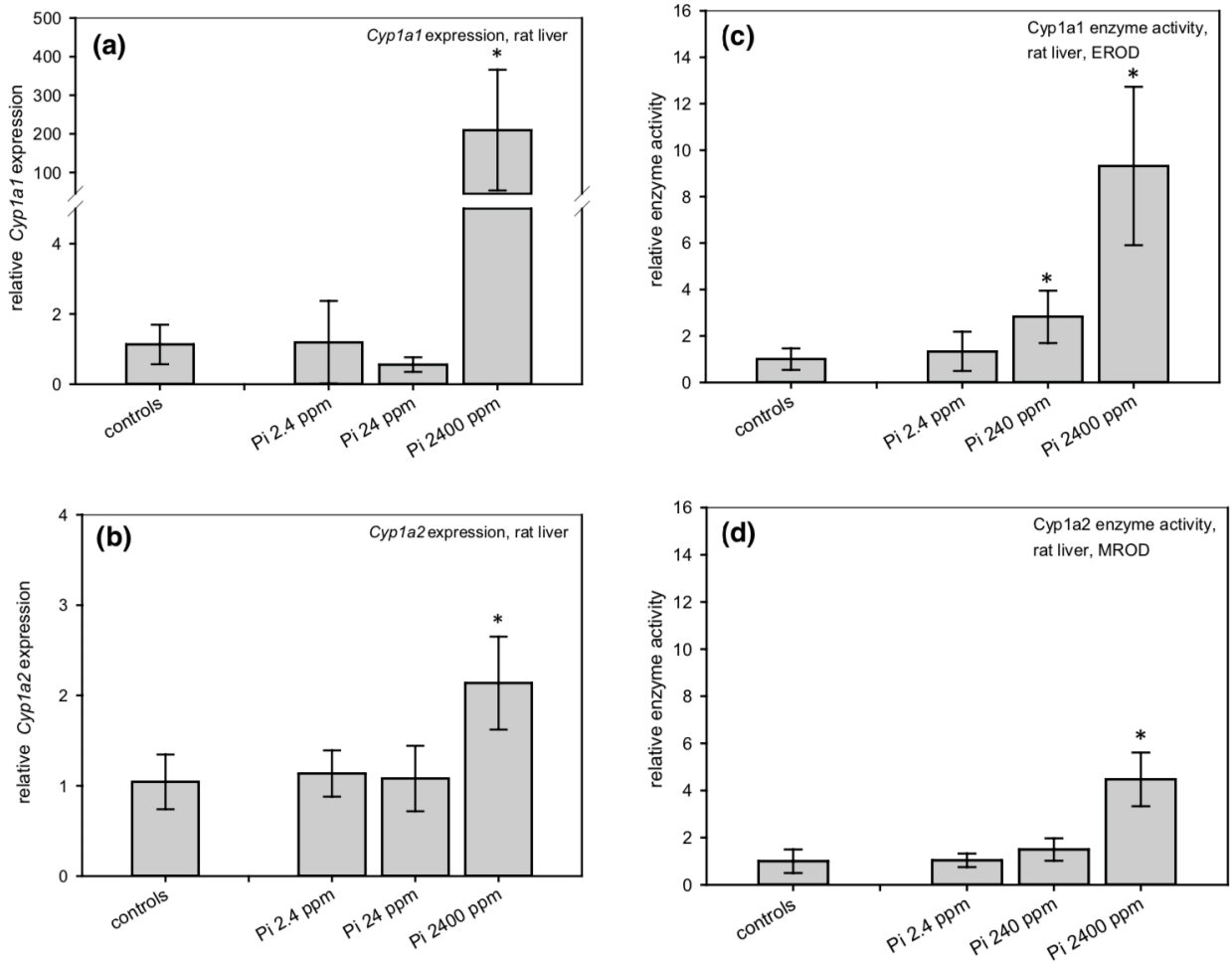

Figure 57: Propiconazole (Pi) induces AHR target genes and resulting enzyme activities in rat livers obtained from a 28-day feeding study at dose levels of up to 2400 ppm. Pi leads to an induction of Cyp1a1 (a) and Cyp1a2 (b) mRNA levels in rat livers as well as to an induction of the enzyme activities of Cyp1a1 (c) and Cyp1a2 (d). Figures show fold induction relative to the respective controls. Mean ± SD (nbiological = 5) is depicted. Statistical significance ($p<0.05$) against the control animals is indicated by asterisks

Effects of Pi in AHR KO, PXR KO and CAR KO HepaRG cells

Three HepaRG cell lines deficient of either AHR, PXR or CAR were treated with Pi and Cyp1A1 and Cyp1A2 gene expression was analysed to investigate if Pi-induced gene expression was mediated by either of the three receptors. Involvement of CAR and PXR in Pi-dependent gene regulation has been reported previously. As shown in Figure 58, Cyp1A1 and Cyp1A2 upregulation was completely blocked in AHR KO cells. Comparable results were seen when using HepG2 cells treated with a pharmacological inhibitor of the AHR and a Cyp1A1 promoter-driven reporter. In contrast, Cyp1A1 and Cyp1A2 gene expression was upregulated in a concentration-dependent manner in both PXR KO cells as well as CAR KO cells, similar to wildtype cells. These results indicate that knocking out PXR and CAR has no remarkable influence on the upregulation of these genes by Pi, whereas the presence of the AHR is crucial.

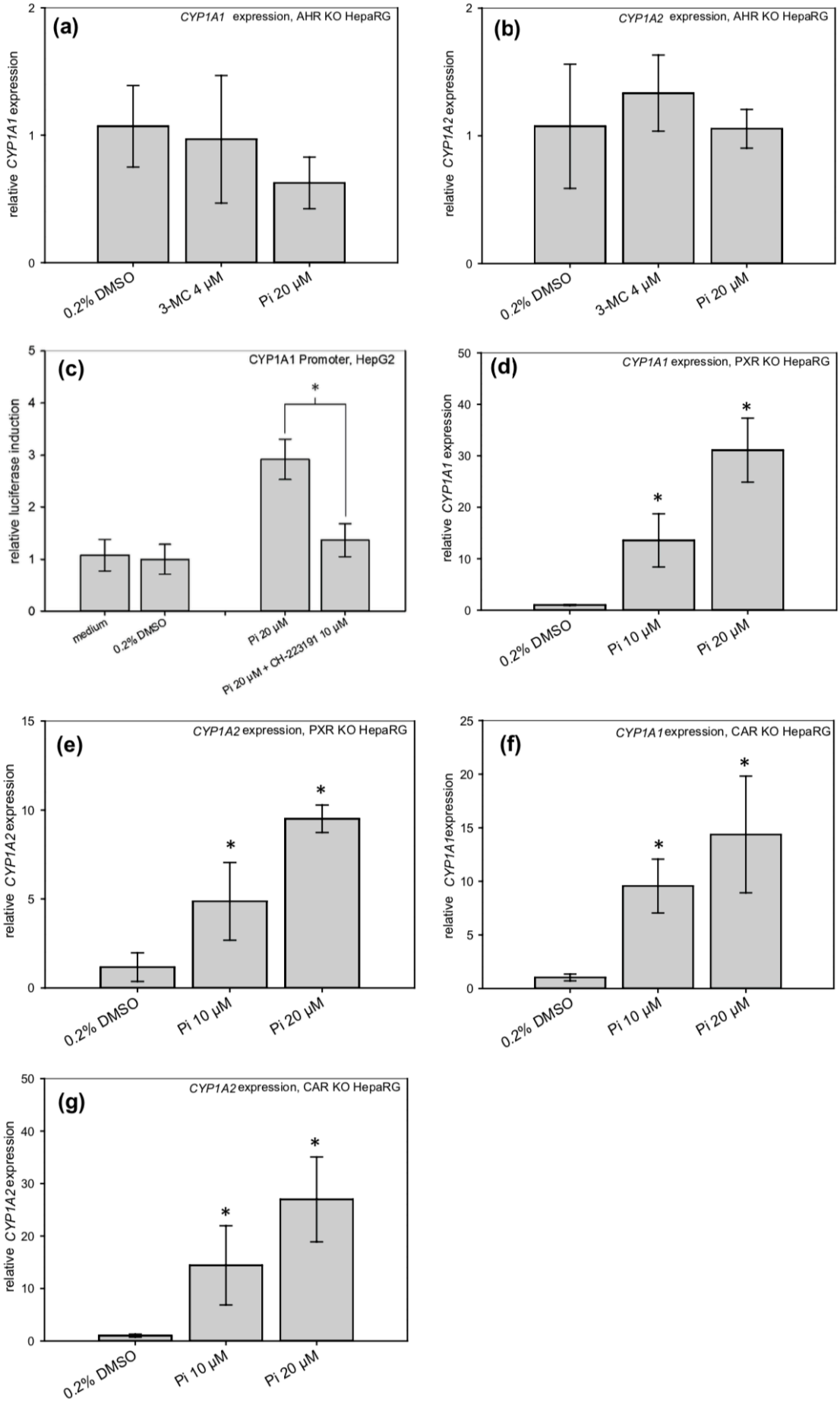
(a)
CYP1A1 expression, AHR KO HepaRG
relative CYP1A1 expression
0.2% DMSO
3-MC 4 µM
Pi 20 µM
(b)
CYP1A2 expression, AHR KO HepaRG
relative CYP1A2 expression
0.2% DMSO
3-MC 4 µM
Pi 20 µM
(c)
CYP1A1 Promoter, HepG2
relative luciferase induction
medium
0.2% DMSO
Pi 20 µM
Pi 20 µM + CH-223191 10 µM
(d)
CYP1A1 expression, PXR KO HepaRG
relative CYP1A1 expression
0.2% DMSO
Pi 10 µM
Pi 20 µM
(e)
CYP1A2 expression, PXR KO HepaRG
relative CYP1A2 expression
0.2% DMSO
Pi 10 µM
Pi 20 µM
(f)
CYP1A1 expression, CAR KO HepaRG
relative CYP1A1 expression
0.2% DMSO
Pi 10 µM
Pi 20 µM
(g)
CYP1A2 expression, CAR KO HepaRG
relative CYP1A2 expression
0.2% DMSO
Pi 10 µM
Pi 20 µM

Figure 58: Upregulation of AHR target genes was blocked in AHR KO cells. No induction of CYP1A1 (a) and CYP1A2 (b) gene expression was measured in AHR KO cells after treatment with the positive control 3-methylcholanthrene (3-MC) or Pi. c Additionally no transactivation of CYP1A1 promoter was measured with 10 µM of the AHR inhibitor CH223191. In contrast, investigation of CYP1A1 and CYP1A2 in PXR KO (d, e) and CAR KO (f, g) cells showed concentration-dependent upregulation, indicating that the latter two nuclear receptors are not involved in Cyp1a1/2 induction by propiconazole. Fold induction above solvent control (0.2% DMSO) was calculated. Mean±SD ($n \geq 3$) is depicted. Statistical significance ($p<0.05$) against the solvent control (a, b, d–g) or the treatment with the antagonist (c) is indicated by asterisks.

Combination effects of Pi and the model AHR ligand BbF

According to a previous publication linking Pi and rodent AHR, Pi alone activates the rodent AHR but might inhibit the response to model AHR ligands (Ghisari *et al*., 2015). We therefore exposed human hepatic cells *in vitro* to mixtures of Pi and BbF, a model AHR activator routinely used in our laboratory. Figure 59 demonstrates that no inhibition of BbF-mediated induction of AHR-dependent 3xDRE reporter activity was observed when applied in combination with Pi. Instead, data were consistent with the assumption of concentration addition. When analysing mRNA induction of Cyp1A1 and Cyp1A2 in response to Pi and BbF mixtures, concentration addition was observed. The analysis of enzyme activity of Cyp1A1 in the EROD-Assay showed similar results.

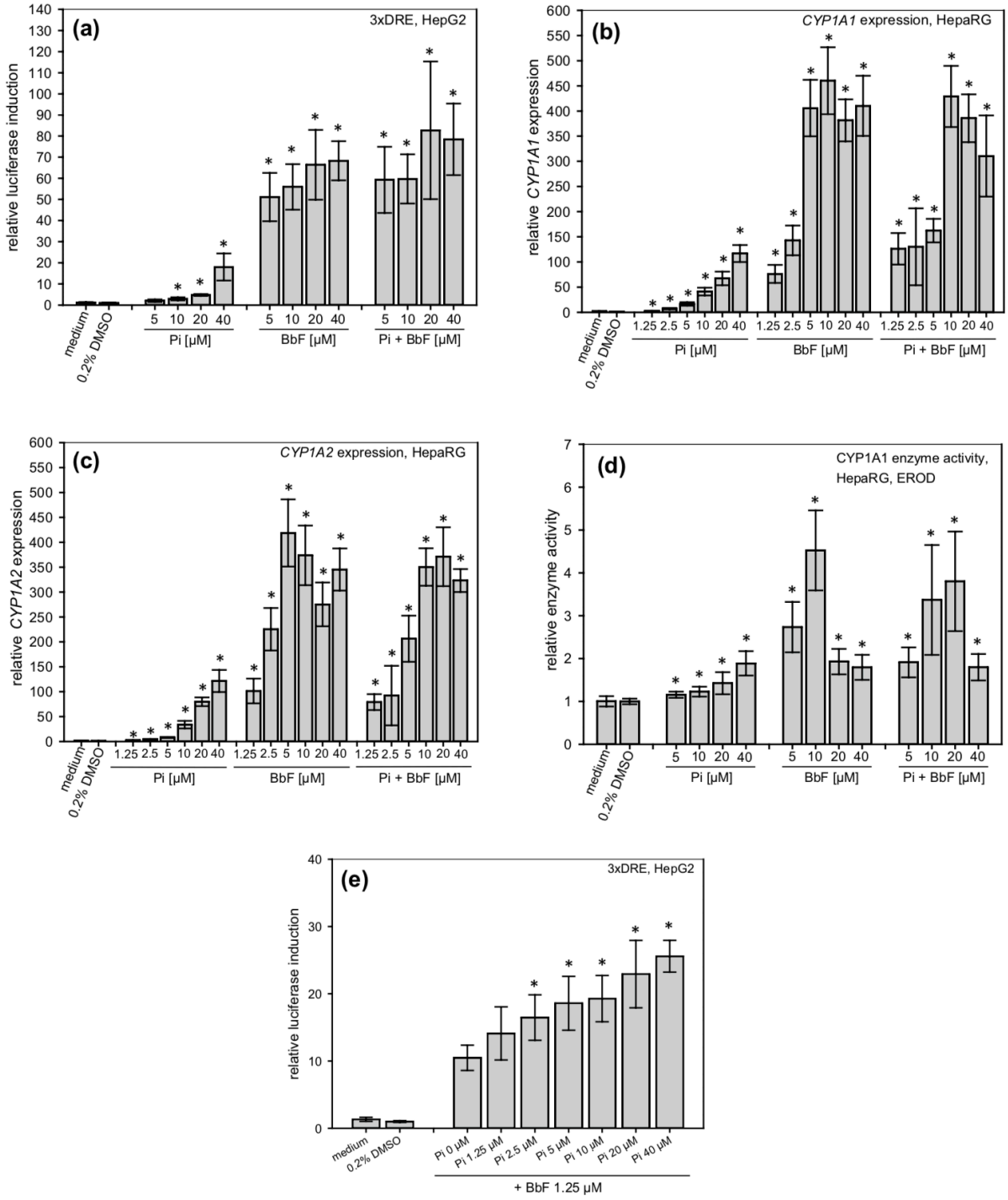

Figure 59: Propiconazole (Pi) and the more potent model ligand benzo[b] fluoranthene (BbF) have concentration additive effects on human AHR. a) Pi and BbF both lead to a dose-dependent induction of the artificial 3xDRE promoter construct. Mixtures of both compounds suggest con- centration additive combination effects on AHR activation. Further- more, induction of b) CYP1A1 and c) CYP1A2 mRNA levels in human HepaRG cells by Pi and BbF shows concentration additivity. d) The results from the EROD assay, which shows the induction of CYP1A1 enzyme activity by Pi and BbF, are also in line with concentration additivity. e) The results of the AHR-dependent 3xDRE reporter gene assays with a fixed BbF concentration show that Pi enhances the effect of BbF dose-dependently. This indicates additive behaviour of the combination. Fold induction above solvent control (0.2% DMSO) was calculated. Mean±SD (n=3 independent experiments, each in three

replicates) is depicted. Statistical significance ($p<0.05$) against the solvent control or the BbF treatment without Pi (e) is indicated by asterisks

Discussion/Conclusions

Among all the nuclear receptor studied, AHR is the most interesting one, due to both its tiny binding pocket and its fold. Globally, all the other tested nuclear receptors are very sensible to the tested chemicals binding, due to their unselective binding pockets. For these reasons, only 10 prioritized chemicals for each NR where further studied both *in vitro* and *in vivo* by EuroMix partners. Results are not reported in the present thesis, where we focused our attention on AHR.
In fact, data presented in this Part clearly demonstrate that Pi is an activator of the human AHR, as consistently shown by analyses at the reporter gene, mRNA expression, protein abundance, and enzyme activity levels in HepG2, HepaRG, or HepaRG variants bearing knockouts of individual nuclear receptors. Furthermore, investigation of gene expression and enzyme activity in rat livers showed induction *in vivo* of the AHR targets Cyp1a1 and Cyp1a2.
So far, only few previous publications have established indirect links between Pi and AHR. (Sun *et al*., 2005) administered Pi to rats and observed an induction of Cyp1a2 gene expression and the resulting enzyme activity without analyzing receptor binding and transactivation. (Li *et al*., 2013) measured induced hepatic EROD activity in juvenile rainbow trout exposed to Pi versus a control group. They suggest that Pi had toxic effects in the fish through binding to the aryl hydrocarbon receptor (AHR) without analysing receptor binding or transactivation. In human intestinal cells, an increase of Cyp1A1 activity after treatment with imazalil and other conazoles like Pi has been reported (Sergent *et al*., 2009). However, imazalil was shown not to bind AHR while Pi was not investigated. (Ghisari *et al*., 2015) have screened various compounds for activation of rodent AHR using a murine cell line stably transfected with an AHR-responsive reporter construct; they reported a concentration of 10 μM Pi as the lowest dose to exert an effect. Given the differences in incubation conditions and reporter system used, these results appear well in line with our present findings, indicating that Pi is a weak agonist of human as well as rodent AHR. Altogether, the present data on AHR activation by Pi go far beyond what has been published previously by Ghisari *et al*. (2015) who followed a screening approach in a rodent cell system rather than systematically characterizing the properties of an individual compound in human hepatic cells, as was the focus of our study.
While the AHR has initially been believed to become activated rather specifically by polycyclic aromatic compounds, such as (halogenated) polycyclic aromatic hydrocarbons, dioxins, and certain polyhalogenated biphenyls, more recent data have revealed that numerous other compounds not exactly fitting into this class of molecules are capable of activating the receptor. For example, certain experimentally used ATP-competitive kinase inhibitors such as U0126 and SB216763 (Andrieux *et al*., 2004; Braeuning and Buchmann, 2009), phytochemicals such as isoflavones (Van der Heiden *et al*., 2009) and also endogenous metabolites such as kynurenine (Opitz *et al*., 2011) are activators of the AHR, which, however, in most cases do not share the potency or the long biological half-life of the model activator TCDD. The present observations thus fit well into this picture of a somewhat promiscuous receptor. Since species-specific differences with regard to the agonistic properties of foreign compounds at different nuclear receptors have been noted, it is important to show activation of the human receptor to draw a conclusion as to the relevance for humans. A very prominent example of species-species differences is the receptor CAR, where CITCO is considered a specific agonist of human CAR, whereas TCPOBOP activates the receptor in mice but not in humans (Tzameli *et al*., 2000). However, such observations are not limited to CAR: the best-studied AHR activators, e.g. TCDD or polycyclic aromatic hydrocarbons, generally activate both, the AHR of humans and rodents. They do so, however, with sometimes remarkable quantitative differences: for example, binding of TCDD to the human AHR has been reported to occur with approximately 10-fold lower affinity than for the most common AHR variants expressed in the mouse (Ema *et al*., 1994). Similar differences

have been observed for other AHR ligands and also for species other than only humans and rodents, as for example documented in detail in (Denison *et al*., 2011; Flaveny *et al*., 2009). Species differences have also been described with respect to AHR antagonists, for example SR1, which acts as an antagonist of human but not of rat AHR (Boitano *et al*., 2010). These observations underline the importance of conducting studies with human cells in order to assess possible toxicological consequences of nuclear receptor activation by foreign compounds in humans. It has to be noted that comparative analyses of the response of the AHRs from different species are not routinely performed, as can be concluded from the lack of such data in many publications identifying novel AHR agonists. In the paper by Ghisari *et al*. (2015) it is mentioned that Pi attenuated the AHR-inducing effects of the model AHR activator TCDD in the murine cell system used there. As, however, no exact values are given, one cannot judge the strength and/or significance of this observation. Due to the fact that toxicological effects of mixtures have become an increasingly important topic during the past years, we investigated how Pi and the model AHR ligand BbF jointly influence AHR activity in human cells. Our results do not support the abovementioned finding by Ghisari *et al*. (2015) according to which one would expect AHR activation by a model ligand to be diminished by Pi. Instead, our findings are in line with a model of concentration addition. The validity of this model for AHR activators constitute the basis of current assessment of classic AHR activators: for these substances, additivity is assumed and concentrations of individual substances, multiplied by their equivalence factor (a measure for their potency relative to TCDD) can be added in order to predict a mixture effect. Our present data suggest that this type of additivity is also valid for mixtures of Pi with other AHR activators.

Pi belongs to a large family of frequently used fungicidal active substances, the triazole fungicides. These compounds are closely related with respect to their molecular structure. The finding that Pi is an AHR activator thus triggers the question whether this holds also true for other members of this chemical class. We have investigated two related substances, namely cyproconazole and tebuconazole. We could not observe any AHR activation after treatment with cyproconazole or tebuconazole when tested with the sensitive endpoint of luciferase reporter analysis up to the highest possible non-cytotoxic concentrations (own unpublished data). Instead, cyproconazole acts as an activator of human and rodent PXR and also rodent but not human CAR (Marx-Stoelting *et al*., 2017), whereas tebuconazole also activates PXR but is an antagonist of CAR (Knebel *et al*., 2018). Together these observations demonstrate that, despite evident similarities at the level of chemical structure, the molecular targets of these substances differ considerably. This might have implications for risk assessment, where adverse effects in the liver following activation of certain nuclear receptors by xenobiotics is not considered relevant for humans, as in case of the peroxisome proliferator-activated receptor (PPAR) alpha (Corton *et al*., 2014), or is subject of a controversial scientific debate, as in case of CAR activation (Braeuning *et al*., 2014; Braeuning *et al*., 2016; Braeuning *et al*., 2015; Elcombe *et al*., 2014; Yamada *et al*., 2014). By contrast, the most potent and specific xenobiotic inducer of the AHR, TCDD, has been classified as carcinogenic to humans by the International Agency for the Research on Cancer (IARC) and others (Baan *et al*., 2009). Different triazole fungicides appear to activate different sets of nuclear receptors and show variable potencies at the individual receptors. Adverse liver effects in experimental animals exposed to such substances might be contributed to by a single receptor or by a combination of multiple receptors simultaneously activated by a certain compound. Based on classic histopathology, it appears almost impossible to deduce a specific molecular mechanism from observations at the tissue level. Many adverse outcome pathways (AOP) describing adversity as a sequence of molecular events triggering an adverse outcome at the organ level contain multiple molecular initiating events which later converge at the cellular level (www.aopwiki.org). For example, the AOP for liver steatosis comprises almost all important nuclear xeno-sensing receptors, such as AHR, CAR, PXR, and PPAR. Proof of activation of a certain receptor by a chemical does not always allow drawing conclusions on the prevailing molecular mechanisms, since a compound, e.g. a triazole, might be able to simultaneously act on a whole set of receptors. Thus, when judging on the human relevance of experimental data, not only

possible species differences with respect to ligand-receptor interaction should be considered, but it should also be regarded as important to keep in mind that mechanistic toxicological argumentation for or against human relevance of a certain adverse effect should involve the different possible modes of action which are driven by individual nuclear receptors but lead to a similar adverse outcome.

Chapter 4 – Material and Methods

This Chapter is organized as follows: general materials and methods, e.g. chemical inventory, homology modelling procedures and molecular docking, are flagged as "general" and convey transversal information. Specific methods, on the other hand, are flagged with their respective Chapter and Part for greater clarity.
In Chapter 2, Part II and Part V sections, please refer to original manuscript for *in vitro*/*in vivo* procedures.

Chemical Inventory – General

EUROMIX chemical inventory

The EUROMIX chemical inventory (CI) is a broad list of chemical substances that was developed in the frame of the EuroMix (European Test and Risk Assessment Strategies for Mixtures), an Horizon2020 project in which University of Milan is involved. The selection of the compounds included in the CI was based on the principle that CI should include substances from several chemical categories. Therefore, in this extensive list of chemicals approximately one thousand substances have been included representing different chemical categories i.e. pesticides (plant protection products and biocides), environmental pollutants (e.g. dioxins, PAHs, PCBs, PBDE, PFAS, PBBs), food contaminants (e.g. mycotoxins), food contaminants materials (FCM) and bioactive alkaloids (e.g. pyrrolizidine alkaloids), metals, pharmaceuticals and miscellaneous chemicals. This list was used as a starting point for the prioritization task *via in silico* procedures in order to discriminate among chemicals which should be further investigated with *in vitro* or *in vivo* studies.

For each chemical, information was provided regarding its identity, i.e. the substance chemical common name (or structural name in case of environmental pollutants), the chemical category (for plant protection products only), the chemical class, the product type (for Non-intentionally added substances (NIAS) and FCM migrants only) and the CAS number. Table 18 reports the number of chemical substances for each chemical category.

Chemical Category		No. of Chemical Substances
Pesticides	**Plant Protection a.i.**	501
	Biocidal a.i.	34
Non-pesticides	**NIAS & FCM migrants**	66
	Mycotoxins	20
	Alkaloids	40
	Environmental pollutants	308
Other chemicals		224

Table 18: Summary of EuroMix chemical inventory.

The selection of the compounds included in CI was performed by EuroMix research group and it was based on the principle that CI should be as broad as possible including substances with a well-known toxicological profile, representative of different chemical categories that could be of relevance for dietary exposure. In this respect, the compounds included in each category of the CI were selected considering three main parameters:

i) *chemical variability*, in order to ensure that a wide range of chemicals has been considered and,
ii) *food safety relevance (e.g under discussion at EFSA)*, and/or
iii) *toxicological data availability*, since for each of the substances in the CI specific toxicological parameters have to be collected for the development of a hazard-based database.

CI structures were provided in 2D *.sdf* format and then, 3D structures were generated through the minimization procedure contained in the MOE Builder module. Structures were manually verified in order to check if the minimization step had solved the most complex structures. Amber10::ETH was used as a force field for all procedures.

Chemical Inventory for developmental toxicology

Twenty-eight different triazoles were selected with the aim of creating the CI for this area of study on developmental toxicology, basing on literature (Menegola *et al*. 2001; Menegola *et al*. 2016; Di Renzo *et al*. 2011). The azoles 3D structures were selected starting from a search in PubChem and subsequently verified and optimized through an energy minimization procedure carried out with the

MOE Builder module. The stereochemistry of these structures was then analysed and, when necessary, the stereoisomers were generated.
In addition, the binding free energy of retinoic acid was considered as a positive reference value, and both ethanol and valproic acid were also included in CI for developmental toxicology. In particular, ethanol was included in the database because of its relevance for the PhD project, since there are clinical reports that describe synergic effects between ethanol and azoles taken for therapeutic reasons by women, unaware of being pregnant, causing developmental foetal defects. Valproic acid, on the other hand, was included in the CI as a reference compound for teratogenic effects (Di Renzo *et al.* 2010). Amber10::ETH was used as force field for all procedures. The database composition is listed in Table 19.

Chemical Category		No. of Chemical Substances
Azoles	**Triazoles**	28*
Non-azole	**Substrate**	1
	Ethanol	1
	Other	1

Table 19: Summary of the tested chemicals for developmental toxicology (Chapter 2, Part I). *This number comprises also enantiomers of azoles

Chemical Inventory for (re)myelination
Seven different azoles, approved for clinical use in skin infections and disorders (ketoconazole, isavuconazole voriconazole, posaconazole, fluconazole, itraconazole, miconazole) were selected with the aim of investigating their ability to induce the local increase of retinoic acid (RA) concentration, assumed to be responsible for the (re)myelinating effects observed in specific experimental models (Najm *et al.*, 2015). The 3D structures of the selected antifungal azoles were obtained from the PubChem compound repository and subsequently verified and optimized through an energy minimization procedure carried out with the MOE Builder module. The stereochemistry of these structures was then analysed and, when necessary, the stereoisomers were generated. At the end of this procedure, 39 structures of azoles were considered for molecular docking.
The database composition is listed in Table 20.

Chemical Category		No. of Chemical Substances
Azoles	**Diazoles**	6*
	Triazoles	33*
Non-azole	**Substrate**	1

Table 20: Summary of the tested chemicals for (re)myelination (Chapter 2, Part V). *These numbers comprise also enantiomers of azoles.

3D protein structures - General

Human nuclear receptors
The human LBD crystallographic structures of selected nuclear receptors were downloaded from the RCSB Protein Data Bank (http://www.rcsb.org), except for AHR whose 3D structure has not been experimentally solved yet. Each crystallographic structure was selected with a co-crystalized agonist ligand, in order to choose only the templates with the 12th α-helix in closed conformation. In fact, as suggested by Ng *et al* (Ng *et al.*, 2014) for ERα, choosing a crystal structure in closed conformation permits to preliminarily discriminate between agonist and antagonist. Some antagonists have a bigger molecular size than agonists and this implies that they will have atom clashes in docking calculation, with unacceptable values of binding free energy.
Moreover, among all the solved structures of each receptor, the one with both the best resolution and the lowest number of crystallographic non-solved amino acids was selected. 3D structures were then

verified and structurally prepared using MOE Structure Preparation Module, in order to correct crystallography-related errors and/or to fill up any unresolved residues. These crystallographic structures were then energy minimized down to a Root Mean Square (RMS) gradient of 0.05 kcal/mol/Å^2 using the Molecular Operating Environment (MOE) software. Amber10:EHT with the reaction field solvation model was set as force field for the structures preparation step. PDB ID of selected templates are reported in Table 21.

NR	PDB ID	Resolution [Å]	References
AR	2AM9	1.6	10.1110/ps.051905906
PR	1ZUC	2.0	10.1074/jbc.M504144200
ERα	3UUD	1.6	10.1073/pnas.1203574109
ERβ	3OLS	2.2	10.1002/cbic.201000532
CAR	1XV9.B	2.7	10.1016/j.molcel.2004.11.042
FXR	3RUT	3.0	10.1016/j.bmcl.2011.08.034
GR	1P93	2.7	10.1074/jbc.M212711200
LXRα	3IPU	2.4	10.1016/j.jmb.2010.04.005
LXRβ	1PQ6	2.4	10.1074/jbc.M304842200
PPARα	4BCR	2.5	10.1016/j.jmb.2013.05.010
PPARδ	3SP9	2.3	10.1074/jbc.M111.266023
PPARγ	3NOA	1.9	To be published
PXR	1M13	2.2	To be published
RARα	3KMR	1.8	10.1038/nsmb.1855
RARβ	4JYG	2.4	10.1371/journal.pone.0123195
RARγ	1FCX	1.5	10.1006/jmbi.2000.4032
RXRα	1XV9.A	2.7	10.1016/j.molcel.2004.11.042
RXRβ	1UHL	2.9	10.1093/emboj/cdg456
RXRγ	2GL8	2.4	To be published

Table 21. PDB code, resolution and references for each NR

To obtain the AHR LBD model, crystal structure of human hypoxia-inducible factor α (HIF-2α) (PDB ID:1P97 (Wu *et al*. 2013)) in *apo*- form was set as template. The alignment produced by the Clustal Omega (http://www.ebi.ac.uk/Tools/msa/clustalo/) software was manually checked using the MOE Alignment module. Comparative model building was carried out with the MOE Homology Model program with default settings. Ten independent models were built and refined, then the highest scoring intermediate model - according to the electrostatic solvation energy calculated using a Generalized Born/Volume Integral (GB/VI) methodology (Labute, 2008) - was submitted to a further round of energy minimization.

CYP26 isoenzymes

Since no structures are yet available at an atomistic resolution for CYP26, a model of each CYP26 isoenzyme (CYP26A1, CYP26B1 and CYP26C1) was built by comparative modelling for each species (human, rat, zebrafish).

The search for suitable templates was performed through the BLAST server (https://blast.ncbi.nlm.nih.gov/Blast.cgi), using as queries the primary structures of the three rat CYP26 isoforms: CYP26A1 [UniProt: G3V861], CYP26B1 [G3V7X8] and CYP26C1 [D4AAL3].

The crystallographic structure of the retinoic acid-bound cyanobacterial Cyp120a1 cytochrome (PDB ID: 2VE3) was identified as the most suitable template for all three isoforms in the PDB database (https://www.rcsb.org/pdb/home/home.do), with a sequence identity of approx. 30% for all the queries. Since the identity between CYP26 primary structures and the identified template was not high enough to ensure the generation of an accurate model, in order to achieve a thorough comparative modelling procedure, we developed an in-house substitution matrix from the alignment of 1,752 Cyp450 sequences. Only the annotated entries of the cytochrome P450 (Cyp450) family of the UniProt database (http://www.uniprot.org/) were selected and aligned by BLAST. In detail, we first considered the whole multiple-sequence alignment as a unique block and calculated the score

associated to each substitution as a measure of its evolutionary likelihood, in the same way as for the BLOSUM scoring matrices (Henikoff & Henikoff 1992).
The generated Cyp450-custom substitution matrix was then used to align the query CYP26 sequences to the selected template with a Python implementation of the Needleman-Wunsch pairwise alignment algorithm (Needleman & Wunsch, 1970), a gap opening penalty of -11 and an extension penalty of -2 per residue. Comparative modelling procedure was carried out by MOE with its default settings. Briefly, ten independent models were built and refined for each CYP26s and then the top-scoring intermediate models - according to the electrostatic solvation energy calculated using a Generalized Born/Volume Integral (GB/VI) methodology - were selected for each isoenzyme, refined and carefully inspected. Also the heme group, present in all the CYP450 isoenzymes and RA were considered in the CYP26 model generation.
The Amber10::ETH force field was used for all computational procedures.
For all the three generated models, the final quality was carefully checked, in order to make sure that the geometry (backbone bond lengths, angles and dihedrals), the sidechain rotamer quality and packing, the non-bonded contact quality, and the stereo-chemical quality of the generated structure were acceptable. In fact, from the analysis of the Ramachandran plot, only one outlier was found for CYP26A1 and CYP26B1, while two outliers were found for CYP26C1. However, they were located in loops distant from the binding site.
The same procedure was also applied to human CYP26 isoenzymes: CYP26A1 [O43174], CYP26B1 [Q9NR63] and CYP26C1 [Q6V0L0]; and to zebrafish CYP26 isoenzymes: CYP26A1 [P79739], CYP26B1 [Q6EIG3] and CYP26C1 [A1L1M2]. Also for human and zebrafish CYP26s, the crystallographic structure of the retinoic acid-bound cyanobacterial Cyp120a1 (PDB ID: 2VE3) was identified as the most suitable template, on the basis of sequence similarity. All the comparative modelling procedures were computed as previously described.

Identification of binding sites
The binding site of each receptor/enzyme was identified through the MOE Site Finder program, which uses a geometric approach to calculate putative binding sites in a protein, starting from its three-dimensional structure. This method is based on alpha spheres, which are a generalization of convex hulls. The prediction of the binding sites, performed by the MOE Site Finder module, confirmed the binding sites defined by the co-crystallized ligands in the *holo*-forms of the investigated proteins, except for AHR, which is in its *apo*- form. For this protein, a set of alpha spheres was selected according to Bisson *et al* (Bisson *et al*. 2009), that define the binding site for AHR PAS-B domain.

In silico molecular docking - General

In silico molecular docking was carried out with the MOE Dock tool. The same procedure was applied for each NR and CYP26 isoenzyme. 'Triangle Matcher' was selected as placement methodology, in which the poses are generated by superposing triplets of ligand atoms on triplets of receptor site points, which are alpha spheres centres representing locations of tight packing.
Three hundred complexes were generated for each tested ligand, removing the duplicate poses if the same set of ligand-receptor atom pairs is involved in both hydrogen bond and hydrophobic interactions. Then, putative poses were scored according to the following London dG scoring empirical function, to estimate the binding free energy of the ligand from a given pose:

$$\Delta G = c + E_{flex} + \sum_{h-bonds} c_{HB} \cdot f_{HB} + \sum_{m-lig} c_M \cdot f_M \sum_{atoms-i} \Delta D_i$$

where c represents the average gain/loss of rotational and translational entropy; E_{flex} is the energy expected for the loss of ligand flexibility; f_{HB} is a binary value measuring geometric imperfections due

to hydrogen bonds; c_{HB} is the energy owned by an ideal hydrogen bond; f_M is a binary value measuring geometric imperfections due to metal ligation; c_M is the energy owned by an ideal metal ligation; D_i is the desolvation energy of atom *i*. The difference in desolvation energies is calculated according to the following equation:

$$\Delta D_i = c_i R_i^3 \left\{ \iiint_{u \notin A \cup B} |u|^{-6} du - \iiint_{u \notin B} |u|^{-6} du \right\}$$

where *A* and *B* are the protein and/or ligand volumes; R_i is the solvation radius of atom *i*; C_i is the desolvation coefficient of atom *i* and both triple integrals are approximated using Generalized Born integral formulas.
A refinement step was applied to all the kept poses, basing on molecular mechanics in which all receptor atoms were held fixed during this step and the solvation effects were calculated using the reaction field functional form for the electrostatic energy term. Then, the GBVI/WSA dG scoring function with the Generalized Born solvation model (GBVI) (Wojciechowski & Lesyng, 2004) was used to evaluate the final energy (docking score) of ligand::protein complexes. In detail, the force field-based scoring function GBVI/WSA dG, which estimates the free energy of binding of the ligand from a given pose, is formalized by the following equation:

$$\Delta G \approx c + \alpha \cdot \left[\frac{2}{3} \left(\Delta E_{coul} + \Delta E_{sol} \right) + \Delta E_{vdw} + \beta \cdot \Delta SA_{weighted} \right]$$

where *c* represents the average gain/loss of rotational and translational entropy and both α and β are force field-dependent constants; E_{coul} describes the coulombic electrostatic term; E_{sol} is the solvation electrostatic term; E_{vdw} quantifies the van del Waals contribution to binding; $SA_{weighted}$ is the surface area weighted by exposure. At the end of refinement step, 50 final poses for each ligand::protein were kept. All ligands of the molecular database were tested according to the above procedure using Amber10:EHT as force field in all the computational procedures. Moreover, entries of the developmental toxicology were also submitted to a further refinement step, using MOE QuickPrep module in order to compute solvation contribute for a deepest analysis. With this procedure, ligand and residues within 4.5 Å were left free to move during minimization step, computing both affinity and solvation values.
The dissociation constant (K_i) was computed starting from empirical binding free energy values, according to the following equation:

$$\Delta G = RT \ln(K_i)$$

where R represents the gas constant and T the temperature. K_i was computed starting from the binding free energy values at a fixed temperature (300 K).

Chapter 1 – Part I

All the *in silico* calculations were carried out both in UMIL and FERA laboratories by Dr. Luca Palazzolo, Dr. Jane Cotteril and co-author of the already published paper (Cotteril and Palazzolo et al., 2019) and here reported to clarify the materials and methods. This research was funded by European Commission, in the EuroMix Horizon2020 Project.

(Q)SAR models

Details of the models used are shown below and a summary of the type of ER activity estimated by the models is shown in Table 1. The input for the models was an .sdf file of the test set compounds.

COSMOS Nuclear Receptor model

The COSMOS project (www.cosmostox.eu) Nuclear Receptor model implemented into KNIME workflows are available in the COSMOS KNIME WebPortal. Although primarily developed to identify potential binding to NRs important in hepatosteatosis, ER receptors are included in the model, which was developed using structural and physico-chemical features of NR ligands using data from ChEMBL and the Protein Data Bank (PDB). A total of 1489 ER agonists were identified and used in the workflow. Further details of the methodology of the workflow are available (Mellor *et al*., 2016).

DEREK Nexus Endocrine alerts

DEREK Nexus is a rule-based expert system where Structural Alerts for a particular endpoint identify important structural fragments within molecules that are associated with a specific toxicological effect (http://www.lhasalimited.org/products/derek-nexus.htm). If a compound contains a structural alert then the likelihood that the compound will cause toxicity is provided (based on the species and other rules such as bioavailability). If no Structural Alert is fired then DEREK returns "Nothing to Report". This does not necessarily mean a negative result, just that that the compound contains none of the structural fragments built into the rule-based system. Derek Nexus 5.01 contains 9 alerts for Oestrogen receptor modulation and 2 alerts for estrogenicity. Presence of these alerts is for our purposes interpreted as a substance being an ER binder, and absence of any of the alerts is interpreted as being a non-binder.

OCHEM estrogen receptor alpha agonists qualitative model

QSAR modelling efforts in the Tox21 Data Challenge 2014 ("TOX 21," 2014) resulted in a number of models for ER receptor binding, which were implemented in the online chemical modelling environment (OCHEM, http://ochem.eu). These include two ER-α agonist models using two different cell lines and a third model developed using log RBA data (Abdelaziz *et al*., 2016). For the purposes of this study only one model was used (Consensus Estrogen receptor α agonists qualitative), as the other Estrogen receptor agonist and RBA model estimates for the test set used in this study were found to be highly correlated. Other OCHEM models for ER agonists were available, but again as these are similar to the VEGA CERAPP model (2.1.7) they were not included in the study model selection.

OECD QSAR Toolbox DART scheme

DART (Developmental And Reproductive Toxicity) is a decision tree developed on the basis of the combination of known modes of action (MoA) and associated structural features, as well as an empirical association of structural fragments within molecules of reproductive or developmental toxic chemicals when MoA information was lacking. The decision tree is based on a detailed review of 716 chemicals (664 positive, 16 negative, 36 with insufficient data) that have DART end-point data and are grouped into defined receptor binding and chemical domains. When tested against a group of chemicals not included in the training set, the decision tree is shown to identify a high percentage of chemicals with known DART effects (Wu *et al*., 2013). The DART scheme is incorporated into the OECD (Q)SAR Toolbox (http://www.oecd.org/chemicalsafety/risk-assessment/theoecdqsartoolbox.htm). For the purposes of this study a positive score was assigned if a DART alert was present and the alert specifically mentioned ER binding.

OECD QSAR Toolbox ER profilers

There are two profilers related to ER binding freely available in the OECD (Q)SAR Application Toolbox software.

a) ER binding alert
The incorporated Toolbox ER binding profiling scheme is based on structural and parametric rules extracted from literature sources and supported by experimental data (Hamblen *et al*., 2003, Saliner *et al*., 2003, Schultz *et al*., 2002). The ER-binding profiler classifies chemicals as non-binders or weak, moderate, strong or very strong binders depending on molecular weight (MW) and structural characteristics of the chemicals. The performance of this profiler was evaluated by Mombelli (2012) using large human and rat binding datasets and the majority of compounds were correctly predicted. For the purposes of the present study chemicals were classed as positive if they had any alert for ER-binding (weak, moderate, strong or very strong).
b) rtER alert
The rtER Expert System v1, USEPA Estrogen Receptor Expert System (ERES) Profiler is an effects-based automated system used to predict estrogen receptor binding affinity, based on rainbow trout ER (rtER) (Hornung *et al*., 2014; Schmieder *et al*., 2014). It was specially designed to prioritise pesticides (inert and antimicrobial) that do not include any steroidal structures and thus are not capable of higher affinity ER interactions. The ERES is a logic rule-based decision tree that encodes the experts' mechanistic understanding with respect to both the chemical and biological aspects of the well-defined endpoint, or the ER bioassay domain.

VEGA Estrogen RBA model (IRFMN) – v.1.0.1
This classification QSAR model for binding to human estrogen receptor alpha (hER-α) was developed using experimental values for relative binding affinity (RBA), with 17β-estradiol as reference (Roncaglioni *et al*., 2008). This model is incorporated into the VEGA *in silico* platform, which is freely available online at http://www.vega-qsar.eu/ (the version used for this study was 1.1.3).

VEGA Estrogen Receptor-mediated effect (IRFMN/CERAPP) - v.1.0.0
This Structural alert rules-based model was built using Sarpy software using a large dataset of high-quality ER signalling data (1529 chemicals screened across 18 high-throughput screening assays integrated into a single score), from the ToxCast program (Judson *et al*., 2014). The model was developed within the framework of the Collaborative Estrogen Receptor Activity Prediction Project (CERAPP), Mansouri *et al*., 2016.

(Q)SAR Model	ER-related endpoints considered	Access to models
COSMOS Nuclear Receptor model	ER-agonists	Freely available
DEREK Nexus	Various endpoints related to ER activity	License fee
OCHEM estrogen receptor alpha agonists	ER- α agonists	Freely available
OECD QSAR Toolbox DART scheme (ER binding)	Various endpoints related to ER binding	Freely available
OECD QSAR Toolbox alerts (ER binding alert)	Various endpoints related to ER binding	Freely available
OECD QSAR Toolbox alerts (rtER alert)	Various endpoints related to ER binding,	Freely available
VEGA – RBA	Relative Binding Affinity, hER- α	Freely available
VEGA - CERAPP	Various endpoints related to ER signalling	Freely available

Table 22. ER activity estimated by the (Q)SAR models

Applicability Domain
The (Q)SAR models considered in this study are in general applicable only for small organic molecules; inorganic compounds, organo-metallic and polymeric structures are outside of the domain of the models. The QSAR models available in the VEGA platform have a built-in tool to measure the reliability of the prediction through the applicability domain index, based on similarity to molecules in the training set, accuracy of prediction of similar molecules, concordance for similar molecules, errors of prediction among similar molecules, model's descriptor range check and atom centered

fragments similarity checks. For the purposes of this study, estimates of low reliability were not considered in the majority consensus. For the other models considered in the study based on Structural Alerts, training sets are often not readily available and the domain thus difficult to define. Although the lack of an alert thus does not necessarily mean a negative estimation, the presence of these alerts is for our purposes interpreted as a substance being an ER binder, and absence of any of the alerts is interpreted as being a non-binder. Some compounds, for example Organophosphorus compounds, are not covered by the version of the DART scheme used in the study and so are outside the applicability domain of this model.

Majority Consensus

The model outputs were collated and a score of 1 assigned to positively predicted compounds and a score of 0 assigned to negatively predicted compounds. Where no estimate was obtained from a model, if it was outside the applicability domain of the model, or the compound was in the training set of the model and so its estimate excluded from the analysis, N/A was assigned. The total score of each compound (i.e. the number of models with a positive prediction) was divided by the total number of models producing an estimate. Where this was greater than or equal to 0.5 a positive estimate was assigned and where less than 0.5 a negative estimate was assigned.

Selection of the validation set

As the various models to predict ER-binding cover a range of activities, for example some of the (Q)SAR models and the standard molecular docking procedure do not distinguish between agonists and antagonists, a validation set which isn't specific for agonists or antagonists was required. The validation set selected contained Relative Binding Affinity (RBA) data for the ERα receptor and is the external validation set used to test the VEGA RBA model (Roncaglioni *et al*., 2008). It is a diverse dataset of compounds, including natural and synthetic steroids, drugs and chemical contaminants such as pesticides, PCBs and phthalates, originally obtained from the Japanese METI database (METI 2002). The validation set was selected on the basis of it containing RBA data for a heterogeneous group of compounds, its previous use as a validation set (Roncaglioni *et al*., 2008), data for all of the compounds also being available from reporter gene assay and it containing not too large a number of compounds to enable molecular docking to be also carried out for all of the compounds within the time constraints of the project. The validation set was downloaded as a text file from VEGA version 1.1.3 (from the dataset of 806 compounds, the 150 compounds labelled with TEST status were selected) and then converted to an .sdf file for input to the various models. Details of how the chemical structures were originally obtained and modified for use in QSAR modelling are available in Roncaglioni *et al*. (2008). Two compounds containing tin were removed for this study as these metallo-organic compounds are not predicted in several models, leaving 148 compounds of which 52 were active and 96 were inactive for ERα receptor binding.

Evaluation of predictive performance where the validation set compounds were actually used to build the suite of (Q)SAR models and therefore would lead to overestimation of the accuracy of the models is to be avoided. Therefore, where the training sets for models are known, any compounds in the validation set which were used to build models were removed. For the VEGA CERAPP model, 50 of the 148 compounds were used to build the model, so these were removed leaving 98 validation compounds (38 active, 60 inactive) for this model. For the OCHEM ER agonist model 68 of the 148 compounds were used to build the model, so these were removed leaving 82 validation compounds (35 active, 47 inactive) for this model. The training sets for the other models considered in the study were not available.

Reporter gene (RA) assay experimental data for the validation set were also obtained (Roncaglioni *et al*., 2008) in order to use alongside RBA results with a view to identify if compounds may be antagonists.

Cooper statistics

In order to compare the individual (Q)SAR models, the molecular docking prioritization (Trisciuzzi *et al*., 2017) and majority consensus predictions, the standard Cooper statistics (Cooper *et al*., 1979) and Matthews correlation coefficient (Matthews, 1975) were used to assess the quality of the predictions. Sensitivity is defined as the percentage of correctly classified positive predictions among the total number of positive instances. Specificity is the percentage of correct negative predictions compared to the total number of negatives. Accuracy is defined as the total number both positive and negatives correctly predicted among the total number of compounds. MCC (Matthews correlation coefficient) is a weighted value that overcomes any imbalance in the data classes which might lead to over-optimistic values of accuracy. The so-called Negative Predictive Value (NPV) was also computed for the (Q)SAR and molecular docking results to evaluate the goodness of the classification and, in particular, to represent the probability that a chemical predicted as a non-binder (under-threshold) is actually a non-binder (Trisciuzzi *et al*., 2005, 2017).

Methods for molecular docking (details)

Among all the solved structures of estrogen receptor alpha LBD in complex with estradiol, the one with both good resolution and the lowest number of crystallographic non-solved amino acids was retrieved from the RCSB Protein Data Bank [PDB entry: 3UUD.A] (Delfosse *et al*., 2012). 3D structures were then verified and structurally prepared using MOE Structure Preparation Module, in order to correct crystallography-related errors, adding hydrogens and/or to fill up any unresolved residues. The 3D structure was then submitted to an energy minimization step with the Amber10:EHT force field and the reaction field solvation model. Refinement was carried out down to a Root Mean Square (RMS) gradient of 0.05 kcal/mol/A ˚2.

For each chemical, stereochemistry was carefully checked according to those reported in PubChem, the dominant protomer/tautomer and protonation state was computed at physiological pH for each chemical. Twenty thousand rotamers were also generated for each chemical.

In silico molecular docking was carried out with the MOE Dock Program. 'Triangle Matcher' was selected as placement methodology, in which the substance poses are generated by superposing triplets of ligand atoms on triplets of receptor site points, which are alpha spheres centres representing locations of tight packing.

Thirty complexes were generated for each tested ligand, removing the duplicate poses if the same set of ligand-receptor atom pairs is involved in both hydrogen bond and hydrophobic interactions. Then, putative poses were scored according to the London dG scoring empirical function, to estimate the binding free energy of the ligand from a given pose.

A refinement step was then applied to all the kept poses, basing on molecular mechanics in which all receptor atoms were held fixed during this step and the solvation effects were calculated using the reaction field functional form for the electrostatic energy term. Then, the GBVI/WSA dG scoring function with the Generalized Born solvation model (GBVI) (Wojciechowski and Lesyng, 2004) was used to evaluate the final energy (docking score) of ligand::protein complexes.

To verify the robustness of the molecular docking approach on ERα, the binding pose of the 3UUD co-crystallized estradiol was computed, obtaining a perfect overlapping (RMSD lower than 0.3 Å) (Galli *et al*., 2014). Moreover, with the aim of detecting the best cut-off energy values for a toxicological evaluation, i.e. whether a compound could be classed as an ER-binder or ER-non-binder, Cooper statistics were applied. To better visualize the docking behaviour, the Receiver Operating Characteristic (ROC) curves were used to graphically compare docking performances, for a range of different cut-off values.

Low-Mode Molecular Dynamics simulations (LM-MD)

To study the flexibility of α-helix 12 of NR LBD due to ligand activity, LM-MD simulation is a very efficient way to reproduce the low-mode vibrations with respect to classical molecular dynamics for minima troughs on the potential energy surface. To run these computations, MOE Conformational Search program was used, estimating the low-frequency modes through an efficient implicit method,

based on the attenuation of high-range velocities as described in detail in Labute *et al*., 2010. The human ERα LBD bound to

i) a well-known full-agonist (17β-estradiol),
ii) a well-known antagonist (4-hydroxytamoxifen),
iii) selected chemicals and
iv) in its apo- form were simulated after the MOE QuickPrep preparation.

(i) ERα ::17β-estradiol complex was obtained from the above mentioned structure preparation procedure; (iv) the apo- form, the protein moiety of a molecular complex, was obtained from the same PDB, by removing the endogenous hormone *in silico*; (ii) the complex with antagonist was obtained superimposing RCSB PDB 3ERT (Shiau *et al*., 1998) and RCSB PDB 3UUD crystal structures and then importing the coordinates of co-crystalized antagonist 4-hydroxytamoxifen from 3ERT to 3UUD in apo- form.

Complexes with selected chemicals were obtained with the following procedure: ERα::Ligand complexes resulting from docking procedures were superimposed to 3UUD bound to both full-agonist (i) and antagonist (ii); proteins were removed and two Flex-Alignments for putative agonist/antagonist were performed keeping hold of the endogenous hormone or antagonist, respectively; complexes with selected ligands were rebuilt using the coordinates of the apo-3UUD 3D structure.

Both helix 12 (set as a rigid body) and the loop joining helix 12 to the preceding helix were left free to move during the low-mode molecular dynamics, whereas the residues more than 4.5 Å away were fixed (not free to move but used for the energy calculations); the other residues were defined as inert (fixed and not used for energy calculations). The simulation was carried out with default parameters, except for strain energy cut-off, which was set at 200 kcal/mol. Hundred conformations were generated and analysed. The Amber10:EHT force field was used for all the computational procedures. In order to classify the tested chemicals as agonist, partial agonist or antagonist, the Root Mean Square Deviation (RMSD) values of helix 12 alpha carbons was computed between 3UUD crystal structure and simulated complex.

Chapter 2 – Part I, ligand-based approach

To study the electronic transitions between the heme of CYP26s and the site of metabolism (SOM) of selected compounds, the following steps were followed:

i) for each compound belonging to the azoles database, three SOMs were predicted using SMARTCyp (Rydberg *et al*., 2010), a *.svl* MOE module, that rate atoms basing on specific chemical-physical and geometric descriptors for CYP P450;
ii) basing on docking score, selected on the basis of binding free energy and on some geometric constraints between SOM and the Fe atom of heme (Li *et al*., 2012), structures for Transition State Theory (TST) were built;
iii) from these structures, reaction energies were computed applying single point energy calculation *via* DFT (Rydberg *et al*., 2014; Rydberg *et al*., 2009; Rajakumar & Arunan, 2003).

Both HEME and selected pose of each ligand were imported into Schrodinger (https://www.schrodinger.com/maestro). HEME was then replaced by a carboxyl as recommended by Li *et al* (Li *et al*., 2012), in order to speed up the DFT and TST calculations.

Starting from these modified structures, the reaction products for each compound was drawn, while transition states were drawn by positioning the carboxyl group closest to the SOM. 6-31G** was used as basis set for all the computational procedures (Rydberg *et al*., 2014; Rajakumar & Arunan, 2003).

Chapter 2 – Part III, PD ODE system

RA and single azoles

All the *in vitro* tests were carried out in UMIL laboratories by Prof. Elena Menegola research group and published in Battistoni *et al*. Here we report the extracted data, while for experimental procedures, please, see Materials and Methods in Battistoni *et al*. In the following tables, *n* is the total number of tested embryos, while *r* represents the number of malformed embryos. In Tables 23, 24, 25, 26 are reported concentrations of single azoles/RA, while in Tables 27, 28, 29 are reported concentrations of azoles in mixtures.

RA concentrations (nM)	n	r
0	22	0
25	23	2
50	16	11
125	19	19

Table 23: Retinoic acid concentrations and malformed embryos

Cyproconazole concentrations (nM)	n	r
0.0	9	0
7.8	14	4
15.0	9	8
31.5	7	7
250.0	3	3

Table 24: Cyproconazole concentrations and malformed embryos

Triadimefon concentrations (nM)	n	r
0.00	22	0
6.25	8	0
12.50	11	3
25.00	8	8
50.00	7	7

Table 25: Triadimefon concentrations and malformed embryos

Flusilazole concentrations (nM)	n	r
0.0000	18	0
1.5625	10	0
3.1250	11	5
6.2500	9	9
9.3750	5	5

Table 26: Flusilazole concentrations and malformed embryos

Mixtures

Triadimefon concentration (nM)	n	r
0.00	11	5
6.25	10	10
12.50	12	11
25.00	8	8
50.00	7	7

Table 27: Triadimefon and flusilazole (3.125 nM) concentrations and malformed embryos

Flusilazole concentration (nM)	n	r
0.000	11	3
1.560	7	4
3.125	12	11
6.250	6	6
9.375	6	6

Table 28: Flusilazole and triadimefon (12.5 nM) concentrations and malformed embryos

Cyproconazole concentration (nM)	n	r
0.0	12	5
7.8	11	9
15.0	3	3

Table 29: Cyproconazole and triadimefon (7.8 nM) concentrations and malformed embryos

ODE System

To capture the RA kinetics, we formalized the following set of differential equations. In the equations, the five variables of the system, ADH, RA, CYP26_mRNA, CYP26 and FGF represent intracellular concentrations. Only CYP26A1 was considered because of its inducted expression is the only one expression that is well characterized. The embryo was considered as a point in space, representative of the half of the normalized embryo hindbrain length. This effect is active only in RA equation, in the ADH term, and in FGF equation that are the only two variables that in embryo create a spatial gradient.

The ADH equation consists in three term, a synthesis of ADH protein, a degradation that depends on ADH concentration and a transcription term, mediated by ethanol (17 mM). The latter is positive and increases the ADH concentration.
The FGF equation is composed by only two terms and, in our simulation, it is no affected by system perturbations inducted by azoles. This equation contains a synthesis and a degradation term, the latter depending on FGF concentration.
The CYP26 mRNA term, on the other hand, is composed, by three terms: synthesis, degradation and an induction term, in which both RA and FGF concentrations mediate the effects, through a cooperative Hill expression.
The equation of CYP26 is very similar to FGF, but the synthesis term depends on CYP26 mRNA equation.
RA equation is pivotal in our ODE system, and in the following lines it will be discussed term by term in more detail. The equation has the first term that represents the production rate by ADH, depending on Retinol concentration, that is fixed in time, and the second term that represents the physiological rate of RA elimination. The third term implemented in this ODE system describes the interactions between RA and azoles, depending on CYP. In this term, we consider all the azoles contribution to CYP26 inhibition, weighted by RA. All the respective *in silico* Ki were considered in the Hill terms.

From a biological point of view, the following scenario is described: Ethanol increases ADH concentration, ADH increases with time RA concentration that, as primary feedback, increases Cyp mRNA. Cyp mRNA progressively increases CYP26 concentration that, as secondary feedback, decreases RA concentration.

```
dt (ADH) = k_syn_ADH - k_deg_ADH * ADH + k_trs_ADH_by_ETH * ETH;

 dt (RA) = k_trs_RA_by_ADH * ADH * ( RO / ( k_i_RO + RO))*0.5 - k_deg_RA * RA - CYP26 *
        (
        km_RA  * RA -
        km_FLUCO * ((FLUCO/(ki_FLUCO + FLUCO))    / ( RA / (ki_RA + RA)) ) * FLUCO -
        km_FON * ((FON/(ki_FON + FON))          / ( RA / (ki_RA + RA)) ) * FON -
        km_CYPRO * ((CYPRO/(ki_CYPRO + CYPRO))    / ( RA / (ki_RA + RA)) ) * CYPRO -
        km_FLUSI * ((FLUSI/(ki_FLUSI + FLUSI))    / ( RA / (ki_RA + RA)) ) * FLUSI -
        km_ETH  * ( (ETH/(ki_ETH + ETH))        / ( RA / (ki_RA + RA)) )  * ETH
        );
```

```
dt (CYP26_mRNA) = k_trs_CYP26_base +
                  vmax_trs_CYP26_by_RA *
                  (pow(RA, 2) / (pow(k_act_CYP26_by_RA, 2) + pow(RA, 2))) *
                 ((pow(FGF, 2) / (pow(k_inh_CYP26_by_FGF, 2) + pow(FGF, 2)))) -
                  k_deg_CYP26_mRNA * CYP26_mRNA;

dt (CYP26) = k_trd_CYP26 * CYP26_mRNA - k_deg_CYP26 * CYP26;

dt (FGF) = k_syn_FGF * 0.5 - k_deg_FGF * FGF;
```

As output of the ODE system, here reported from MCSim software imput, we extracted the RA concentration at 48 h, in order to simulate embryo conditions and then, basing on this information, we computed the malformations probability using the logit function.

To simulate the equilibrium concentration of RA, CYP26 mRNA, CYP26, ADH and FGF, at different times, the ODE system was solved by numerical integration. With this approach we studied the stable concentrations of variables. In the first run, all the concentrations were set to 0.1 nM as suggested in Goldbeter *et al*. and in Battistoni *et al*. ODE parameters were also extracted from literature, as for the RA baseline and the total amount of ADH, that is compliant with our equilibrated RA gradient concentration. The CYP26 inhibition constants by azoles were extracted from Chapter 2, Part II. The values of ODE constants are reported in the following tables.

Constant	Value	Info
km_RA	0.01667	1/(nM * min)
k_deg_RA	0	
k_trs_CYP26_base	0.00608333	0.365 nM/min
vmax_trs_CYP26_by_RA	0.118333	7.1 nM/min
k_act_CYP26_by_RA	7.083839	nM
k_deg_CYP26_mRNA	0.01667	1 min^-1
k_trd_CYP26	0.01667	1 min^-1
k_deg_CYP26	0.00466667	0.28 min^-1
k_syn_FGF	0.083333	min^-1
k_deg_FGF	0.016667	1 min^-1
ADH	7.1	nM
k_inh_CYP26_by_FGF	1	
RO	150	nM Horton and Maden 1995 ,ÄúRO is 5 fold excess
k_syn_ADH	0.01666667	equal to k_syn_RA
k_deg_ADH	0.00234742	Fitted in "setting_ADH"
k_i_RO	49	nM Chase *et al*. 2009
k_trs_RA_by_ADH	3.61022	fitted parameter with MatLab for RA = 26 nM
k_i_ETH_ADH	36	mM Chase *et al*. 2009
baseline_RA	26.327	RA baseline (nM)

Table 30: ODE parameters

Variable	Value	Unit
RA	26	nM*
CYP26_mRNA	4	nM
CYP26	14.28	nM

FGF	2.45	nM
ADH	7.1	nM*

Table 29: ODE initial variables

Q0, Q1, kinh_FLUSI, kinh_FON, and kinh_CYPRO free parameters were calibrated using a fitting strategy on data. Q0 and Q1 were fitted on RA, while azoles-specific constants were fitted on flusilazole, triadimefon and cyproconazole data, respectively. For each parameter, the fitting strategy is based on the Bayesian calibration, as suggested in Battistoni *et al*., assuming a binomial distribution with probability P, managed by the logit function. The priors were set to uninformative uniform distributions. Given the prior and the data, Markov-chain Monte Carlo (MCMC) simulations were performed. For each parameter, two MCMC chains were run in parallel for 10,000 iterations. The last 5,000 samples from each chain were kept for inference and predictive simulations. Convergence of the chains was assessed using Gelman and Rubin Rhat criterion. Convergence was achieved in all cases.

All model simulations and MCMC calibrations were performed with GNU MCSim version 6.0.1 (www.gnu.org/software/mcsim) through an R script (cran.r-project.org) and managed with Knitr extension in order to produce plots and to resume the simulation steps.
Calibration of initial conditions of variables were explored both *via* MATLAB and basing on literature.

Chapter 2 – Part IV, PBPK ODE system

Data for two tebuconazole enantiomers [R (-)- and S (+)-tebuconazole] in plasma, liver, brain, heart, kidney, fat, lung, muscle and spleen of male Japanese white rabbits were digitized form Zhu *et al* (2007). As first step, the two enantiomers were considered as the same chemical and data were aggregated.
The Open Systems Phrmacology Suite – PK-Sim (http://www.systems-biology.com/products/pk-sim.html) was used to build the ten compartment PBPK model (Scheme 1), using physiological rabbit data (e.g. tissue volume, regional blood flows) provided by the software for a Japanese white rabbit weighing 2.25 kg. Cardiac output was allometrically scaled to body weight using the following equation:

$$0.25 \times W\ (kg)^{0.74}\ L/min\ (Brown\ et\ al.\ 1997).$$

Relative blood weight was assumed to be 7.5% of body weight and plasma weight to be 50% of blood weight. Plasma:tissue tebuconazole partition coefficients and the liver clearance rate of tebuconazole were fitted to the data available. Tebuconazole chemical properties were calculated via MOE Molecular Descriptors suite. Administration route was set as 30 mg/kg body weight (bd wt) by intravenous (iv) injection, as reported in Zhu *et al*. (2007)
The time rate of the amount of tebuconazole (A_x) changes in a tissue x is given by the difference between the amount of the entering tebuconazole in the tissue through arterial blood and the amount leaving the tissue through venous blood. The following differential equation describe the rate of change for brain, heart, kidney, spleen, muscle, fat and rest of body:

$$\frac{dA_x}{dt} = Q_x(C_{p,art} - C_x / P_x)$$

where Q_x is the tissue x regional blood flow, C_x is the tebuconazole concentration in tissue x, P_x is the tebuconazole tissue x:plasma partition coefficient and $C_{p,art}$ is the tebuconazole concentration in arterial

plasma. For lung the time rate of the amount of tebuconazole changes is described by the difference between the amount entering through venous blood and the amount leaving to the arterial blood pool:

$$\frac{dA_{lu}}{dt} = Q_c \cdot (C_{p,ven} - C_{lu} / P_{lu})$$

For the liver, two terms indicating liver clearance were added to the standard differential equation, as reported in the following equation

$$\frac{dA_{li}}{dt} = Q_{li}(C_{p,art} - C_{li} / P_{li}) + Q_{GI}(C_r / P_r - C_{li} / P_{li}) - CL_{li} \cdot C_{li} / P_{li};$$

while for the venous plasma changes, concentration is given by the difference between the amount entering the venous pool through venous blood from both the tissues *x* and liver, and the amount leaving the pool to lung:

$$\frac{dA_{p,ven}}{dt} = \sum_{\substack{x \neq \text{remaining} \\ \text{tissue}}} Q_x \cdot C_x / P_x + Q_{ss} \cdot C_r / P_r + (Q_{li} + Q_{GI}) \cdot C_{li} / P_{li} - Q_c \cdot C_{p,ven}$$

For arterial plasma the time rate of change of the amount of tebuconazole is given by the difference between the amount entering from the lung and the amount leaving to venous pool:

$$\frac{dA_{p,art}}{dt} = Q_c \cdot (C_{lu} / P_{lu} - C_{v,pla})$$

where Q_c is the cardiac output that is allometrically scaled to rabbit body weight as in Andersen *et al*. (2016). Data about the blood flow in rabbit were imported from rat (Brown *et al*. (1997), Table 23). Plasma:tissue tebuconazole partition coefficients and the liver clearance rate of tebuconazole were fitted to the data available.

To extrapolate the tebuconazole model from rabbit to human the same compartment and the same equation were maintained, scaling the coefficients according to Brown *et al*.

Parameters from Bosgra *et al*. were extrapolated to describe the organ volumes and regional blood flows. Tissue::plasma partition coefficient was determined from the rabbit data and scaled taking into account the human organ volumes. Liver clearance was allometrically scaled proportional to the ratio of human to rat body weights to the power 0.75 as in West *et al*., scaling the 0.052 L/min of the rabbit to the 44 L/h for a man of 73 kg.

The standard male body composition was extrapolated by Bosgra *et al*., assuming a man weighing 73 kg and a cardiac output of 390 L/h was assumed.

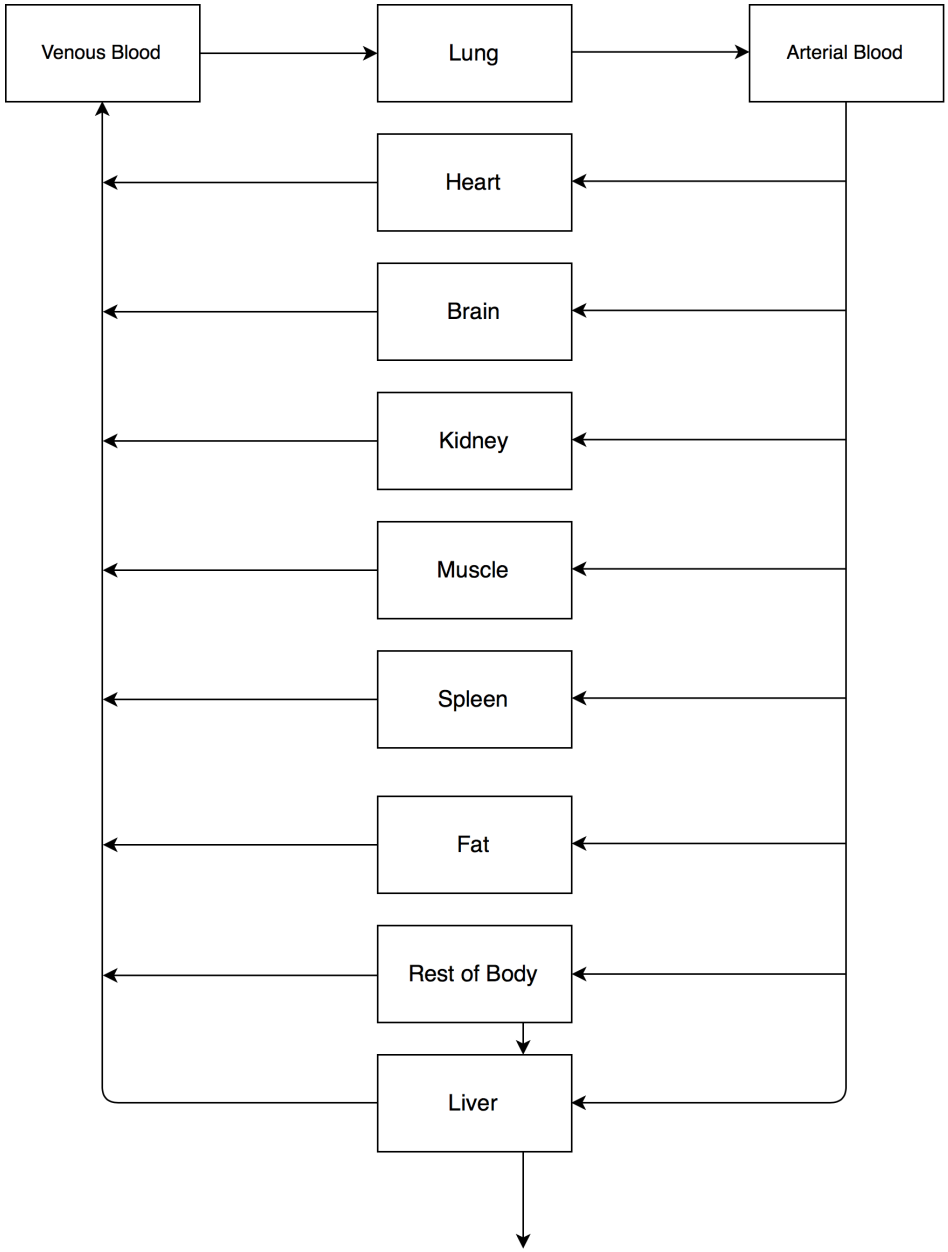

Figure 60: Proposed PBPK-model for tebuconazole in humans.

Chapter 2 – Part V, *In vitro* tests

All the *in vitro* experiments were carried out in UMIL laboratories by Dr. Chiara Parravicini in the FISM grant framework and here reported to clarify the *in vitro* procedures.

OPC cultures

OPCs were obtained from the cortex of P2 CD1 Sprague Dawley rats; after isolation, brain tissues were stored for 4 hours in MACS® Tissue Storage Solution before starting the digestion and dissociation protocol, following the manufacturer instructions to obtain a single-cell suspension (Miltenyi Biotec).
After enzymatic dissociation cells were counted and forwarded to the next purification step. Cells expressing A2B5 were isolated from single-cell suspension using the magnetic labelling of OPCs

specifically expressing A2B5 antigen via magnetic microbeads conjugated to monoclonal anti-A2B5 antibody.
After counting, purified cells were plated onto poly-D,L-ornithine-coated multi-wells (final concentration 50 μg/ml) to a density of 15,000 cells/well, and cultured in a proliferation medium. After 2-3 days, this medium was substituted with a differentiation medium lacking growth factors and in absence of the thyroid hormone T3. The next day, to analyse the effect of azoles in myelination, OPCs were exposed to selected azoles and RA with the following concentration, together with the control (exposed only to vehicle):

- RA (50 nM)
- RA (50 nM) + citral (150 μM),
- citral (150 μM)
- posaconazole (10 nM),
- posaconazole (10 nM), + citral (150 μM)
- itraconazole (10 nM)
- itraconazole (10 nM) + citral (150 μM)
- fluconazole (30 nM)
- fluconazole (30 nM) + citral (150 μM)

RA and citral concentration were set according to literature data (Menegola et al, 2016) while azole concentrations were established according to the pKi obtained from docking results as 30 nM for fluconazole, 10 nM for itraconazole and posaconazole, 50 nM for RA and 150 μM for citral.
After 48 hours, cells were fixed and stained with a standard immunocytochemical approach.

DRG-OPC co-cultures
DRG-OPC co-cultures were prepared according to the following protocol.
DRG from E14.5 mouse embryos were plucked off from spinal cord, put in culture (1 DRG/coverslip) in Neurobasal supplemented with B27 in the presence of 100 ng/ml NGF and cycled with 10 μM fluorodeoxyuridine to eliminate all non-neuronal cells. After 20 days, when neurites were well extended radially from DRG explants, 35,000 OPCs were added to each DRG in culture and kept in MEM supplemented with 4 g/L glucose, 10% FBS and 2 mM L-glutamine. Myelination was induced the following day by the addition of recombinant chimeric 1 μg/ml TrkA-Fc to the culture medium.
OPC/DRG co-cultures were exposed to the same mixtures as in the above OPC cultures protocol, with the exception of those containing posaconalzole which was deemed uneffective after OPC cultures results. The protocol is 12 day long: the treatments were carried out every 48/72 hours for five times, then after 48 hours cells were fixed and stained with a standard immunocytochemical approach.

Immunocytochemistry studies
To perform immunocytochemical studies, the cells were fixed according to the following procedure: the culture medium was aspirated and, to each well, paraformaldehyde plus 4% sucrose was added (500 μL for well). After incubation for 20 minutes at room temperature, the fixative was aspirated and three washes, 10 minutes each, were performed with PBS 1X (Phosphate Buffered Saline 0.1 M, EuroClone). Finally, up to the time of immunohistochemical analysis, the coverslips were stored in PBS sodium azide (500 μL per well) and the plates, sealed with parafilm, were stored at 4 ° C.

OPC protocol
The coverslips with the fixed cells were taken and transferred for staining to another appropriately labelled plate. After two quick washes in low salts (10 mM phosphate buffer and 150 mM NaCl) followed by two rapid washes in high salts (20 mM phosphate buffer and 50 0mM NaCl) to promote hydration of the fixed cells and to remove any impurities or debris, the coverslips were transferred to a wet room. Each coverslip was pre-treated with 45 μL of Goat Serum Diluition Buffer (GSDB; 450 mM NaCl, 20 mM sodium phosphate buffer, pH 7.4, 15% goat serum, 0.3% Triton X-100, Life

Technologies) for 15 minutes at room temperature in a humid chamber, in order to saturate the non-specific binding sites.
The primary antibodies, rabbit-anti-GPR17 (marker of differentiation) and rat-anti-MBP were diluted 1:50 and 1: 200 respectively in GSDB 1X and incubated (each slide on a 45 µL droplet) for 2 hours and 30 minutes in a humid chamber at room temperature or overnight (16 h) at 4 ° C. At the end of the incubation, the coverslips were subjected to 3 washes in high salts for a total of 30 minutes. The samples were then incubated with the secondary goat anti-rat/-rabbit antibodies conjugated to the fluorophores Alexa Flour 488 (green) and Alexa Flour 555 (red) (Life Technologies), diluted in 1:600 in GSDB 1X, for one hour in a humid chamber at room temperature.
Subsequently, two washes in high salts of 5 minutes were performed, then the nuclei were stained by incubating the cells with HOECSTH 33258 (Life Technologies), diluted 1:10,000 in high salts, for 20 minutes in the dark under a chemical hood. Finally, three washes in low salts for a total of 15 minutes and a final wash in 5 mM phosphate buffer aimed at removing any nonspecific signal determined by the link between the secondary antibody and various cellular proteins. At the end, the coverslips were mounted with the Dako Fluorescent Mounting Medium agent (Dako Glostrup, Germany) on object slides previously defatted with 70% ethanol and appropriately labelled.

DRG-OPC protocol
To prevent cross-link interaction of the primary antibodies used (rat and mouse) DRG-OPC were treated with a different protocol. The coverslips with the fixed cells were taken and transferred for staining to another appropriately labelled plate. After two quick washes in low salts followed by two rapid washes in high salts to promote hydration of the fixed cells and to remove any impurities or debris, the coverslips were transferred to a wet room. Each coverslip was pre-treated with 45 µL of Goat Serum Dilution Buffer for 15 minutes at room temperature in a humid chamber, in order to saturate the non-specific binding sites.
The first primary antibody rat-anti-MBP was diluted 1:600 in GSDB 1X and incubated (each slide on a 45 µL droplet) for 2 hours and 30 minutes in a humid chamber at room temperature or O/N (16 h) at 4 ° C. At the end of the incubation, the coverslips were subjected to 3 washes in high salts for a total of 30 minutes. The samples were then incubated with the secondary goat anti-rat antibodies conjugated to the fluorophores Alexa Flour 555 (red), diluted in 1:600 in GSDB 1X for one hour in a humid chamber at room temperature.
Three washes were carried out in high salts followed by three washes in low salts for a total of 30 minutes. Then, two rapid washes in high salts were performed followed by pre-treatment with 45 µL of GSDB for 15 minutes at room temperature in a humid chamber.
The second primary antibody is a mixture of mouse-anti-smi31 and mouse-anti-smi32, diluted 1:500 in GSDB 1X and incubated for 2 hours and 30 minutes in a humid chamber at room temperature or O/N (16 h) at 4 ° C. At the end of the incubation, the coverslips were subjected to 3 washes in high salts for a total of 30 minutes. The samples were then incubated with the secondary goat-anti-mouse antibodies conjugated to the fluorophores Alexa Flour 488 (green), diluted in 1:600 in GSDB 1X for one hour in a humid chamber at room temperature.
Subsequently, two washes in high salts of 5 minutes were performed, then the nuclei were stained by incubating the cells with HOECSTH 33258 (Life Technologies), diluted 1: 10,000 in high salts, for 20 minutes in the dark under a chemical hood. Finally, three washes in low salts for a total of 15 minutes and a final wash in 5 mM phosphate buffer aimed at removing any nonspecific signal determined by the link between the secondary antibody and various cellular proteins. At the end, the coverslips were mounted with the Dako Fluorescent Mounting Medium agent (Dako Glostrup, Germany) on object slides previously defatted with 70% ethanol and appropriately labelled.

Data analysis of OPC
To obtain a quantitative interpretation of the biological phenomena observed in the OPCs fixed and subjected to immunocytochemistry, a semiautomatic cell count protocol was developed using the

ImageJ program, a graphic processing program developed by Wayne Rasband at the Research Services Branch of the National Institute of Mental Health in Bethesda, Maryland, USA. The procedure is divided in three phases: acquisition of the cell fields to be counted, processing of the acquired images and the actual count.
Images were acquired using an AXIOVERT 200 M optical microscope (Zeiss, Milan), equipped with a UV lamp and an AXIOCAM HRM Zeiss camera. The initial processing was performed with the Axiovision 4.4 software on the computer connected to the microscope, respectively in the fluorescence channel of the fluorescein isothiocyanate (FITC), of the rhodamine (RHODAMINE) and of the 4 ', 6-diamidino-2-phenylindole (DAPI). Fields were acquired at a 20X magnification using the area framed by the microscope camera, along the horizontal diameter of the slide as a reference. For each slide all the diameter fields have been acquired.
The level of myelination is evaluated by counting the numbers of cells that express MBP (myelin basic protein) related to the number of nuclei as marked by HOECST. To enforce count consistency a stack of images was generated from the sequence of the acquired images; then balance of individual channels as well as contrast and brightness of the image were applied on the stack as a whole. The data obtained from the count were then tabulated and analysed.
Experimental data were fitted to a linear mixed effect model using the "lmer" function of the R library "lmerTest", using restricted maximum likelihood as convergence criterion type III analysis of variance with Satterthwaite's correction.
The formula used was:
MBP/HOECST ~ treatment + (1|experiment)
in which MBP/HOECST is the response variable while treatment the explanatory variable i.e. the "fixed effect". Since the experiment was repeated 3 times the variable exp was also considered as "random effect" to account for pseudoreplication. Initially it was considered also coverslip as source of pseudoreplication but it was later removed from the model since its contribution proved to be nonsignificant.

Data analysis of DRG-OPC
DRG-OPC coverslips were analysed under a confocal microscope (LSM510 META, Zeiss). The quantification of myelin segments was performed by the following protocol: 6 random fields of 4-5 coverslips for each experimental condition were acquired with the ZEISS LSM Image Browser. Stack images of MBP and smi31/smi32 positive cells were taken at 40X magnification; images in the stacks were merged at each level and pixels overlapping in the red and green fields above a predefined threshold intensity value were highlighted in white. The amount of myelin per axon (myelination index), was calculated as the ratio between the white pixels area and the green pixels area.
As above, to account for pseudo-replication, a linear mixed effect model (lmer procedure of lmerTest R library) was used for statistical analysis:

$$Myelination\ index \sim treatment + (1|coverslip) + (1|experiment)$$

where the treatment was considered as fixed effect and coverslip and experiment as random effects.

Chapter 3 – Part II, *In vitro* tests

All the *in vitro* tests were carried out in Bf3R laboratories by the co-author of the already published paper and here are reported to clarify the *in vitro* procedures.

Test substances
Propiconazole (CAS # 60207-90-1; Batch # CGA64250B; purity 96.10%) was acquired in technical quality from Syngenta AG (Basel, Switzerland) and benzo[*b*]fluoranthene (CAS # 205-99-2; purity 98.00%) from Sigma-Aldrich (Taufkirchen, Germany). For receptor transactivation assays,

propiconazole in analytical quality from LGC Standards (Wesel, Germany) (CAS # 60207-90-1; Batch # G144536; purity 99.00%) was used. For dilution of the test substances, DMSO (dimethylsulfoxide) was used, resulting in a final DMSO concentration of 0.2% in the treatment medium. For mixture experiments concentrations of the test substances were halved (10 μM A+B corresponds to 5 μM A + 5 μM B).

Cultivation of cells

The human hepatocellular carcinoma cells HepaRG were acquired from Biopredic International (Saint Grégoire, France) and cultured as previously described (Gripon *et al*., 2002). For a period of two weeks the HepaRG cells were incubated in the proliferation medium which consists of Williams E medium (Pan-Biotech GmbH, Aidenbach, Germany), 10% fetal calf serum (FCS; Pan-Biotech GmbH), 100 U/ml penicillin, 100 μg/mL streptomycin, 0.05% human insulin (PAA Laboratories GmbH, Pasching, Austria) and 50 μM hydrocortisone-hemisuccinate (Sigma-Aldrich). For differentiation, the cells were incubated for further two weeks in differentiation medium, which includes the proliferation medium and 1.7% DMSO. Differentiated cells were treated with test substances in phenol red-free Williams E medium (Pan-Biotech GmbH) including the same supplements as the differentiation medium, but only 2% FCS.

The PXR, AHR, and CAR knockout HepaRG cells were purchased from Sigma-Aldrich. The cultivation was done according to the manufacturers' protocol. In brief, cells were thawed in recovery medium (Sigma-Aldrich) and cultivated in recovery medium for two days. Afterwards, cells were cultured for a period of two weeks in maintenance medium (Sigma-Aldrich) then for one day in pre-induction-medium (Sigma-Aldrich) before being treated in serum-free-induction medium (Sigma-Aldrich).

The incubation of HepG2 cells (ECACC, Porton Down, UK) was performed in DMEM medium (Pan-Biotech GmbH) which included 10% FCS. Cells were passaged when they had reached a confluence of about 80%,. Treatment with the test substances was performed in phenol red-free DMEM medium (Pan-Biotech GmbH) supplemented with 10% FCS (Pan-Biotech GmbH) for 24 hours. Incubation of both cell lines was done at 37°C and 5% CO_2 in a humidified atmosphere in a Binder cell culture incubator.

Testing of cell viability

For analysis of cell viability, we used the colorimetric MTT (3-(4,5-dimethylthiazol-2-yl)-2,5-diphenyltetrazolium bromide) reduction assay according to standard protocols (Braeuning *et al*., 2012). The detergent Triton X-100 (0.01%) was used as positive control.

Animal experiment

The animal experiment was conducted as previously described (Schmidt *et al*., 2016). In brief, 5-6 week old male Wistar rats were treated with propiconazole via rodent standard diet for 28 days at a dose level of 2.4 ppm, 240 ppm or 2400 ppm yielding 181 mg/kg bw/d. Animals were deeply anaesthetized with Sevofluran (Abbot, Germany), finally sacrificed by 95% CO_2 / 5% O_2 and livers were isolated. Directly after isolation, livers were partially frozen on dry ice for subsequent molecular analysis. Additionally, standard pathology and histopathology were performed according to standard principles of the Society for Toxicopathology (STP 2010) as previously reported (Schmidt *et al* 2016).

Reporter gene assays

The dual luciferase reporter gene assays were performed using HepG2 cells in 96-well plates. For transient transfection of the cells, TransIT-LT1 (Mirus Bio LLC, Madison; WI, USA) was used. For each assay, the cells were transfected with two plasmids (see Table 1). A detailed description of the generation and the features of the luciferase reporter constructs used in this study is available elsewhere (Schreiber *et al*., 2006; Schulthess *et al*., 2015). In brief, a pT81Luc-based firefly luciferase

reporter driven by a 1.2 kbp fragment of the wildtype human *CYP1A1* promoter including four functional AHR binding sites was used. In addition, a mutant version of the promoter lacking these AHR-responsive sites (-CDEF) came into operation. Third, a pT81Luc-based artificial promoter construct consisting of three AHR binding sites (3xDRE) was used. For all three assays, cells were co-transfected with a second plasmid, which constitutively expresses *Renilla* luciferase and served as internal control. After transfection, treatment and lysis of the cells (100 mM potassium phosphate with 0.2% (v/v) Triton X-100, pH 7.8), luminescence was measured using a plate reader (Infinite M200PRO, Tecan, Männedorf, Switzerland) according to the Dual Luciferase Assay protocol provided by the supplier (Promega, Madison, WI, USA).

Luciferase assay	Plasmid	Time of incubation	Positive control
***hCYP1A1*-promoter**	pT81Luc-hCYP1A1 pcDNA3-RLuc	48 h	10 μM BbF
***hCYP1A1* (-CDEF)-promoter**	pT81Luc-hCYP1A1-CDEF pcDNA3-RLuc	48 h	10 μM BbF
3xDRE	pT81Luc-3xDRE pcDNA3-RLuc	24 h	10 μM BbF

Table 32: Plasmids used for dual luciferase reporter gene assays in HepG2 cells.

Gene expression analysis

HepaRG cells and HepaRG knockout cells were treated for 24 hours in 6 well plates with the test substances. RNA from cells as well as from rat liver tissues frozen in nitrogen was isolated using peqGOLD TriFast (peqlab, Erlangen, Germany) or TRIzol reagent (Invitrogen, Carlsbad, CA, USA) according to the manufacturers' protocol. Quality and quantity of the isolated RNA were controlled with a Nanodrop spectrophotometer (NanoDrop 2000, Thermo Fisher Scientific, Waltham, MA, USA). If necessary, RNA was further purified using a RNA purification kit (Qiagen, Hilden, Germany). The human microarray Agilent Expression Profiling Service (incl. 8x60K Array) was performed by ATLAS Biolabs GmbH. The results were further analyzed using the bioinformatic analysis and search tool IPA (Ingenuity Pathway Analysis) from QIAGEN. Therefore, the IPA "Tox Analysis" tool was used. All analyses were performed with the standard settings, where no filtering was applied and direct as well as indirect relationships were considered (date of the search: 2017/11/10). Real-time RT-PCR was performed as described previously (Heise *et al.*, 2015). In brief, reverse transcription of 1 μg of RNA (HepaRG cells) or 2 μg RNA (rat livers) was conducted using the High Capacity cDNA Reverse Transcription Kit (Applied Biosystems, Darmstadt, Germany). Quantitative real-time PCR was performed of 40 ng cDNA on an ABI 7900HT instrument (Applied Biosystems) using Maxima SYBR Green/ROX qPCR Mastermix (Thermo Fisher Scientific) and primers (0.25 μM, synthesized at Eurofins Genomics, see Table 2).

gene name	forward primer	reverse primer
hGAPDH	CCACTCCTCCACCTTTGAC	ACCCTGTTGCTGTAGCCA
hACTB	ACCGAGCGCGGCTACAG	CTTAATGTCACGCACGATTTCC
hCYP1A1	TGTCAGTGGCCAACGTCATT	AGGGTTAGGCAGGTAGCGAA
hCYP1A2	TGCAAGACAAGCTGGTGTCTA	TCTCATGCGCTCACAGAACT
rGapdh	CCGTGGGGCAGCCCAGAAC	GCCCCAGCATCAAAGGTGGAGGA
rActb	AGGGAAATCGTGCGTGAC	CGCTCATTGCCGATAGTG
rCyp1a1	TTCACCATCCCCCACAGCACCATA	CAGGCCGGAACTCGTTTGGATCAC
rCyp1a2	CGGTGATTGGCAGAGATCGG	GTCCCTCGTTGTGCTGTGG

Table 33: Sequences of primers used for RT-PCR analysis.

Cyp protein quantification

HepaRG cells were treated with the test substance Pi for 24 hours in 6-well plates. After two washing steps with ice-cold PBS-buffer, the cells were incubated for 1 hour at 4 °C with lysis buffer under shaking (Zahn *et al*., 2017). Afterwards, each sample was prepared and measured as described previously (Marx-Stoelting *et al*., 2017; Wegler *et al*., 2017). In brief, a proteolysis was performed and multi-specific antibodies recognizing short C-terminal sequences of proteotypic peptide fragments were mixed with isotopically labeled peptides. With the help of an automated immunoprecipitation procedure endogenous peptides and standards for the proteins were enriched (Weiß *et al*., 2015). Peptide-antibody-complexes were precipitated with magnetic protein G microspheres using a magnetic particle processor. Elution was achieved with 1% formic acid and peptides were subsequently desalted by a PepMap100 μ-precolumn (0.3 mm I.D. x 5 mm, Thermo Fisher Scientific, Waltham, MA, USA) and separated by an Acclaim Rapid Separation LC (RSLC) Column (75 μm I.D. x 150 mm; Thermo Fisher Scientific, Waltham, MA, USA) on a UltiMate 3000 RSLCnano LC system (Thermo Fisher Scientific, Waltham, MA, USA). After that, peptides were quantified with a Q Exactive™ Plus (Thermo Fisher Scientific, Waltham, MA, USA) using targeted Single-Ion-Monitoring (tSIM). Ion chromatograms were processed with Skyline 3.7.0.11317 (MacCoss Lab. Department of Genome Sciences, UW, USA). Concentrations were calculated by the peak area ratios of isotopically labeled and endogenous peptides on parent ion level. The analyte-dependent lower limits of quantification (LLOQ) were determined with a dilution series of standard peptides (0.1-0.4 fmol/μg).

Cyp activity assay

HepaRG cells were treated for 24 hours in 96-well plates with the test substances. 10 μM of the substrate 7-ethoxyresorufin was added to each well and incubated for 30 minutes at 37°C. Liver microsomes were isolated in a 250 mM sucrose buffer (Merck, Darmstadt, Germany) by differential centrifugation at a final speed of 100,000g for 1 h. Afterwards, the O-dealkylation of the substrates 7-ethoxyresorufin (EROD) and 7-methoxyresorufin (MROD) were measured to detect the enzyme activity of CYP1A1 and CYP1A2 using resorufin as a standard (reagents obtained from Sigma-Aldrich, Basel, Switzerland). The assay was performed at 37 °C in a KH_2PO_4/K_2HPO_4 buffer at pH 7.4. Fluorescence measurements (535 nm/590 nm) were conducted on a Tecan Plate Reader (Tecan, Infinite M200Pro).

Statistical analysis

The statistical analysis was performed using SigmaPlot for Windows software (Version 13.0, Systat Software Inc. 2008). The Shapiro-Wilks and Brown-Forsythe tests were used to analyze the data for normal distribution and for homogeneity of variances. These results demonstrated that non-parametric testing is the adequate testing method for the present data sets. Therefore the Mann-Whitney rank sum test was executed to compare the solvent control to respective treatment groups. Error bars depict the standard deviation and asterisks (*) define statistical significance if $p \leq 0.05$. For the combination experiments, a statistical dose-response modeling was performed.

References

Abdelaziz, A., Spahn-Langguth, H., Schramm, K.-W., Tetko, I.V. 2016 Consensus modeling for HTS assays using in silico descriptors calculates the best balanced accuracy in Tox21 challenge. *Front. Environ. Sci.*

Abagyan, R., Chen, W. & Kufareva, I., 2012. Docking, Screening and Selectivity Prediction for Small-molecule Nuclear Receptor Modulators. *Approaches to Nuclear* (30), pp.84–109.

Andersen, M.E., Clewell, H.J., Gargas, M.L., Smith, F.A. and R.H. Reitz; Physiologi-cally based pharmacokinetics and the risk assessment process for methylene chloride; *Toxicol. Appl. Pharmacol.* 87 (1987) 185-205

Andrieux L, Langouet S, Fautrel A et al 2004 .Aryl hydrocarbon recep- tor activation and cytochrome P450 1A induction by the mito- gen-activated protein kinase inhibitor U0126 in hepatocytes. *Mol Pharmacol* 65(4):934–943. h

Andreu-Sánchez, O., Paraiba, L. C., Jonsson, C. M. and J. M. Carrasco; 2011. Acute toxicity and bioconcentration of fungicide tebuconazole in zebra fish (Danio rero); *Environ. Toxicol.* 21

Andrysik Z, Vondracek J, Machala M et al. 2007. The aryl hydrocar- bon receptor-dependent deregulation of cell cycle control induced by polycyclic aromatic hydrocarbons in rat liver epithelial cells. *Mutat Res* 615(1–2):87–97.

Baan R, Grosse Y, Straif K et al. 2009. A review of human carcino- gens—Part F: chemical agents and related occupations. *Lancet Oncol* 10(12):1143–1144

Benfenati, E., Roncaglioni, A., Petoumenou, M.I., Cappelli, C.I., Gini, G., 2015. Integrating QSAR and read-across for environmental assessment. *SAR QSAR Environ Res.* 26 (7-9), 605–618.

Bernardes, A. et al., 2013. Molecular mechanism of peroxisome proliferator-activated receptor α activation by WY14643: A new mode of ligand recognition and receptor stabilization. *Journal of Molecular Biology*, 425(16), pp.2878–2893.

Bisson, W.H. et al., 2009. Modeling of the aryl hydrocarbon receptor (AhR) ligand binding domain and its utility in virtual ligand screening to predict new AhR ligands. *Journal of Medicinal Chemistry*, 52(18), pp.5635–5641.

Bois, F.Y. et al., 2017. Multiscale modelling approaches for assessing cosmetic ingredients safety. *Toxicology*, 392, pp.130–139.

Borgert, Christopher J. et al., 2011. Hypothesis-driven weight of evidence framework for evaluating data within the US EPA's Endocrine Disruptor Screening Program. *Regulatory Toxicology and Pharmacology* 61 (2), 185–191.

Bosgra, S., Bos, P., van Eijkeren, J., Zeilmaker, M., Vermeire, T., Rompelberg, C., and W. Slob; An improved model to predict physiologically based model parameters and their inter-individual variability from anthropometry. *Critical Reviews in Toxicology* 42(9):751-67

Braeuning A, Buchmann A. 2009. The glycogen synthase kinase inhibitor 3-(2,4-dichlorophenyl)-4-(1-methyl-1H-indol-3-yl)- 1H-pyrrole-2,5-dione (SB216763) is a partial agonist of the aryl hydrocarbon receptor. *Drug Metab Dispos Biol Fate Chem* 37(8):1576–1580.

Braeuning A, Vetter S, Orsetti S, Schwarz M. 2012. Paradoxical cytotoxicity of tert-butylhydroquinone in vitro: what kills the untreated cells? *Arch Toxicol* 86(9):1481–1487.

Braeuning A, Gavrilov A, Brown S, Wolf CR, Henderson CJ, Schwarz M. 2014. Phenobarbital-mediated tumor promotion in transgenic mice with humanized CAR and PXR. *Toxicol Sci* 140(2):259– 270.

Braeuning A, Thomas M, Hofmann U et al. 2015. Comparative analysis and functional characterization of HC-AFW1 hepato- carcinoma cells: cytochrome P450 expression and induction by nuclear receptor agonists. *Drug Metab Dispos Biol Fate Chem* 43(11):1781–1787.

Braeuning A, Gavrilov A, Geissler M et al. 2016. Tumor promo- tion and inhibition by phenobarbital in livers of conditional Apc-deficient mice. *Arch Toxicol* 90(6):1481–1494.

Brown, R.P. et al., 1997. Physiological Parameter Values for Physiologically Based Pharmacokinetic

Models. *Toxicology and Industrial Health*, 13(4), pp.407–484.
Buist, H.E., Ld, Wit-Bos, Bouwman, T., Vaes, W.H., 2012. Predicting blood:air partition coefficients using basic physicochemical properties. *Regul Toxicol Pharmacol*. 62 (1), 23–28.
Conroy-Ben, O., Garcia, I., Teske, S.S., 2018. In silico binding of 4,4′-bisphenols predicts in vitro estrogenic and antiandrogenic activity. *Environ. Toxicol*. 33, 569–578.
Cooper, J.A., Saracci, R., Cole, P., 1979. Describing the validity of carcinogen screening tests. Br. *J. Cancer*.
Corton JC, Cunningham ML, Hummer BT et al. 2014. Mode of action framework analysis for receptor-mediated toxicity: the peroxi- some proliferator-activated receptor alpha (PPARalpha) as a case study. *Crit Rev Toxicol* 44(1):1–49.
Currie RA, Peffer RC, Goetz AK, Omiecinski CJ, Goodman JI. 2014. Phenobarbital and propiconazole toxicogenomic profiles in mice show major similarities consistent with the key role that constitutive androstane receptor (CAR) activation plays in their mode of action. *Toxicology* 321:80–88.
Delfosse, V., Grimaldi, M., Pons, J.-L., Boulahtouf, A., le Maire, A., Cavailles, V., Labesse, G., Bourguet, W., Balaguer, P., 2012. Structural and mechanistic insights into bi- sphenols action provide guidelines for risk assessment and discovery of bisphenol a substitutes. *Proc. Natl. Acad. Sci. U. S. A*. 109, 14930–14935.
Denison MS, Soshilov AA, He G, DeGroot DE, Zhao B. 2011. Exactly the same but different: promiscuity and diversity in the molecular mechanisms of action of the aryl hydrocar- bon (dioxin) receptor. *Toxicol Sci* 124(1):1–22.
Diab, A. et al., 2004. Ligands for the peroxisome proliferator-activated receptor-gamma and the retinoid X receptor exert additive anti-inflammatory effects on experimental autoimmune encephalomyelitis. *Journal of neuroimmunology*, 148(1–2), pp.116–26.
Diamanti-Kandarakis, E., Bourguignon, J.P., Giudice, L.C., Hauser, R., Prins, G.S., Soto, A.M., Zoeller, R.T., Gore, A.C., 2009. Endocrine-disrupting chemicals: an Endocrine Society scientific statement. *Endocr. Rev*
Ding, D., Xu, L., Fang, H., Hong, H., Perkins, R., Harris, S., Bearden, E.D., Shi, L., Tong, W., 2010. The EDKB: an established knowledge base for endocrine disrupting che- micals. *BMC Bioinformatics*
Di Renzo, F. et al., 2007. Citral, an inhibitor of retinoic acid synthesis, attenuates the frequency and severity of branchial arch abnormalities induced by triazole-derivative fluconazole in rat embryos cultured in vitro. *Reproductive Toxicology*, 24(3–4), pp.326–332.
Di Renzo, F. et al., 2011. Early genetic control of craniofacial development is affected by the in vitro exposure of rat embryos to the fungicide triadimefon. *Birth Defects Research Part B - Developmental and Reproductive Toxicology*, 92(1), pp.77–81.
Di Renzo, F. et al., 2010. VPA-related axial skeletal defects and apoptosis: A proposed event cascade. *Reproductive Toxicology*, 29(1), pp.106–112.
EFSA. 2010. Conclusion on the peer review of the pesticide risk assess- ment of the active substance cyproconazole. *EFSA Journal* 8(11):1897
EFSA, 2019. Guidance on harmonised methodologies for human health, animal health and ecological risk assessment of combined exposure to multiple chemicals. *EFSA Journal* 17 (3), 5634.
Elcombe CR, Peffer RC, Wolf DC et al. 2014. Mode of action and human relevance analysis for nuclear receptor-mediated liver toxicity: a case study with phenobarbital as a model consti- tutive androstane receptor (CAR) activator. *Crit Rev Toxicol* 44(1):64–82.
Ema M, Ohe N, Suzuki M et al. 1994. Dioxin binding activities of polymorphic forms of mouse and human arylhydrocarbon recep- tors. *J Biol Chem* 269(44):27337–27343
Erbel PJ, Card PB, Karakuzu O, Bruick RK, Gardner KH. 2003. Structural basis for PAS domain heterodimerization in the basic helix–loop–helix-PAS transcription factor hypoxia-inducible factor. *Proc Natl Acad Sci USA* 100(26):15504–15509.
Flaveny CA, Murray IA, Chiaro CR, Perdew GH. 2009. Ligand selec- tivity and gene regulation by

the human aryl hydrocarbon receptor in transgenic mice. *Mol Pharmacol* 75(6):1412–1420.
Galli, C.L. et al., 2014. A computational approach to evaluate the androgenic affinity of iprodione, procymidone, vinclozolin and their metabolites. *PLoS ONE*, 9(8).
Ghisari M, Long M, Tabbo A, Bonefeld-Jorgensen EC. 2015. Effects of currently used pesticides and their mixtures on the func- tion of thyroid hormone and aryl hydrocarbon receptor in cell culture. *Toxicol Appl Pharmacol* 284(3):292–303.
Goettel M, Melching-Kollmuss S, Honarvar N, Marxfeld H, Elcombe CR, Fegert I. 2015. Mouse liver tumors induced by prochloraz have a CAR-like mode of action and are not relevant to humans. *Toxicol Suppl Toxicol Sci* 144:1
Goetz AK, Dix DJ. 2009. Mode of action for reproductive and hepatic toxicity inferred from a genomic study of triazole antifungals. *Toxicol Sci* 110(2):449–462.
Gripon P, Rumin S, Urban S et al (2002) Infection of a human hepatoma cell line by hepatitis B virus. *Proc Natl Acad Sci USA* 99(24):15655–15660.
Halwachs S, Wassermann L, Lindner S, Zizzadoro C, Honscha W. 2013. Fungicide prochloraz and environmental pollutant dioxin induce the ABCG2 transporter in bovine mammary epithelial cells by the arylhydrocarbon receptor signaling pathway. *Toxicol Sci* 131(2):491–501.
Hamblen, E.L., Cronin, M.T.D., Schultz, T.W., 2003. Estrogenicity and acute toxicity of selected anilines using a recombinant yeast assay. *Chemosphere*.
Heise T, Schmidt F, Knebel C et al. 2015. Hepatotoxic effects of (tri)azole fungicides in a broad dose range. *Arch Toxicol* 89(11):2105–2117.
Heise T, Schmidt F, Knebel C et al. 2018. Hepatotoxic combination effects of three azole fungicides in a broad dose range. *Arch Toxicol* 92(2):859–872
Henikoff, S. & Henikoff, J.G., 1992. Amino acid substitution matrices from protein blocks. *Proceedings of the National Academy of Sciences*, 89(22), pp.10915–10919.
Hester SD, Nesnow S. 2008. Transcriptional responses in thyroid tissues from rats treated with a tumorigenic and a non-tumorigenic triazole conazole fungicide. T*oxicol Appl Pharmacol* 227(3):357– 369.
Hewitt, M., Ellison, C.M., Enoch, S.J., Madden, J.C., Cronin, M.T., 2010. Integrating (Q) SAR models, expert systems and read-across approaches for the prediction of devel- opmental toxicity. *Reprod Toxicol*. 30 (1), 147–160
Hornung, M.W. et al., 2014. Effects-based chemical category approach for prioritization of low affinity estrogenic chemicals. *SAR and QSAR in Environmental Research*, 25(4), pp.289–323.
Huang, J.K. et al., 2011. Retinoid X receptor gamma signaling accelerates CNS remyelination. *Nature neuroscience*, 14(1), pp.45–53.
Humphrey, M.J., Jevons, S. & Tarbit, M.H., 1985. Pharmacokinetic evaluation of UK-49,858, a metabolically stable triazole antifungal drug, in animals and humans. *Antimicrobial Agents and Chemotherapy*, 28(5), pp.648–653.
Judson, R., Houck, K., Martin, M., Knudsen, T., Thomas, R.S., Sipes, N., Shah, I., Wambaugh, J., Crofton, K., 2014. In vitro and modelling approaches to risk assess- ment from the U.S. environmental protection agency ToxCast programme. *Basic Clin. Pharmacol. Toxicol.*
Kienhuis AS, Slob W, Gremmer ER, Vermeulen JP, Ezendam J. 2015. A dose-response modeling approach shows that effects from mix- ture exposure to the skin sensitizers isoeugenol and cinnamal are in line with dose addition and not with synergism. *Toxicol Sci* 147(1):68–74.
Knebel C, Neeb J, Zahn E et al. 2018. Unexpected effects of propicona- zole, tebuconazole and their mixture on the receptors CAR and PXR in human liver cells. *Toxicol Sci*.
Kortenkamp A, Faust M. 2018. Regulate to reduce chemical mixture risk. *Science* 361(6399):224–226.
Kortenkamp A, Backhaus T, Faust M. 2009. State of the art report on mixture toxicity. *Contract* 70307:94–103
Labute, P., 2010. LowModeMD - Implicit low-mode velocity filtering applied to conformational search of macrocycles and protein loops. *Journal of Chemical Information and Modeling*, 50(5),

pp.792–800.
Labute, P., 2008. The generalized Born/volume integral implicit solvent model: Estimation of the free energy of hydration using London dispersion instead of atomic surface area. *Journal of Computational Chemistry*, 29(10), pp.1693–1698.
Larsson M, Orbe D, Engwall M. 2012. Exposure time-dependent effects on the relative potencies and additivity of PAHs in the Ah receptor-based H4IIE-luc bioassay. *Environ Toxicol Chem* 31(5):1149–1157.
Li, J. et al., 2012. IDSite: An accurate approach to predict P450-mediated drug metabolism. *J Chem Theory Comput.*, 7(11), pp.3829–3845.
Li ZH, Zlabek V, Velisek J et al. 2013. Multiple biomarkers responses in juvenile rainbow trout, Oncorhynchus mykiss, after acute expo- sure to a fungicide propiconazole. *Environ Toxicol* 28(3):119– 126.
Marotta, F. & Tiboni, G.M., 2010. Molecular aspects of azoles-induced teratogenesis. *Expert opinion on drug metabolism & toxicology*, 6(4), pp.461–482.
Marx-Stoelting P, Ganzenberg K, Knebel C et al (2017) Hepato- toxic effects of cyproconazole and prochloraz in wild-type and hCAR/hPXR mice. *Arch Toxicol*.
Mellor, C.L., Steinmetz, F.P. & Cronin, M.T.D., 2015. The identification of nuclear receptors associated with hepatic steatosis to develop and extend adverse outcome pathways. *Critical Reviews in Toxicology*, 8444(January), pp.1–15.
Mellor, C.L., Steinmetz, F.P. & Cronin, M.T.D., 2016. Using Molecular Initiating Events to Develop a Structural Alert Based Screening Workflow for Nuclear Receptor Ligands Associated with Hepatic Steatosis. *Chemical Research in Toxicology*, 29(2), pp.203–212.
Menegola, E. et al., 2001. Antifungal triazoles induce malformations in vitro. *Reproductive Toxicology*, 15(4), pp.421–427.
Menegola, E. et al., 2016. Comparison of teratogenic potency of azoles using in silico and in vitro methods. *Toxicology Letters*, 258, p.S294.
Menegola, E., Broccia, M.L., Renzo, F.D., et al., 2006. Dysmorphogenic effects of some fungicides derived from the imidazole on rat embryos cultured in vitro. *Reproductive Toxicology*, 21(1), pp.74–82.
Menegola, E., Broccia, M.L., Di Renzo, F., et al., 2006. Postulated pathogenic pathway in triazole fungicide induced dysmorphogenic effects. *Reproductive Toxicology*, 22(2), pp.186–195.
Menegola, E. et al., 2004. Relationship between hindbrain segmentation, neural crest cell migration and branchial arch abnormalities in rat embryos exposed to fluconazole and retinoic acid in vitro. *Reproductive Toxicology*, 18(1), pp.121–130.
Mercadante, R. et al., 2014. Identification and quantification of metabolites of the fungicide tebuconazole in human urine. *Chemical Research in Toxicology*, 27(11), pp.1943–1949.
Mombelli, E., 2012. Evaluation of the OECD (Q)SAR Application Toolbox for the profiling of estrogen receptor binding affinities. *SAR and QSAR in Environmental Research*, 23(1–2), pp.37–57.
Najm, F.J. et al., 2015. Drug-based modulation of endogenous stem cells promotes functional remyelination in vivo. *Nature*, 522(7555), pp.216–220.
Needleman, S.B. & Wunsch, C.D., 1970. A general method applicable to the search for similarities in the amino acid sequence of two proteins. *Journal of Molecular Biology*, 48(3), pp.443–453.
Ng, H.W. et al., 2014. Competitive molecular docking approach for predicting estrogen receptor subtype α agonists and antagonists. *BMC Bioinformatics*, 15(Suppl 11), p.S4. Available at: http://bmcbioinformatics.biomedcentral.com/articles/10.1186/1471-2105-15-S11-S4.
Niederreither, K. et al., 2000. Retinoic acid synthesis and hindbrain patterning in the mouse embryo. *Development (Cambridge, England)*, 127(1), pp.75–85.
Opitz CA, Litzenburger UM, Sahm F et al. 2011. An endogenous tumour-promoting ligand of the human aryl hydrocarbon receptor. *Nature* 478(7368):197–203.
Pang, X., Fu, W., Wang, J., Kang, D., Xu, L., Zhao, Y., Liu, A.-L., Du, G.-H., 2018. Identification

of estrogen receptor alpha antagonists from natural products via in vitro and in silico approaches. *Oxidative Med. Cell. Longev.*

Peffer RC, Moggs JG, Pastoor T et al. 2007. Mouse liver effects of cyproconazole, a triazole fungicide: role of the constitutive androstane receptor. *Toxicol Sci* 99(1):315–325.

Piparo, E. Lo, Worth, A.P., 2010. Review of QSAR Models and Software Tools for Predicting Developmental and Reproductive Toxicity.

Rajakumar, B. & Arunan, E., 2003. Ab initio, DFT and transition state theory calculations on 1,2-HF, HCI and CIF elimination reactions from CH2F?CH2ClElectronic supplementary information (ESI) available: Structural details and vibrational frequencies for the ground and transition states f. *Physical Chemistry Chemical Physics*, 5(18), p.3897.

Ray, W.J. et al., 1997. CYP26, a novel mammalian cytochrome P450, is induced by retinoic acid and defines a new family. *Journal of Biological Chemistry*, 272(30), pp.18702–18708.

Rieke S, Koehn S, Hirsch-Ernst K, Pfeil R, Kneuer C, Marx-Stoelting P (2014) Combination effects of (tri)azole fungicides on hormone production and xenobiotic metabolism in a human placental cell line. *Int J Environ Res Public Health* 11(9):9660–9679.

Rieke S, Heise T, Schmidt F et al (2017) Mixture effects of azole fun- gicides on the adrenal gland in a broad dose range. *Toxicology* 385:28–37.

Rorije, E., van Hienen, F.J., Dang, Z.C., Hakkert, B.H., Vermeire, T., Piersma, A.H., 2012. Relative parameter sensitivity in prenatal toxicity studies with substances classified as developmental toxicants. *Reprod Toxicol*. 34 (2), 284–290.

Roncaglioni, A. et al., 2008. Binary classification models for endocrine disrupter effects mediated through the estrogen receptor. In *SAR and QSAR in Environmental Research*. pp. 697–733.

Rydberg, P. et al., 2009. Fast prediction of cytochrome p450 mediated drug metabolism. *ChemMedChem*, 4(12), pp.2070–2079.

Rydberg, P. et al., 2010. SMARTCyp: A 2D method for prediction of cytochrome P450-mediated drug metabolism. *ACS Medicinal Chemistry Letters*, 1(3), pp.96–100.

Rydberg, P., Jorgensen, F.S. & Olsen, L., 2014. Use of density functional theory in drug metabolism studies. *Expert opinion on drug metabolism & toxicology*, 10(2), pp.215–227.

Sandell, L.L. et al., 2012. RDH10 oxidation of vitamin A is a critical control step in synthesis of retinoic acid during mouse embryogenesis. *PLoS ONE*, 7(2).

Schmidt F, Marx-Stoelting P, Haider W et al. 2016. Combination effects of azole fungicides in male rats in a broad dose range. *Toxicology* 355–356:54–63.

Schmieder, P.K. et al., 2014. A rule-based expert system for chemical prioritization using effects-based chemical categories. *SAR and QSAR in Environmental Research*, 25(4), pp.253–287.

Schreiber TD, Kohle C, Buckler F et al. 2006. Regulation of CYP1A1 gene expression by the antioxidant tert-butylhydroquinone. *Drug Metab Dispos Biol Fate Chem* 34(7):1096–1101

Schug, T.T., Janesick, A., Blumberg, B., Heindel, J.J., 2011. Endocrine disrupting che- micals and disease susceptibility. J. *Steroid Biochem. Mol. Biol*. 127, 204–215.

Schulthess P, Loffler A, Vetter S et al. 2015. Signal integration by the CYP1A1 promoter—a quantitative study. *Nucleic Acids Res* 43(11):5318–5330.

Sergent T, Dupont I, Jassogne C et al. 2009. CYP1A1 induction and CYP3A4 inhibition by the fungicide imazalil in the human intestinal Caco-2 cells-comparison with other conazole pesticides. *Toxicol Lett* 184(3):159–168.

Shiau, A.K., Barstad, D., Loria, P.M., Cheng, L., Kushner, P.J., Agard, D.A., Greene, G.L., 1998. The structural basis of estrogen receptor/coactivator recognition and the an- tagonism of this interaction by tamoxifen. *Cell* 95, 927–937.

Sun G, Thai SF, Tully DB et al. 2005. Propiconazole-induced cytochrome P450 gene expression and enzymatic activities in rat and mouse liver. *Toxicol Lett* 155(2):277–287.

Thomas Zoeller, R. et al., 2012. Endocrine-disrupting chemicals and public health protection: A statement of principles from the Endocrine Society. *Endocrinology*, 153(9), pp.4097–4110.

Tiboni, G.M., 1993. Second branchial arch anomalies induced by fluconazole, a bis-triazole

antifungal agent, in cultured mouse embryos. *Res.Commun.Chem.Pathol.Pharmacol.*, 79(3), pp.381–384.

Trisciuzzi, D., Alberga, D., Mansouri, K., Judson, R., Novellino, E., Mangiatordi, G.F., Nicolotti, O., 2017. Predictive structure-based toxicology approaches to assess the androgenic potential of chemicals. *J. Chem. Inf. Model.* 57, 2874–2884.

Tzameli I, Pissios P, Schuetz EG, Moore DD. 2000. The xenobiotic compound 1,4-bis[2-(3,5-dichloropyridyloxy)]benzene is an agonist ligand for the nuclear receptor CAR. *Mol Cell Biol* 20(9):2951–2958

Van der Heiden E, Bechoux N, Muller M et al. 2009. Food flavo- noid aryl hydrocarbon receptor-mediated agonistic/antagonis- tic/synergic activities in human and rat reporter gene assays. *Anal Chim Acta* 637(1–2):337–345.

Vanier, K.L., Mattiussi, A.J. & Johnston, D.L., 2003. Interaction of all-trans-retinoic acid with fluconazole in acute promyelocytic leukemia. *Journal of pediatric hematology/oncology*, 25(5), pp.403–404.

Vuorinen, A., Odermatt, A., Schuster, D.J., 2013. In silico methods in the discovery of endocrine disrupting chemicals. *J. Steroid Biochem. Mol. Biol.* 137, 18–26.

Wegler C, Gaugaz FZ, Andersson TB et al (2017) Variability in mass spectrometry-based quantification of clinically relevant drug trans- porters and drug metabolizing enzymes. *Mol Pharm* 14(9):3142– 3151.

Weiß F, Schnabel A, Planatscher H et al (2015) Indirect protein quan- tification of drug-transforming enzymes using peptide group- specific immunoaffinity enrichment and mass spectrometry. *Sci Rep* 5:8759

Wojciechowski, M. & Lesyng, B., 2004. Generalized Born model: Analysis, refinement, and applications to proteins. *Journal of Physical Chemistry B*, 108(47), pp.18368–18376.

Wu, D. et al., 2013. Structure and dimerization properties of the aryl hydrocarbon receptor PAS-A domain. *Molecular and cellular biology*, 33(21), pp.4346–56.

Wu, S., Fisher, J., Naciff, J., Laufersweiler, M., Lester, C., Daston, G., Blackburn, K., 2013. Framework for identifying chemicals with structural features associated with the potential to act as developmental or reproductive toxicants. *Chemical Research in Toxicology*.

Yamada T, Okuda Y, Kushida M et al. 2014. Human hepatocytes sup- port the hypertrophic but not the hyperplastic response to the murine nongenotoxic hepatocarcinogen sodium phenobarbital in an in vivo study using a chimeric mouse with humanized liver. *Toxicol Sci* 142(1):137–157.

Ye, H., Shaw, I.C., 2019. Food flavonoid ligand structure/estrogen receptor-alpha affinity relationships - toxicity or food functionality? *Food Chem. Toxicol*

Zahn E, Wolfrum J, Knebel C et al. 2018 Mixture effects of two plant protection products in liver cell lines. *Food Chem Toxicol.* 112:299–309.

Zhang, R. et al., 2015. Transcriptional factors mediating retinoic acid signals in the control of energy metabolism. *International Journal of Molecular Sciences*, 16(6), pp.14210–14244.

Zhu, W. et al., 2007. Stereoselective Degradation Kinetics of Tebuconazole in Rabbits. , 147(May 2006), pp.141–147.